Forward and Inverse Calculation Methods for Lorentz Force Evaluation applied to Laminated Composites

**Dissertation zur Erlangung des
akademischen Grades Doktor-Ingenieur (Dr.-Ing.)**

**vorgelegt der Fakultät für Informatik und Automatisierung
der Technischen Universität Ilmenau**

von M. Sc. Judith Mengelkamp

Datum der Einreichung: 11.04.2016
Datum der wissenschaftlichen Aussprache: 30.11.2016

Gutachter: 1. Prof. Dr.-Ing. habil. Jens Haueisen
2. Prof. dr. ir. Guillaume Crevecoeur
3. Dr.-Ing. Hartmut Brauer

Acknowledgements

The completion of this thesis would not have been possible without the dedication and encouragement of many persons, who deserve my sincere gratitude.

First of all, I would like to thank my principal supervisor Prof. Jens Haueisen for his continuous support and valuable advice throughout the whole work. I highly appreciate his permanent motivation to transfer the inverse methods established in biomedical engineering to the field of nondestructive testing.

I am sincerely grateful to Dr. Hartmut Brauer. His scientific knowledge and ideas in the fields of nondestructive testing and material science helped me to proceed and complete this thesis. Moreover, I would like to take the opportunity to thank Dr. Roland Eichardt for sharing his scientific knowledge in the fields of inverse methods and optimization. A very special "Thank you!" goes to Dr. Marek Ziolkowski for his never-ending patience in answering all my questions in the fields of electromagnetism and beyond.

Furthermore, I would like to thank my colleagues from the Advanced Electromagnetics Group Matthias Carlstedt for performing Lorentz force eddy current testing measurements, and Konstantin Weise for performing numerical simulations. The obtained data has been used for the inverse calculations presented in this thesis. I thank them both for the very productive teamwork throughout the last three years.

It has been a great pleasure for me to work for three months during my PhD project at the Ghent University in Belgium. I thank Prof. Guillaume Crevecoeur for the great time and experience.

In this thesis, measured data obtained from laminated composites used in the aerospace industry have been evaluated. I would like to thank the company Mejo Metall Josten GmbH & Co.KG in Düsseldorf, Germany for providing the sandwich-structured Alucobond test specimen. Moreover, I am grateful to the company Premium Aerotec in Nordenham, Germany for manufacturing a custom-made GLARE specimen. My particular thanks go to Ingo Schumann for the exceptionally interesting factory tour at Premium Aerotec that allowed a great insight into the aircraft manufacturing.

Finally, I am thankful to all other colleagues not mentioned so far from the Biomedical Engineering Group and the Advanced Electromagnetics Group for their help and discussions. Warmest thanks go to my room mate Dr. Bojana Petković for encouraging me throughout the whole time.

Abstract

The classification of material deficiencies is a key feature in quality assurance. In this framework, laminated composite materials are of special interest, because they increasingly replace monolithic materials. The Lorentz force evaluation (LFE) is an evaluation technique to reconstruct the geometry of flaws in electrically conducting composites using inverse calculations. These calculations are based on perturbations that occur in the measured Lorentz force signals and are caused by the flaws. The force signals are obtained using the nondestructive testing method Lorentz force eddy current testing (LET). In this electromagnetic technique, a permanent magnet and the material under investigation move relative to each other. As a consequence eddy currents are induced in the conductor. The eddy currents in turn interact with the magnetic field and cause a Lorentz force. Inverse calculations in LFE require a forward solution of the measured force signals, which incorporates a model of the LET setup.

The objective of this thesis is the development and evaluation of forward and inverse calculation methods for LFE. The proposed methods are assessed using Lorentz force data obtained from laminated composites.

In order to model the permanent magnet in the forward solution for LFE the magnetic dipoles model (MDM) is introduced. In the MDM, a permanent magnet is represented by an assembly of magnetic dipoles. An optimization procedure is used to determine optimal dipole positions. Contrary to analytic models the MDM can be applied to permanent magnets of arbitrary geometry, and forward calculations can be performed with analytic mathematics.

For defect reconstruction three inverse methods are introduced in this thesis. In the first method, conductivity reconstructions are performed using a stochastic optimization algorithm, the Differential Evolution (DE). Prior to inverse calculations, the intrinsic control parameters of the DE are determined based on parameter studies. As the second inverse strategy, current density reconstructions (CDR) calculated with minimum norm estimates (MNE) are employed. This approach is based on interpreting a defect in the forward solution for LFE as a distributed current source. In the third method, a goal function scan is performed to reconstruct the geometry parameters of the defect. All three inverse methods are suitable for reconstructing defects, whereas the first and third method provide more accurate results than the second.

Further, measured Lorentz force signals obtained from glass laminate aluminum reinforced epoxy (GLARE) composite are investigated. GLARE is widely used in the aircraft industry. The flaw detectability of LET and LFE for GLARE is proved.

Zusammenfassung

Die Klassifizierung von Materialdefekten ist ein wesentliches Merkmal der Qualitätssicherung. Dabei sind geschichtete Verbundwerkstoffe von besonderem Interesse, weil sie zunehmend monolithische Werkstoffe ersetzen. Lorentz force evaluation (LFE) ist eine Methode zur Rekonstruktion der Geometrie von Fehlstellen in elektrisch leitfähigen Verbundwerkstoffen mittels inverser Berechnungen. Die Grundlage der inversen Berechnungen sind Störungen, die aufgrund der Fehlstellen in den gemessenen Lorentzkraft-Signalen auftreten. Die Signale werden mittels der zerstörungsfreien Prüfmethode, der Lorentzkraft-Wirbelstromprüfung (LET) gemessen. Bei diesem elektromagnetischen Testverfahren bewegen sich ein Permanentmagnet und das zu untersuchende Material relativ zu einander. Dadurch werden Wirbelströme im Material induziert. Die Interaktion dieser mit dem Magnetfeld hat eine Lorentzkraft zur Folge. Für inverse Verfahren ist eine Vorwärtslösung zur Berechnung der Lorentzkraft notwendig, der ein Modell des LET-Aufbaus zugrunde liegt.

Das Ziel der vorliegenden Dissertation ist die Entwicklung und Evaluierung von Vorwärtslösungen und inversen Berechnungsmethoden für LFE. Zur Bewertung der Methoden werden Lorentzkraftsignale verwendet, die aus Messungen von geschichteten Verbundmaterialien stammen.

Zur Modellierung des Permanentmagneten in der Vorwärtslösung für LFE wird das Magnetische-Dipole-Modell (MDM) entwickelt. In diesem Modell wird ein Permanentmagnet durch eine Verteilung magnetischer Dipole repräsentiert. Die Positionen der magnetischen Dipole werden optimiert. Im Vergleich zu analytischen Modellen kann das MDM zur Modellierung beliebig geformter Permanentmagneten verwendet werden. Die Lorentzkraft-Signale können analytisch berechnet werden.

In dieser Dissertation werden drei inverse Berechnungsmethoden für LFE erarbeitet. In der ersten Methode wird ein stochastischer Optimierungsalgorithmus, der Differential Evolution, zur Rekonstruktion von Leitfähigkeiten im Material verwendet. Die intrinsischen Kontrollparameter des Differential Evolution (DE) werden anhand von Parameterstudien festgelegt. Als zweite inverse Methode werden Stromdichterekonstruktionen mittels Minimum-Norm-Schätzungen durchgeführt. Grundlegend für diesen Ansatz ist die Interpretation eines Defektes in der Vorwärtslösung als verteilte Stromquelle. Als dritte inverse Methode wird eine Abtastung der Zielfunktion zur Rekonstruktion der Defektparameter vorgenommen. Alle inverse Verfahren sind zur Defektrekonstruktion geeignet, wobei sich die Ergebnisse der erste und dritten Methode genauer darstellen als die der zweiten.

Des Weiteren werden Messdaten eines aus glasfaserverstärktem Aluminium (GLARE) bestehenden Prüfkörpers ausgewertet. GLARE wird insbesondere im Flugzeugbau eingesetzt. Es wird gezeigt, dass mit LET und LFE Materialfehler in GLARE nachgewiesen werden können.

Table of Contents

1 Introduction

1.1 Motivation

In the course of increasing globalization, ongoing developments in transport systems strive for larger and more complex systems that can operate at high loads. The need for more efficient systems should coincide with a minimum weight and low costs. Especially affected by this trend are the aircraft, railway and naval industry. However, the outlined needs can not be fulfilled by solely using homogeneous materials. As a consequence, composite materials that are composed of two or more constituents increasingly replace monolithic materials. Especially laminated composites that consist of an assembly of layers of different materials are of special interest.

Because material failures can give rise to technology breakdowns that cause in turn human casualties, it is inevitable for the manufacturer to ensure the health of the materials used and thus of the product. In particular, possible flaws should be detected at an early stage. During manufacturing regular controls are necessary to obtain a qualified product. Further, in-service inspections are performed in order to detect fatigue fractures. This is essential for the product maintenance and to prevent premature wear.

For these purposes quality assurance methods, which are capable of investigating the material without affecting the serviceability of the product, are of great interest. It is important that the material examination is noninvasive and does not impair any material properties. Methods that incorporate these characteristics are referred to as nondestructive testing (NDT) techniques. Their working principle is to detect and localize inhomogenities based on information in measured signals.

Then, a subsequent evaluation procedure is necessary to classify the influence of flaws on the stability and contingency risk of the product. In the evaluation procedure, an inverse problem is solved, i.e., the defect characteristics such as dimension, shape, and structure are reconstructed based on the measured NDT signals. The results can be used to determine whether a product should be rejected. The combination of the testing and evaluation procedure is referred to as nondestructive testing and evaluation (NDT&E).

Inverse calculations usually require to solve a forward problem, i.e., to simulate the measured signals using a mathematical model of the processes underlying the NDT method. This forward model has to incorporate information about the defect. The accuracy of the forward model can be evaluated by comparing the simulated Lorentz forces to the measured data. The connection of forward and inverse problem is illustrated in Figure 1.1.

For NDT&E of electrically conducting materials, the techniques Lorentz force eddy

Forward problem

Parameters of hidden defect are given

| Model of NDT problem | | Simulated data | | Measured data |

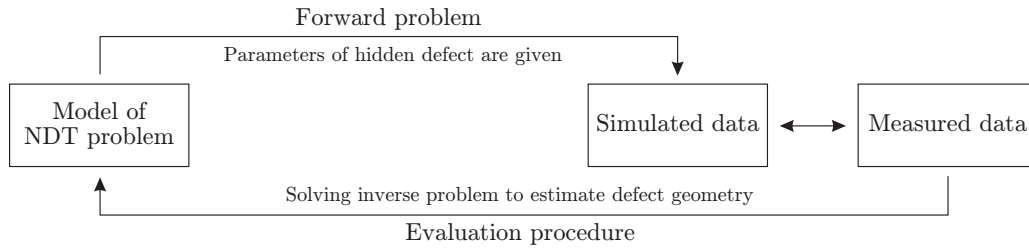Solving inverse problem to estimate defect geometry

Evaluation procedure

Figure 1.1: Illustration of the forward and the inverse problem for the reconstruction of material defects in NDT&E.

current testing (LET) and Lorentz force evaluation (LFE) have been introduced [10, 81]. LET is a contactless electromagnetic NDT method. The key principle is based on the interaction between a permanent magnet and a test object, which move relatively to each other. Due to this movement eddy currents are induced in the conductor. The interaction of the magnetic field and the eddy currents yield Lorentz forces which are measured. If the material contains defects the force signals are perturbed. LFE is an evaluation procedure to reconstruct flaws based on measured LET signals.

The objective of this thesis is to introduce new inverse calculation methods for the defect reconstruction in LFE. Inverse reconstruction approaches that have been applied in other field of application such as biomedical engineering and electromagnetic design optimization serve as a basis for this. Moreover, it is the aim to develop advanced solutions for forward modeling of LET measurement data. Thereby, the emphasis is on modeling the permanent magnet providing the magnetic field. Further, it is intended to demonstrate the efficiency of LET and LFE on laminated composite materials. For this purpose measurement data obtained from laminates that are widely used in industrial applications are applied.

1.2 Structure and Contributions of the Thesis

Chapter 2 introduces the reader to the field of NDT&E with special focus on LET and LFE. In this context an overview on laminated composites is given. Further, fundamental basics of forward and inverse calculations for LFE are described.

In Chapter 3, models of the permanent magnet for the forward solution in LFE are discussed. The main contribution of this chapter is the development of the magnetic dipoles model (MDM) [69, 72]. This model allows precise modeling of arbitrary shaped permanent magnets. The MDM is compared to existing analytic models. Further, the MDM is embedded in an existing forward solution for LFE. The magnetic field and corresponding Lorentz forces of the model are evaluated.

In Chapter 4, an inverse calculation strategy for LFE is introduced, in which the geometry of the defect is estimated by reconstructing the conductivity distribution in the material. This approach is motivated by the fact that anomalies are characterized by changes in conductivity. For inverse calculations a stochastic optimization algorithm is used [71]. In the following Chapter 5, current density reconstructions are introduced to LFE. In this inverse

method, defect estimation is based on reconstructing the induced eddy current distribution that changes depending on the defect [70]. The performance of both methods is evaluated based on measured data of a three-layered composite that has the trade name Alucobond.

Afterwards, in Chapter 6 the potential applicability of LET and LFE for industrial NDT is demonstrated by assessing measured data obtained from the glass laminate aluminum reinforced epoxy (GLARE) material. This multi-layered composite is of rapidly growing interest for public aircrafts and is mainly responsible for the technology progress in this area. A GLARE test object containing an artificial defect has been specifically manufactured for this purpose by a leading aircraft supplier. Within this framework, the performance of an advanced permanent magnet system for LET is evaluated. Further, a third inverse method, namely the goal function scanning method, is applied to estimate the defect parameters in LFE.

Finally, in Chapter 7 the results of this thesis are summarized. The performance and efficiency of the different inverse calculation methods are compared. Also, open issues are outlined.

2 Fundamentals of Lorentz Force Evaluation

2.1 Overview

A wide variety of methods exist for nondestructive testing (NDT) of electrically conducting non-ferromagnetic objects. These include ultrasonics [6,77], radiography [2], thermography [22,73], tomography [62], magnetic flux leakage (MFL) [64], and eddy current testing (ECT) [45,46,100,105]. Lorentz force eddy current testing (LET) has been introduced in 2008 [10] and belongs similar to ECT to the class of electromagnetic testing methods.

The origins of LET and of electromagnetics in general date back to the work of Faraday in 1832, Lenz in 1834, and Lorentz in 1892. Faraday's law of induction states that an electromotive force is generated in a conductor, if the conductor is moving in a magnetic field or exposed to a time-varying magnetic field [28]. This electromotive force gives rise to eddy currents flowing in the conductor. According to Lenz' law, the eddy currents are directed in such a way that the magnetic field induced by them opposes the magnetic field that produced them [58]. This justifies the law of energy conservation, which would not be fulfilled if both magnetic fields have equal direction. The electromagnetic force exerted on the conductor, i.e., the Lorentz force that acts on a point charge in the conductor, has been derived in [61].

In the 1970s studies of forces exerted on moving coils and magnets above an electrically conducting non-ferromagnetic slab have been extensively performed in the framework of the development of magnetic levitated transport systems [7,19,55,57,93,94]. The studies investigated linear moving planer objects and rotating cylinders. Later on, the author in [99] provided a comprehensive analysis of the Maxwell's theory for electromagnetic suspension with special focus on motion induced eddy currents and forces. Recent theoretical studies of the force acting on a magnetic dipole positioned above a slowly moving conductor have been performed in [117].

LET is a modification of ECT. Both methods are based on the principle of inducing eddy currents in the conductor, whereas the fundamental difference consists in the excitation of the primary magnetic field (Figure 2.1).

In conventional ECT, an excitation coil, which carries alternating current and has to be actively operated, provides the primary magnetic field. Moreover, the material under test is usually stationary. The signals measured are changes in the impedance in a pick-up coil. A limitation of ECT is the frequency-dependent skin depth which restricts the method to defects lying close to the surface.

Contrary to ECT, the primary magnetic field in LET, is generated by the permanent
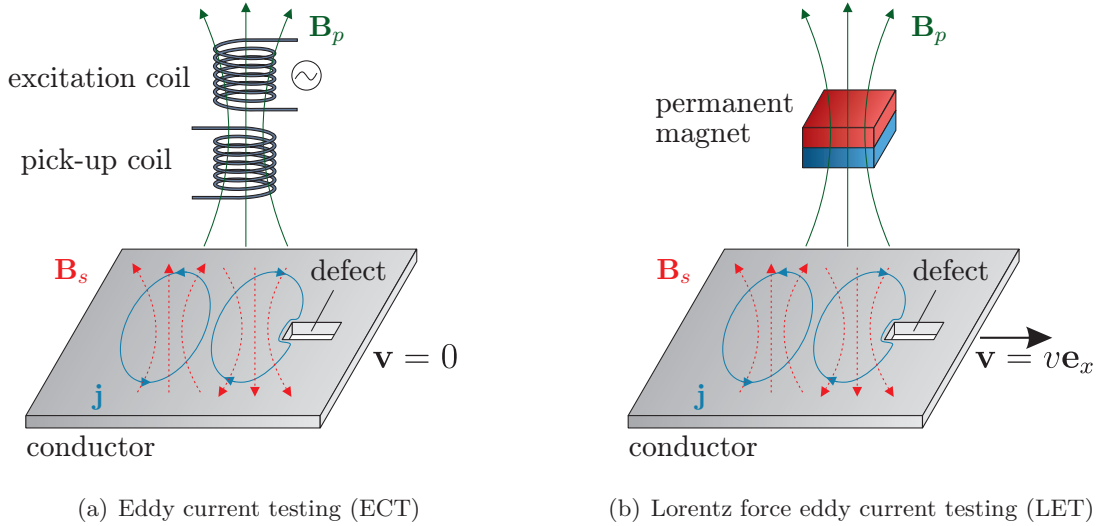
(a) Eddy current testing (ECT)

(b) Lorentz force eddy current testing (LET)

Figure 2.1: Comparison of ECT and LET working principles. The primary and induced magnetic field are denoted by $\mathbf{B}_p$ and $\mathbf{B}_s$, respectively. The induced eddy currents $\mathbf{j}$ are marked with blue color. In ECT the conductor is at rest, whereas in LET it moves with the velocity $\mathbf{v} = v\mathbf{e}_x$.

magnet, i.e., does not require any external operation.The impedance measurements are replaced by measuring Lorentz forces on the permanent magnet. Since eddy currents induced in the conductor are resulting from the relative motion, LET is especially suitable for investigating moving objects. Further, it has been observed that the relative motion yields a skin effect like behavior [16]. However, this effect is much less limiting than the frequency-depending skin-depth in ECT .

Another electromagnetic NDT method, which is relatively closely related to LET is motion induced ECT. This technique has been introduced to overcome the frequency dependent skin depth in classical ECT [109]. In this modification a stationary magnetic field is provided by a coil carrying a direct current and the conductor is in motion. Another modification of LET called velocity induced eddy current testing has been proposed [96]. This method incorporates motion induced eddy currents in a conductor underneath a permanent magnet, but instead of force signals, changes in the secondary magnetic field generated by the induced eddy currents are measured using Hall sensors.

A popular academic approach to explain the physics underlying LET is the creeping magnet problem [21, 40, 113], where the motion of a small spherical permanent magnet traveling in an electrically conducting pipe is investigated. Due to the movement eddy currents are induced in the pipe. The resulting Lorentz forces exerted on the permanent magnet reduce the velocity of the falling magnet. This example is extended to ring magnets in [122], where a falling permanent magnet ring surrounds the conductor.

Further, the Lorentz force principle is used in the Lorentz force velocimetry (LFV) to measure the velocity in an electrically conducting fluid. In this contactless method, a fluid moves across the magnetic field provided by a permanent magnet [110, 111]. Even more, in

Lorentz force sigmometry the electrical conductivity of metals or fluids is determined by exploiting the dependence between the conductivity and the magnitude of the measured Lorentz force [114].

The evaluation technique Lorentz force evaluation (LFE), which has been introduced for inverse calculations of LET signals in [81], encompasses only one forward and one reconstruction method. The authors have indicated that LET and LFE have great potential for investigating defects in laminated composites.

The remainder of this chapter is structured as follows. First, in Section 2.2 the structure and potential flaws of laminates composites are explained, because in this thesis LET and LFE focus thereon. In the following Section 2.3, the underlying physical principles and the experimental realization of LET are described. Then, in Section 2.4 procedures for solving the forward problem in LFE are explained. This includes the theory of electric and magnetic field calculations. In particular, the existing semi-analytic forward calculations are explained and a brief outline on numerical methods is given. In the last part of this chapter, Section 2.5, an overview on inverse calculation methods is given. The fundamental basics and differences of various methods are outlined. Thereby, the focus lies on the reconstruction methods applied in this thesis.

2.2 Laminated Composites

A composite is a material that is composed of two or more constituent materials. One subgroup of composite materials are fiber-reinforced composites that consist of fibers embedded in a polymer or metal matrix. A second class are laminates that consist of a set of thin sheets of different materials bounded together. These can be metal alloys, polymers, or composites themselves. A special type, the fiber metal laminates, are hybrid composite structures made of alternating layers of a metal, mostly an aluminum alloy, and an adhesive fiber-reinforced epoxy resin.

All materials in a composite remain separate and distinct, and retain their physical and mechanical characteristics. However, their combination has superior properties including higher bearing and tensile strength, better damage and fatigue tolerance, larger corrosion resistance, and less weight [63]. Due to these outstanding features composite materials are increasingly used in weight-critical components, where high stiffness is required. Fields of application comprise naval architecture, aerospace, railway supply, automotive industry, paneling of buildings, and sporting goods. Nowadays, the airframes of commercial airplanes comprise by more than half of advanced composites. Widely applied are carbon fiber-reinforced plastics. Moreover, the use of the glass laminate aluminum reinforced epoxy (GLARE), a fiber metal laminate, in the fuselage panels of the Airbus A380 is especially popular [124]. Furthermore, sandwich-structured laminates namely Hylite and Alucobond, which have metal cover layers and a plastic core layer, are used for inner and outer panelling of trucks, ships and trailers.

During the manufacturing process, material abnormalities such as porosities and debonding of sheets can arise. Further, defects can occur during life cycle, because materials are exposed to high stress. External impacts such as lightning strokes, bird strikes, and stone chipping can give rise to surface damages. Moreover, with increasing operating time composites wear out and the strength and durability are reduced. Fatigue cracks are the consequence. Early fatigue damages usually occur in the subsurface microstructure of the material. Most likely cracks occur in the area close to welding seams and riveted joints. Modes of failures include fiber breaking and matrix cracking in the fiber-reinforced matrix, and cracks in metal layers. Ongoing in-service load yields propagation of the defects.

In transport systems material failure during operation can have significant safety implications. Therefore, quality standards are very high and regular in-service inspections and maintenance are required to comply them. Large impact damages on the surface can be visually identified. In order to detect small and subsurface defects high-resolution NDT methods are required. Ultrasonics is most widely applied to check composites after manufacturing and during in-service controls of airplanes. Another common method for these purposes is ECT [105].

Further, LET and LFE are suitable to detect and reconstruct defects occurring in electrically conducting parts of composites, because the working principle of LET is based on eddy currents induced in electrically conducting materials. Thus, LET can be applied to fiber-reinforced composites with a metal matrix and those with electrically conducting fibers in a polymer matrix such as carbon fiber-reinforced plastics. However, due to the fibers and their directed orientation the material is highly anisotropic. This impedes significantly the modeling of the material, which is inevitable for fundamental research. Further, LET has great potential to inspect abnormalities in the metal layers of laminates. The single metal layers are made of monolithic material and have isotropic electrical conductivities. Based on the outlined aspects, the focus of this thesis lies on applying LET and LFE to identify and classify fatigue fractures in the metal layers of laminated composites.

In order to model a laminated composite in the laboratory setup, a set of stacked metal sheets is used. The sheets are not bonded together and thus they are interchangeable [9]. Due to oxidation during the manufacturing process, the sheets are covered by a low conductive oxide layer. This oxide layer provides an electrical isolation between the sheets and thus simulates the intermediate layers in a laminate. In order to prove this, experimental results have been compared with additional measurements, where insulation paper with a thickness of $6\,\mu m$ was placed between the metal sheets. Defects in the metal layers can be realized by drilling holes of desired size and shape in the layer. The stacking of sheets further allows to easily vary the depth of a defect by exchanging the order of layers with and without a defect.

2.3 Lorentz Force Eddy Current Testing

The schematic setup of a LET benchmark problem is shown in Figure 2.2(a). In LET, a electrically conducting non-ferromagnetic test specimen moves relative to a permanent magnet. The permanent magnet has the magnetization $\mathbf{M}$ and is positioned at the liftoff distance δz. The specimen is composed of a set of stacked aluminum alloy sheets with the dimensions $L_c \times W_c \times H_c$ and the conductivity σ_0. The height of a single sheet is denoted by Δz. The global coordinate system is positioned on the top surface of the conductor with the z-axis being perpendicular thereto. Within this coordinate system the permanent magnet is fixed and the specimen moves in x-direction with the velocity $\mathbf{v} = v\mathbf{e}_x$. One subsurface layer contains a defect of height Δz, i.e., a defect is a hole in an aluminum sheet. The depth of the flaw is denoted by d and refers to the z-coordinate of the top surface of the defective layer.

(a) Principle setup

(b) Scanning area and examples of force signals
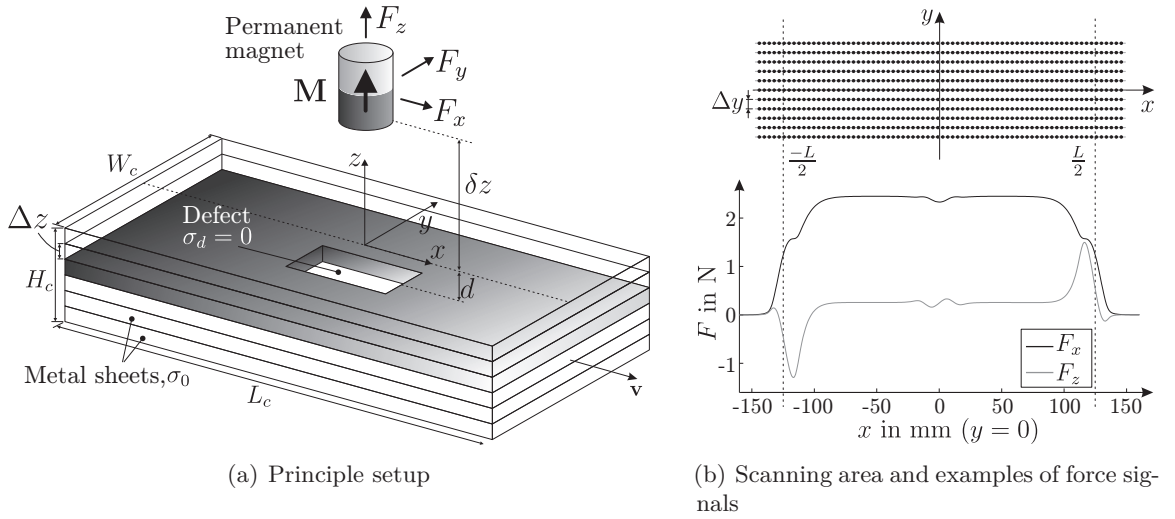
Figure 2.2: Schematic of LET measurements.

If the conductor is in motion within the magnetic field, Faraday's law of induction applies and eddy currents are induced in the conductor. The eddy currents flow in closed paths perpendicular to the magnetic field. The interaction between the eddy currents $\mathbf{j}$ and the resulting magnetic field $\mathbf{B}$, which is the sum of the primary magnetic field provided by the permanent magnet and the secondary field induced by the eddy currents, results into a Lorentz force

$$\mathbf{F} = \int_V \mathbf{j} \times \mathbf{B} \, dV, \tag{2.1}$$

with V being the volume of the conductor. This force acts on the conductor and brakes down its motion. Taking into account Newton's third law, the force of equal magnitude but opposite direction acts on the source of the applied magnetic field, i.e., the permanent magnet system: $\mathbf{F}_p = -\mathbf{F}$.

Force signals are measured at the permanent magnet in all three directions of the Cartesian coordinate system. In all applications discussed in this thesis Lorentz forces are measured along lines distributed in a xy-plane constituting the scanning area (Figure 2.2(b)). Scanning lines are specified by a fixed y-coordinate and varying x-coordinate. The coordinates refer to the xy-position of the center of gravity of the moving conductor in the global coordinate system. It has to be noted that the same scanning points can be obtained by moving the permanent magnet instead of the conductor. The exemplary force signals shown in Figure 2.2(b) are obtained at the symmetry line ($y=0$) from a conductor that has the length $L_c=250$ mm and contains a cuboidal defect of the dimensions $d_x \times d_y \times \Delta z = 12$ mm $\times$ 2 mm $\times$ 2 mm in the second metal layer. Please note that F_y vanishes at the symmetry line. It is clearly visible that the slopes in the force signals correspond to the edges of the specimen.

The information content of the force perturbations about the defect properties is determined by the sampling frequency, the velocity, and the shape and size of the applied permanent magnet. The choice of the permanent magnet is especially crucial [127]. In the first stage of complexity, one single permanent magnet as shown in Figure 2.2(a) is applied. The permanent magnet can be of cylindrical or cuboidal shape and has a magnetization in z-direction $\mathbf{M} = M\mathbf{e}_z$. Currently applied permanent magnets in the experimental setup are neodym iron boron (NdFeB) magnets of grades N35 and N38. The grade number corresponds to the maximum energy product BH_{max} expressed in the centimeter gram second (CGS) unit Mega Gauss Oerstedt (MGOe). In a second stage of complexity, a permanent magnet system that is a combined structure of single permanent magnets is used. Within the working time of this thesis a cylindrical Halbach structure has been developed [120,123]. This structure consist of a circular array of radially magnetized arc-shaped permanent magnets, and an inner cylindrical magnet supported by a soft magnetic material.

The profile of the Lorentz force components depends on the investigated conducting object. If the conductor is free of defects and the permanent magnet is very far away from the edges of the conductor, the Lorentz force components remain constant throughout the measurement. A defect in the metal layers of the conductor yields a change of the eddy currents. Due to Ampere's law this current perturbation yields a perturbation in the magnetic field and thus in the Lorentz force. Since defects are characterized by material loss or reduced conductivity, the Lorentz force experiences a short breakdown. Measuring these perturbations is the fundamental principle of LET.

The experimental realization of the LET method, used to measure signals for LFE, is shown in Figure 2.3. The relative movement in x-direction is realized by moving the investigated specimen and not the permanent magnet. This approach is chosen, because an acceleration of the permanent magnet would result into additional forces excerted on it. If the acceleration is high, these forces are likely to interfere with the actual Lorentz force signal. The test object is positioned on a belt-driven linear drive that has a maximum velocity of 3.75 m/s and a maximum acceleration of 20 m/s^2. The repetition accuracy of the position of the conductor is lower than ±0.2 mm.
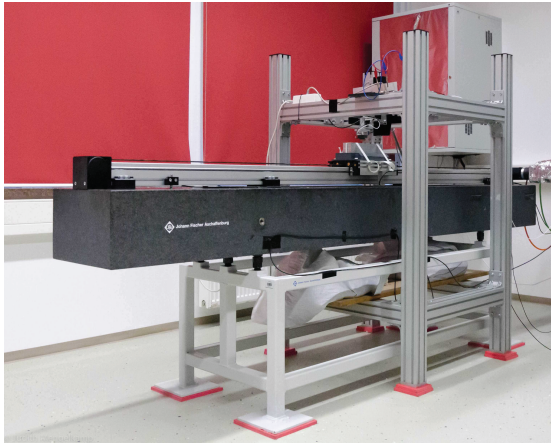
(a) Complete setup
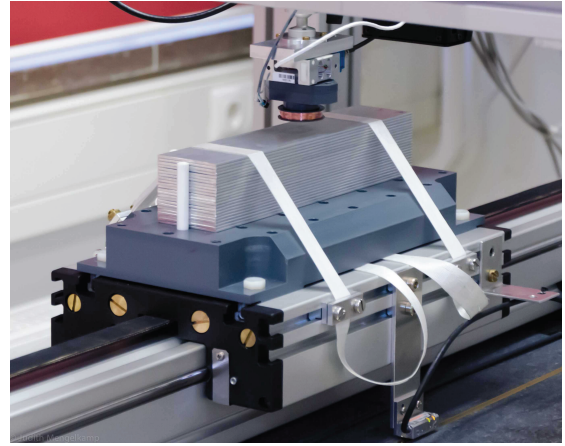
(b) Package of metal sheets positioned underneath the force sensor and permanent magnet. The permanent magnet is wrapped by a coil, which is switched off during measurements.

Figure 2.3: Experimental setup of LET.

The three-component force sensor is based on strain gauge technology. According to the data sheet [67], it has a nominal measurement range of $3\,N$ in x- and y-direction, and $10\,N$ in z-direction. The nominal accuracy equals $15\,mN$ in x- and y-direction, and $50\,mN$ in z-direction. The sensor is positioned on top of the permanent magnet. During measurements, a relative displacement of the permanent magnet in y- and z-direction (liftoff distance δz) has to be enabled. Positioning in both directions is realized by mounting the permanent magnet on a two-dimensional positioning stage that is controlled by two stepper drives. The adjustment range is $45\,mm$ with an achievable accuracy of $\pm 0.05\,mm$ in either direction. The control of all devices and the data acquisition are effected electronically. The maximum sampling frequency of the embedded signal acquisition module equals $102.4\,kHz$. Since the permanent magnet and the linear drive are freely movable parts, an alignment procedure to determine the correct relative x- and y-position of the permanent magnet and the specimen has to be performed. For aligning the correlation between the slopes in the force signals and the edges of the conductor are exploited (Figure 2.2(b)). Further information on the experimental realization of LET and the alignment procedure are provided in [15, 115] and the references therein.

Limitations of LET measurements are the motion-induced skin depth, the measurement range of the applied force sensor, and the dynamic behavior of the experimental setup. The influence of these aspects on the measured force signals scales with the velocity. With increasing velocity, the skin depth decreases. Previous studies have shown that for $v = 0.5\,m/s$ defects are detectable at least up to a depth of $9\,mm$ [14]. For higher velocities the influence of deep defects on the measurements is reduced. Further, the higher the velocity, the larger is the measured Lorentz force. Thus, for high velocities, the force sensor might run into saturation. Moreover, the dynamic behavior limits the detectability of defects at high velocities. Due to the limited bandwidth of the experimental setup, the reduced rise

time results in an increase of unwanted oscillation, which interfere with the Lorentz force signals.

During measurements interfering signals and noise are likely to occur and might influence the force signals. Interfering signals can result from inaccuracies in the y-alignment of the permanent magnet and the positioning of the specimen on the linear drive. Fluctuations in the liftoff distance (z-alignment of permanent magnet) and velocity can also occur. Moreover, the oscillations of the force sensor interfere with the signal. Further, signals are affected by 50-Hz and high-frequency noise that is generated by the electronic devices. The authors in [121] address uncertainties in input parameters including liftoff distance and velocity. The results presented there can be used to improve the measurement setup. However, this is not within the scope of this thesis. This thesis focuses on the appropriate signal processing of the measured force signals. The aim is to identify and reduce interfering signals and noise as much as necessary for accurate inverse calculations.

2.4 Forward Solutions for Lorentz Force Evaluation

2.4.1 Semi-Analytic Approach

The calculation of the force signals for LFE incorporates a model of the permanent magnet, the electric field induced in the conductive specimen, and the relative movement. Principal approaches for computations of the electric and magnetic fields and Lorentz forces are of analytical or numerical nature. Analytical computations have a higher accuracy than numerical simulations and require in the majority of cases significantly less computation time. However, analytic approaches are often based on simplified models. Since inverse calculations are often performed using iterative optimizations, forward calculations with fast computing times are favorable for LFE. However, eddy currents induced in a three-dimensional conductor that contains a defect can only be calculated in a semi-analytic way. Thus, solutions for the force signals of LET systems can only be approximated.

A first approximation of the Lorentz forces has been developed in 2013 [81]. This forward solution was expanded in 2015 using the so-called extended area approach (EAA) yielding a more accurate approximation of the force signals [128]. Both forward solutions have been derived under the consideration of additional conditions and simplifications, which are outlined later in this section.

For forward calculations only modeling of the perturbations in the force signals is of interest, because all available information about the defect is incorporated in these signals. Therefore, the so-called defect response signal (DRS) $\Delta\mathbf{F}$ is considered. The DRS is the difference between the force signals measured for a specimen with a defect and without a defect, i.e., $\Delta\mathbf{F} = \mathbf{F} - \mathbf{F}_0$. Similarly, a defect response eddy current distribution (DRCD) can be defined, i.e., $\Delta\mathbf{j} = \mathbf{j} - \mathbf{j}_0$, with $\mathbf{j}$ and $\mathbf{j}_0$ denoting the eddy currents in a conductor with and without a defect [70]. A similar approach has been used for modeling of eddy currents in ECT [75, 86].

In the proposed forward approximations only permanent magnets of simple geometries

and no permanent magnet systems combining several permanent magnets are considered. Using the simplest possible approximation, the permanent magnet is represented by a single magnetic dipole positioned at $\mathbf{r}_p = [x_p, y_p, z_p]^\mathsf{T}$ (Figure 2.4(a)). The magnetic dipole has the magnetic moment $\mathbf{m} = m\mathbf{e}_z = MV_p\mathbf{e}_z$, with V_p denoting the volume of the permanent magnet. The magnetic dipole produces at any point $\mathbf{r} = [x, y, z]^\mathsf{T}$ the magnetic flux density

$$\mathbf{B} = \frac{\mu_0}{4\pi}\left[3\frac{\mathbf{m}\cdot(\mathbf{r}-\mathbf{r}_p)}{|\mathbf{r}-\mathbf{r}_p|^5}(\mathbf{r}-\mathbf{r}_p) - \frac{\mathbf{m}}{|\mathbf{r}-\mathbf{r}_p|^3}\right]. \tag{2.2}$$

The development and application of more complex models for the permanent magnet is one of the subjects of this thesis and discussed in Chapter 3.

(a) First approximation: voxels in the defect region

(b) Extended area approach: additional voxels outside the defect region

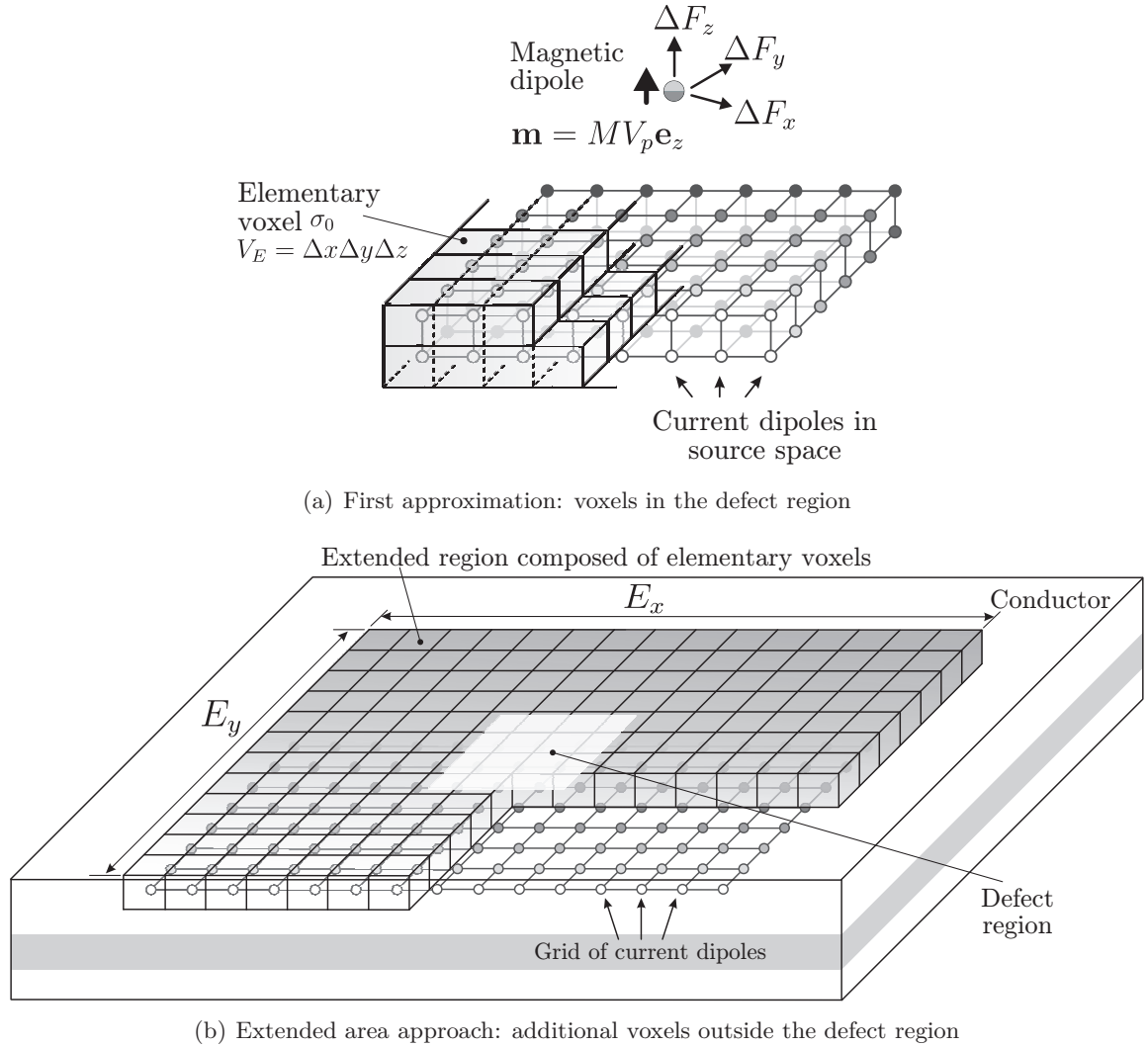Figure 2.4: Forward models for LFE.

In the proposed semi-analytic forward solutions, it is assumed that the magnetic Reynolds number $R_\mathrm{m} = \mu_0\sigma_0|\mathbf{v}|L$, with L being the characteristic length, is much less than one. The magnetic Reynolds number is a dimensionless quantity that is a measure of the relation between the primary and secondary magnetic field. Previous investigations have

shown that the condition outlined above is fulfilled for specimens, that have a characteristic length of $L = H_c \leqslant 50\,\mathrm{mm}$ and are composed of aluminum alloys, as long as the relative velocity is not larger than $0.5\,\mathrm{m/s}$ [127]. As a consequence, the influence of the secondary magnetic field resulting from the induced eddy currents on the total magnetic field can be neglected (weak reaction approach (WRA)). Thus, the magnetic field in the conductor can be reduced to the primary magnetic field of the permanent magnet. A validation of the WRA for low velocities is presented in Appendix B using the finite element method as a reference solution. In this thesis LFE studies are considered only for low velocities, since otherwise the limitations of the LET measurements as outlined in Section 2.3 are likely to have noticeable effects.

Moreover, defects are assumed to be ideal, i.e., the conductivity of the defect equals zero and no eddy currents flow in the defect region. Further, the forward solutions do not take into account the boundary conditions at the edges of the conductor, i.e., the conductor is considered to have infinitively large x- and y-extension. This simplification holds if the defect is much smaller than the conductor, $\{d_x, d_y\} \ll \{L_c, W_c\}$. Taking into account the WRA and the fact that with respect to the global coordinate system the conductor is in motion (Figure 2.2(a)), eddy currents can be calculated using Ohm's law for moving conductors

$$\mathbf{j} = \sigma \left(-\nabla \varphi + \mathbf{v} \times \mathbf{B} \right), \tag{2.3}$$

where φ is the electric scalar potential.

With V and V_d denoting the volume of the conductor without defect and the volume of the defect, the forces $\mathbf{F}$ and $\mathbf{F}_0$ exerted on the conductor can be calculated as

$$\mathbf{F} = \int_{V-V_d} \mathbf{j} \times \mathbf{B} dV, \quad \mathbf{F}_0 = \int_V \mathbf{j}_0 \times \mathbf{B} dV. \tag{2.4}$$

Using the superposition principle and rearranging the resulting equation, the DRS can be calculated by splitting the terms into defect region and the surrounding region as

$$\Delta \mathbf{F} = -\int_{V_d} \mathbf{j}_0 \times \mathbf{B} dV + \int_{V-V_d} (\mathbf{j} - \mathbf{j}_0) \times \mathbf{B} dV = \int_V \Delta \mathbf{j} \times \mathbf{B} dV. \tag{2.5}$$

Omitting the second term in equation (2.5) and using Ohm's law, the remaining term provides a first approximation of the DRS [81]

$$\Delta \mathbf{F}^{(1)} = -\int_{V_d} \mathbf{j}_0 \times \mathbf{B} dV = \sigma_0 \int_{V_d} (\nabla \varphi - \mathbf{v} \times \mathbf{B}) \times \mathbf{B} dV. \tag{2.6}$$

For this first approximation the real defect region of conductivity $\sigma_d = 0$ is substituted with the electric conductivity σ_0 and forms a fictitious conducting region. The eddy currents are only considered in the defect region and flow in exact opposite direction as for a conductor without a defect, i.e., $\Delta \mathbf{j} = -\mathbf{j}_0$.

In order to calculate $\Delta \mathbf{F}^{(1)}$, a finite volume discretization of the fictitious conducting defect region is applied. The defect region is substituted with a regular grid of volume elements, i.e. voxels, where voxel = VOlume $\times$ ELement. The voxels have the elementary volume $V_E = \Delta x \Delta y \Delta z$ and conductivity σ_0 (Figure 2.4(a)). In each voxel, a current dipole $\mathbf{p}_k$ is placed at the center of gravity described by $\mathbf{r}_k = [x_k, y_k, z_k]^\mathsf{T}$ with $k = 1 \ldots K$, where K denotes the number of voxels. The entirety of all current dipoles is a discrete approximation of the continuous eddy current distribution in the defect region. The moment of the k-th current dipole equals $\mathbf{p}_k = \Delta \mathbf{j}_k V_E$. The eddy current density $\Delta \mathbf{j}_k$ can be calculated with the help of Ohm's law for moving conductors in equation (2.3) as

$$\Delta \mathbf{j}_k = \sigma \left(\nabla \varphi_k - \mathbf{v} \times \mathbf{B}_k \right), \tag{2.7}$$

where $\mathbf{B}_k$ is the magnetic flux density at the position of the k-th current dipole calculated using equation (2.2). Although more layers of voxels as shown in Figure 2.4(a) are possible to use, throughout the whole thesis only one layer of voxels is applied to represent a single metal sheet in the laminate. Thus, the height of the voxels equals the height of the metal sheet. This is justified by the fact that a defect is considered as a hole in the sheet.

In order to find an analytic expression for φ_k calculated in equation (2.7), it is exploited that the interfaces between the metal layers are electrically isolating and $\Delta z \ll \{L_c, W_c\}$. The conductor is assumed to be anisotropic, i.e., the diagonal conductivity tensor $[\boldsymbol{\sigma}] = \mathrm{diag}\,(\sigma_{xx}, \sigma_{yy}, \sigma_{zz})$ has the entries $\sigma_{xx} = \sigma_{yy} = \sigma_0$ and $\sigma_{zz} = 0$. Thus, the eddy currents flow only in the $xy-$planes and the z-component vanishes, i.e., $j_z = 0$. Under the condition that the permanent magnet is modeled with one magnetic dipole, the potential φ_k at the point $\mathbf{r}_k = [x_k, y_k, z_k]^\mathsf{T}$ can be determined from $\partial \varphi / \partial z = v B_y$ as

$$\varphi_k = v \int\limits_{-\infty}^{z} B_{k,y} dz = -vm \frac{\mu_0}{4\pi} \frac{y_k - y_p}{|\mathbf{r}_k - \mathbf{r}_p|^3}. \tag{2.8}$$

Then, the DRS profile can be approximated with the help of the electric current dipoles as

$$\Delta \mathbf{F}^{(1)} = \int\limits_{V_d} \Delta \mathbf{j} \times \mathbf{B} dV \approx V_E \sum_{k=1}^{K} \Delta \mathbf{j}_k \times \mathbf{B}_k$$

$$= \sigma_0 V_E \sum_{k=1}^{K} \left(\nabla \varphi_k - \mathbf{v} \times \mathbf{B}_k \right) \times \mathbf{B}_k. \tag{2.9}$$

In the first approximation of the DRS $\Delta \mathbf{F}^{(1)}$ the continuity equation $\nabla \cdot \mathbf{j} = 0$ at the boundaries of the defective regions is not fulfilled. The influence of a defect on the eddy current distribution in the region surrounding the defect is not taken into account. Due to this simplification, deviations in the Lorentz forces from measured signals occur. However, the first approximation can be easily applied if more than one defect is present in the conductor, because the DRCD in the defect regions do not influence each other. The eddy

current distribution outside a defect is influenced by all defects present in the material.

In order to improve the forward solution the extended area approach (EAA) has been introduced [128]. For the extended approximation of the DRS, both terms in equation (2.5) are considered. The DRCD $\Delta\mathbf{j} = \mathbf{j} - \mathbf{j}_0$ in the second term represent the eddy currents in the area outside the defect produced by current dipoles in the defect region.

Figure 2.4(b) shows the regular grid of voxels approximating the defect region. It has the dimensions $E_x \times E_y \times \Delta z$. Current dipoles in the K voxels covering the defect region are calculated as described beforehand. The distortion current density $\Delta\mathbf{j}_e$ of the e-th current dipole in the extended region outside the defect can be approximated by

$$\Delta\mathbf{j}_e \simeq \xi_D \frac{V_E}{2\pi\Delta z} \sum_{k=1}^{K} \left[2\frac{\Delta\mathbf{j}_k \cdot (\mathbf{r}_e - \mathbf{r}_k)}{|\mathbf{r}_e - \mathbf{r}_k|^4} (\mathbf{r}_e - \mathbf{r}_k) - \frac{\Delta\mathbf{j}_k}{|\mathbf{r}_e - \mathbf{r}_k|^2} \right], \tag{2.10}$$

with $e = 1 \ldots E$, and E denoting the number of dipoles outside the defect. The scalar coefficient ξ_D is the dipolar correction factor. Based on an analysis of several cuboidal and elliptic cylinder shaped defects it has been found that ξ_D can be approximated by

$$\xi_D \simeq \begin{cases} 1 + \frac{\pi}{4}\frac{d_x}{d_y} & \text{for a cuboidal defect} \\ 1 + \frac{d_x}{d_y} & \text{for an elliptic cylinder defect} \end{cases}, \tag{2.11}$$

where d_x and d_y denote the x- and y-extension of the defect in case of a cuboidal flaw, and the length of the main axes in case of an elliptic cylinder defect [128].

Finally, the DRS can be approximated with respect to equation (2.9) as

$$\Delta\mathbf{F}^{(2)} = \int_V \Delta\mathbf{j} \times \mathbf{B}dV$$

$$\approx \underbrace{\sum_{k=1}^{K} \Delta\mathbf{j}_k \times \mathbf{B}_k dV}_{\text{defect region}} + \underbrace{\sum_{e=1}^{E} \Delta\mathbf{j}_e \times \mathbf{B}_e dV}_{\text{region outside defect}}. \tag{2.12}$$

Generally, equation (2.12) is restricted to conductors that contain only one defect or several defects, which are far away from each other. Derivations for eddy currents outside the defect region for multiple defects lying close together are challenging and have not been done yet.

The DRS for different measurement points within the scanning area is calculated by changing the position of the permanent magnet with respect to the global coordinate system (Figure 2.2(b)). Despite this aspect forward calculations are performed as outlined for moving conductors.

The improvement due to the EAA is quantified by analyzing the LET benchmark problem for two different defects [9]: a cuboidal one with dimensions $d_x \times d_y \times \Delta z = 6\,\text{mm} \times 2\,\text{mm} \times 2\,\text{mm}$ and a cylindrical one with radius $r_d = 2.5\,\text{mm}$ and height $\Delta z = 2\,\text{mm}$. Both defects are positioned at a depth of $2\,\text{mm}$. The equivalent magnetic dipole has the

moment $\mathbf{m} = \mu_0 M = 1.17\,\text{T}$ and is positioned at the liftoff $\delta z = 8.5\,\text{mm}$ above the conductor. The velocity of the specimen is set to $0.5\,\text{m/s}$ and its conductivity equals $\sigma_0 = 30.61\,\text{MS}$. The voxel dimensions are $\Delta x = \Delta y = 0.5\,\text{mm}$ and the extended region was spanned in the range $-E_x/2 \leqslant x \leqslant E_x/2$ and $-E_y/2 \leqslant y \leqslant E_y/2$ with $E_x = E_y = 30\,\text{mm}$.

Figure 2.5 shows the distribution of distortion eddy currents $\Delta \mathbf{j}$ in the defect region (light gray) and in the extended region outside the defect (dark gray) for both defect geometries. The distributions are calculated in the xy-plane for the center of the defect ($d = -3\,\text{mm}$) at the time where the magnetic dipole is positioned just above the center of the defect ($x_p = y_p = 0$). For better visualization the axes are limited to the range $-5\,\text{mm} \leqslant (x, y) \leqslant 5\,\text{mm}$. It can be observed that the continuity equation $\nabla \cdot \mathbf{j} = 0$ is not fulfilled, if only eddy currents in the region covering the defect are taken into account for forward simulations (light gray).

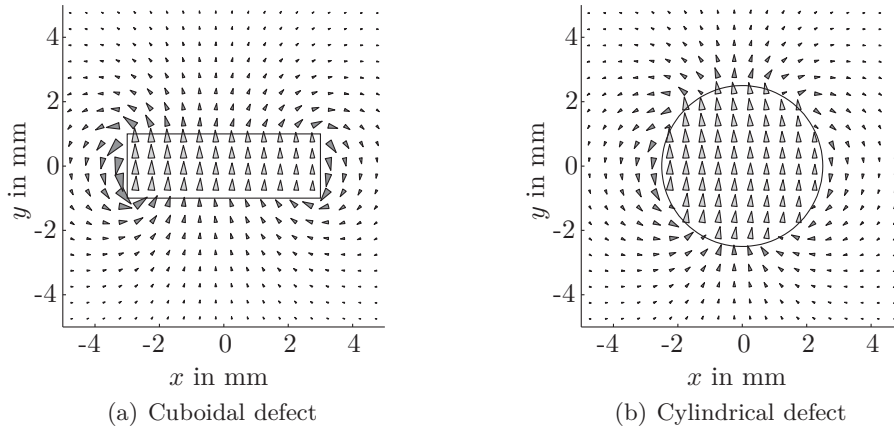(a) Cuboidal defect   (b) Cylindrical defect

Figure 2.5: Defect response eddy current distribution (DRCD) $\Delta \mathbf{j}$ in the defect region (light gray) and extended region (dark gray).

In Figure 2.6, the DRS profiles of ΔF_x and ΔF_z at the symmetry line of the defect ($y = 0$) are compared with results of numerical simulations. Please note that ΔF_y equals zero at the symmetry line and is not shown. Comparing (a) and (b) with (c) and (d), it can be observed that the forward calculations with EAA provide a significantly improved solution for the force signals.

In order to quantify the errors of the used approximations a normalized root mean square error (NRMSE) is introduced as

$$\text{NRMSE} = \frac{\sqrt{\frac{1}{3M} \sum_{i=1}^{3} \sum_{m=1}^{M} \left(\Delta F_{i,m}^{(1,2)} - \Delta F_{i,m}^{(\text{S})} \right)^2}}{\max_{m=1\ldots 3M} \left(\Delta \mathbf{F}^{(\text{S})} \right) - \min_{m=1\ldots 3M} \left(\Delta \mathbf{F}^{(\text{S})} \right)}, \tag{2.13}$$

with M denoting the number of observation points. The superscripts "(1,2)" and "S" denote the forward calculated signals using the approximate solutions (equations (2.6) and (2.12))

(a) Cuboidal defect without EAA

(b) Cylindrical defect without EAA

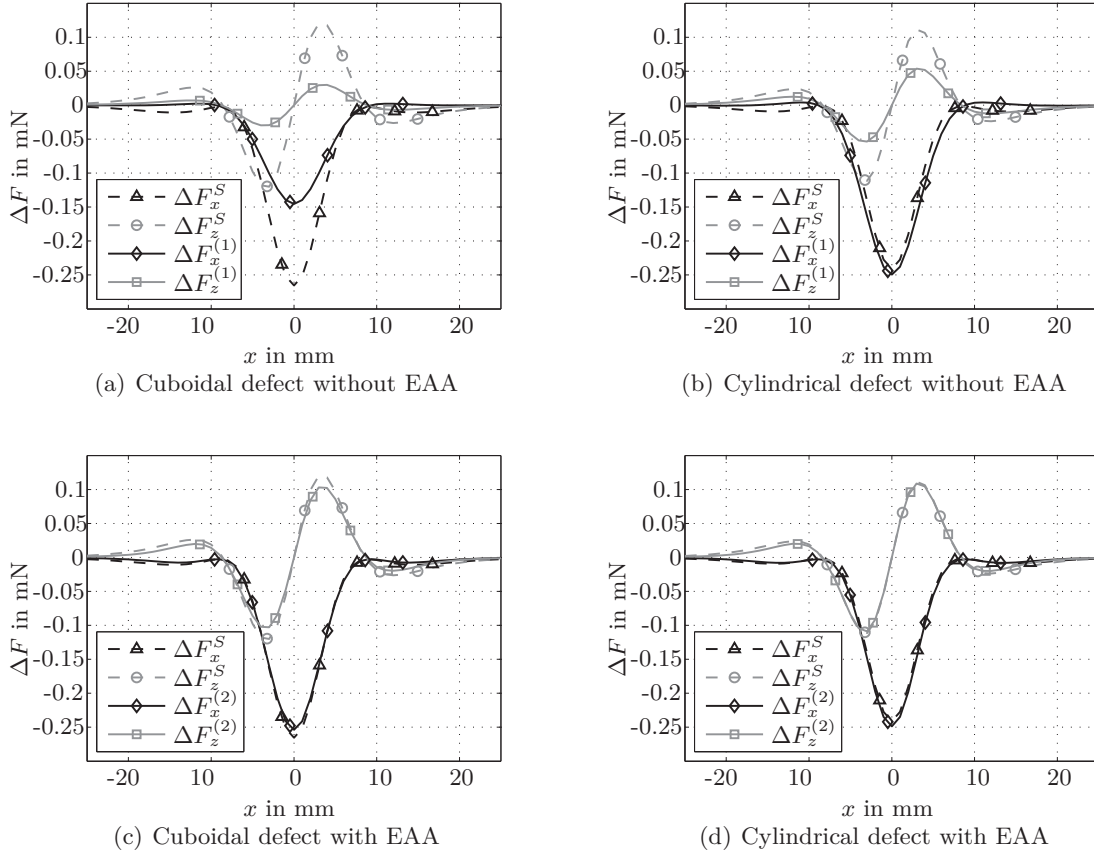(c) Cuboidal defect with EAA

(d) Cylindrical defect with EAA

Figure 2.6: Comparison of forward computed DRSs for a cuboidal and a cylindrical defect. The superscripts "(1)" and "(2)" denote the DRSs calculated with the analytic forward solution using the first approximation and the EAA, respectively. The reference DRS obtained with FEM is denoted by the superscript "(S)".

and signals simulated using a finite element model (FEM), respectively. The results summarized in Table 2.1 show that the errors for the cuboidal defect are significantly higher than for the cylindrical defect. Moreover, the further away the boundaries of the extended region are located from the defect, i.e., the larger the extended region, the smaller the error.

Table 2.1: NRMSE in % between the approximate solutions and numerical simulations.

	$\Delta \mathbf{F}^{(1)}$	$\Delta \mathbf{F}^{(2)}$
Cuboidal defect	9.52	1.57
Cylindrical defect	5.13	0.96

2.4.2 Numerical Simulations

In this thesis, numerical simulations of Lorentz force signals serve as reference solutions to quantify the approximation error of the semi-analytic approaches and as benchmark problems for the evaluation of inverse calculation methods. All numerical simulations are obtained using FEM. For FEM calculations the software COMSOL Multiphysics® is applied (COMSOL Inc., Burlington, USA).

For the implementation of the relative movement in the FEM, two methods are used: the moving magnet approach and the moving defect approach [126, 129]. In the moving magnet approach, the permanent magnet moves with respect to the global coordinate system (Figure 2.2), whereas in the moving defect approach the defect in the specimen moves.

The spatial coordinates of the moving component are modeled using the logical expressions approach [126]. This method allows fast simulations on fixed computational grids and no time-consuming re-meshing of the entire domain is necessary. The finite elements connected with the moving component for each time step are selected by evaluating the logical expressions in a predefined region in which the movement takes place.

Similarly to the semi-analytic forward solution described in the previous section, FEM calculations can be performed using the WRA [127]. In the limits of low magnetic Reynolds numbers, this approach allows a considerable reduction in the computing time without changing the accuracy of the results.

The FEM used for simulation in this thesis consists of tetrahedral elements. The maximum element size depends on the dimensions of the used components. The Galerkin method is used for numerical computations [80].

2.5 Inverse Calculation Methods

2.5.1 Classification of Inverse Problems

Inverse problems are solved in order to obtain insight into the underlying system parameters based only on the observed output data. This is extremely useful in a wide range of engineering issues. For instance, in geological prospecting the properties of the interior structure of the earth such as density and conductivity are determined based on measurements performed on the surface. In medical imaging, computer tomography is used to examine the interior structure of the human body. The attenuation of x-rays by the human body are evaluated. Another example in the framework of medical diagnostics is the reconstruction of activated cortex regions in the human brain using Electroencephalography (EEG) data measured at the surface of the human head. In the inverse scattering method, the shape of an object is determined based on the waves scattered by it. In this framework acoustic and electromagnetic scattering are most widely applied [17, 52].

Inverse problems can be classified into non-linear and linear problems. Their distinction

can be well explained by considering the corresponding formulation of the forward problem

$$\mathbf{y} = \mathcal{G}(\mathbf{x}), \tag{2.14}$$

where the vector $\mathbf{y} \in \mathbb{R}^{M \times 1}$ denotes the measured signals and M is the number of measurement points. The vector $\mathbf{x} \in \mathbb{R}^{N \times 1}$ contains the N model parameters. The operator $\mathcal{G}$ represents a projection of the model parameters on the measured signals. It comprises information about the sensor and source positions and configuration. In the forward problem $\mathbf{y}$ is calculated using the known model parameters. In the associated inverse problem the model parameters are unknowns to be estimated.

If the problem is linear, equation (2.14) can be reformulated as

$$\mathbf{y} = \boldsymbol{K}\mathbf{x}, \tag{2.15}$$

with the gain matrix $\boldsymbol{K} \in \mathbb{R}^{M \times N}$ describing a linear mapping between model parameters and output data. In case of a non-linear problem, the relation between model and data values is more complex and $\mathcal{G}$ in equation (2.14) is a non-linear operator.

The properties of forward and inverse problems differ in the sense that forward problems are usually classified as well-posed, whereas inverse problems are mostly ill-posed. The definition of a well-posed and ill-posed problem dates back to Hadamard [39]. A problem is well-posed if it has the following three properties. First, the problem can be solved (existence of a solution). Second, the number of existing solutions does not exceed one (uniqueness of the solution). Third, a continuous change in the input data yields a continuous change in the solution (stability of the solution). If at least one of these criteria is not fulfilled the problem is said to be ill-posed.

Even if the stability condition is fulfilled, the inverse problem can be sensitive to noise in the data. A small change in the input data may have a significant impact on the solution. If this is the case the problem is said to be ill-conditioned [5]. The degree of ill-conditioning of the inverse problem can be determined by calculating a condition number of the gain matrix. Several condition numbers have been introduced in literature [27, 82]. The most widely used ones include the condition number with respect to the L_2-norm and the Skeel condition number. The condition of the inverse problem depends on the sensor space (the applied grid of measurement points) and the source space (the region containing the unknown parameters).

Additionally, inverse problems can be subdivided into overdetermined and underdetermined problems. An overdetermined problem has more sensor data points than unknown sources to be determined and vice versa for an underdetermined problem. Moreover, constraints can be imposed on the inverse problem. In real-world applications boundary and parameter constraints often have to be considered.

2.5.2 Solving Inverse Problems

In the inverse problem of LFE, it is the aim to characterize the geometry of the underlying defects. A straightforward approach is to solve directly for the defect parameters. Thus, defect geometry parameters such as the center of gravity, depth, and extension can be defined as the unknown variables in $\mathbf{x}$. Other approaches are to determine the eddy current distribution and the conductivity distribution in the conductor. In these reconstruction approaches, the vector $\mathbf{x}$ in equation (2.14) composes the unknown moments of the equivalent current dipoles or the unknown voxel conductivities.

Solving an inverse problem implies to minimize the error between measured $\mathbf{y}_\mathrm{m}$ and forward calculated data $\mathbf{y}_\mathrm{f}$ with respect to the unknown parameters composed in $\mathbf{x}$

$$\min_{\mathbf{x}} \left(\mathbf{y}_\mathrm{m} - \mathbf{y}_\mathrm{f}\right) = \min_{\mathbf{x}} \left(\mathbf{y}_\mathrm{m} - \mathcal{G}(\mathbf{x})\right). \tag{2.16}$$

For this purpose several inverse calculation methods can be applied. Figure 2.7 gives an overview of existing inverse methods and highlights methods used in this thesis. In order to obtain a stable solution of the inverse problem, regularization methods are applied. Regularization exploits *a priori* information of the solution and is usually performed by adding additional information in the form of weighting parameters or function terms to the error function in equation (2.16). Additional function terms are penalty terms that introduce constraints to the solution space, e.g., specific error bounds.

One class of inverse methods are scanning methods. The simplest scanning method is the goal function scanning. The value of the goal function, e.g., the error function $\mathbf{y}_\mathrm{m} - \mathcal{G}(\mathbf{x})$, is computed for different combinations of the parameters to be determined. The inverse solution is set to the parameter combination with the smallest goal function value. The method has the advantage that the course of the goal function can be scrutinized. However, the major drawback is that the method requires a large number of forward calculations, which results into a high computational cost. Thus, the goal function scanning is only feasible if the number of unknown parameters is small, i.e., only one source is to be determined. The method has already been applied to reconstruct sources in the human brain from electroencephalography and magnetoencephalography measurements [32]. In this thesis, the goal function scanning is applied to determine the depth and extensions of a defect in the GLARE material (Chapter 6). An enhancement of the goal function scanning is the multiple signal classification (MUSIC) method, which originates from information theory [76]. In this method, multiple sources are determined by scanning subspaces of the goal function with single sources. Another scanning method is beamforming, which has been developed in the field of radio communication where multiple antennas are used. The working principle of beamforming algorithms is to reduce the interference between signals coming from multiple source with a spatial filter [8].

Another approach to solve the inverse problem are minimum norm estimates (MNE). They are commonly applied to reconstruct current density distributions and especially distributed current sources. A regular grid of elementary current dipoles with fixed positions
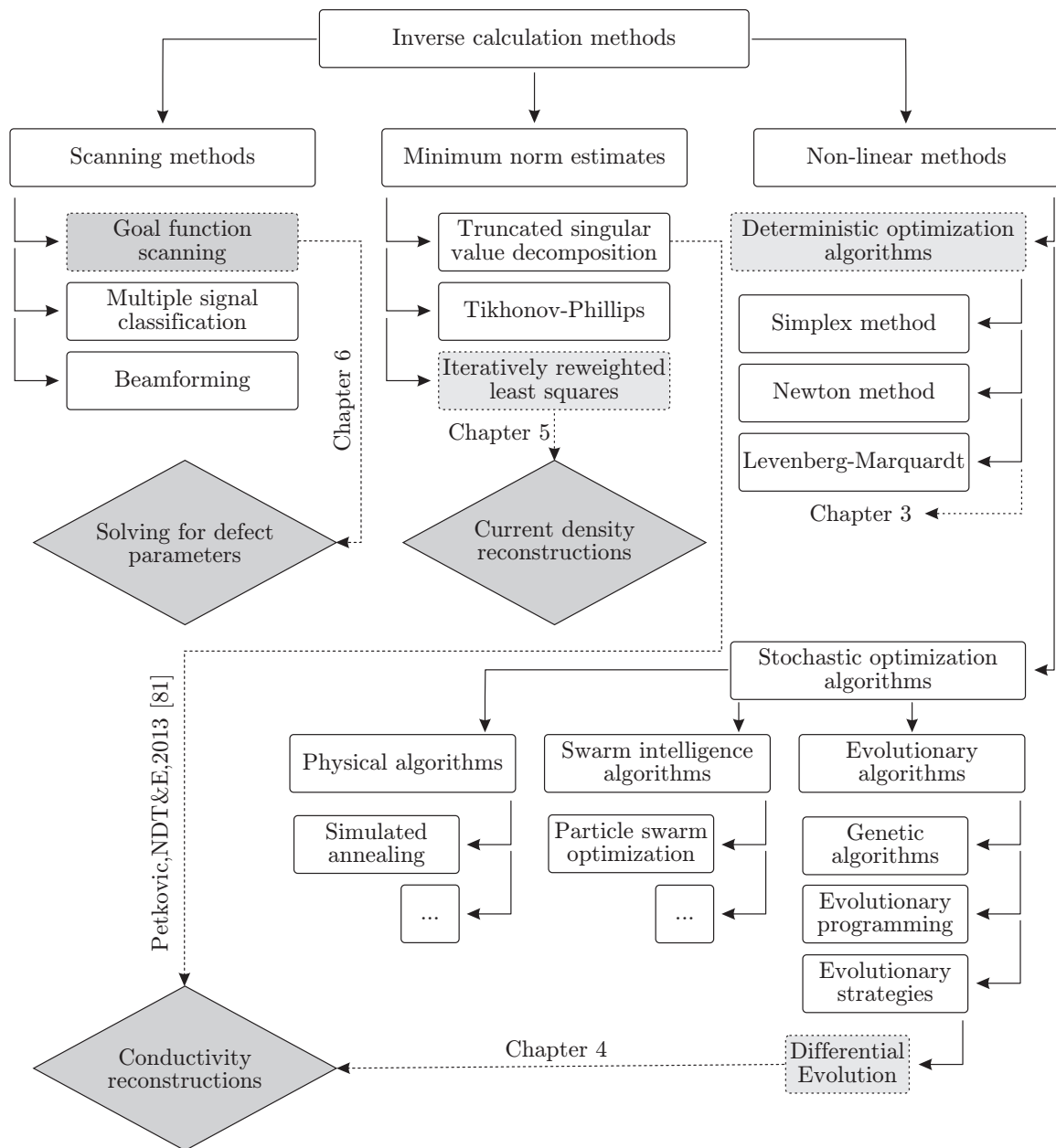
Figure 2.7: Overview of existing inverse calculation methods. Parameters that can be solved for are shown in rhombuses. Inverse methods applied in this thesis to determine these parameters are marked with light gray color and dashed lines. References to the particular chapters are given next to the arrows.

but unknown moments is defined in the region of the distributed current source. Optimal dipole moments are obtained by minimizing the norm of the vector difference between the measured data and the forward solution given in equation (2.15). Regularization is performed by constraining the solution with a norm showing the desired properties. If the L_2 norm is applied, the inverse solution tends to be smeared. Common methods to calculate the solution are the truncated singular value decomposition (TSVD) [43] and the Tikhonov-Phillips regularization [84, 112]. In the TSVD, small singular values are

omitted in order to obtain a stable solution. This approach was also used to reconstruct conductivities in the first application of LFE [81]. In Tikhonov-Phillips regularization, an additional penalty term is introduced to equation (2.16). The regularization incorporates appropriate weighting of this term with respect to the error function. If another norm than the L_2 norm is applied, the inverse solution tends to be sparse. The resulting inverse problem is nonlinear and can be solved using weighted least squares algorithms.

MNE are widely applied in biomedical engineering to localize current sources in the human brain and heart [31, 41, 56, 118]. Further, MNE have been applied in magnetic nanoparticle imaging [4] and to detect buried ferromagnetic objects based on measured magnetic fields [26]. In the framework of NDT this approach has been used to reconstruct pipeline defects from MFL measurement data [44]. Moreover, the authors in [62] applied the Minimum-L_2-norm approach to magnetic tomographic data. Further, ECT signals have been inverted with MNE to estimate flaws in metals [85]. In this thesis, MNE are applied to reconstruct the eddy current distribution $\Delta \mathbf{j}$, which is responsible for the DRS (equation (2.12) and Figure 2.5).

Another approach to minimize the error function is to use optimization techniques. They can be divided into deterministic and stochastic methods. Widely applied deterministic methods are the simplex method [78], the Newton method [87], and the Levenberg-Marquardt algorithm [59, 65]. Results of deterministic methods are reproducible provided that the search area, the starting point, and the termination criterion remain unchanged. However, they often impose constraints such as differentiability, continuousness, and convexity of the goal function. Further, they perform a local search, i.e., they are likely to be trapped by local minima if the initial values are not chosen precisely enough. In this thesis deterministic methods are used to optimize the magnetic dipoles models (MDMs) in Chapter 3.

Stochastic optimization algorithms overcome the starting point problem by defining multiple starting points on the goal function landscape. Most stochastic optimizers are zero-order algorithms, i.e., they do not depend on the derivative of the goal function. Even more, the goal function does not have to fulfill the constraints of continuity and convexity. The probability that they are trapped by local minima is smaller than for deterministic algorithms. Due to the stochastic nature results of multiple trials scatter with a small variance around the global minimum. One drawback of stochastic optimization algorithms compared to deterministic methods is that more goal function evaluations are required and thus the computational cost is higher. Further, stochastic algorithms implicate the challenge of adjusting at least one intrinsic control parameter, e.g., weighting parameters that influence the step size of the algorithm. These parameters can have a significant impact on the result.

Stochastic optimization algorithms can be classified into physical algorithms, swarm intelligence algorithms, and evolutionary algorithms (EAs). Physical algorithms adapt physical processes, e.g., the basic concept of the simulated annealing algorithm is to simulate a cooling process in metallurgy [51]. Swarm intelligence algorithms imitate natural evolution

and selection and exploit the natural collective and social behavior of swarms reaching for some target, e.g., animals searching for food. Among them, the particle swarm optimization is the most prominent member [50].

The EAs are also biologically inspired. They are based on Darwin's evolutionary theory. The theory states that a population evolves by random genetic mutation and recombination. Mutation generates innovation in the population and recombination intermingles information. Selection is determined by the survival-of-the-fittest principle. EAs can be divided into the three main branches: evolutionary strategies (ESs) [102], evolutionary programming (EP) [30], and genetic algorithms (GAs) [36, 48]. In evolutionary strategys (ESs) and EP, the objective variables are real-valued and continuous, whereas in GA they are binary. Hence, mathematical operations for evolving the population are arithmetic in EP and ESs, but logical in GAs.

In EP, only mutation is applied for offspring generation. The ESs combine mutation and recombination, and in GA recombination has priority over mutation. Traditional mutation is based on probability density functions. In EP and ESs, a survivor selection is applied, e.g., after offspring generation it is decided which population members from the combined parent and offspring population will survive to the next generation. The selection procedure in EP and GAs is based on probability functions. Contrary, in ESs selection is performed deterministically, i.e., for selecting the next generation, ranking of the individuals or a tournament selection can be applied. In traditional GAs, parent selection is performed. Prior to mutation and recombination, parents that will produce offsprings are selected based on a probabilistic approach.

Survivor selection as in EP and ESs ensures that the best-so-far solution is retained, i.e., elitism is included. In the parent selection used in traditional GAs this requirement of elitism is violated, because parents that will produce offsprings are selected before the evolution process. Since researches have evaluated that elitism has significant positive influence on the performance of an algorithm, this principle has also been incorporated in GAs [131].

Due to their advantages, stochastic algorithms are applied in the framework of non-destructive testing and evaluation (NDT&E) for inverse calculations of material defects, where the characteristics of the goal function are inherently unknown. The particle swarm optimization has been applied for defect reconstruction using ECT signals [13, 25]. For the same purpose the authors in [54] and in [60] have applied a GA and EP, respectively. In all applications conductivity reconstructions were applied to identify the defect. Moreover, ESs have been of interest in electromagnetic inverse scattering problems [66, 95] and for the analysis of composite materials [89]. In this thesis an ES, the Differential Evolution, is applied for conductivity reconstructions (Chapter 4).

3 Modeling of Permanent Magnets

3.1 Introduction

In this chapter, different modeling approaches for permanent magnets are investigated and compared. Existing models are evaluated and new models especially suitable for Lorentz force evaluation (LFE) are developed. The focus lies on developing permanent magnet models that can be applied to magnets of arbitrary shape. This is motivated by the fact that the resolution of LFE depends on the permanent magnet and future investigations aim to apply complex shaped magnets and magnet systems. This chapter contains methods and principles that have been published in [69, 72].

Fully analytic forward calculations ensuring low computational costs are intended to be maintained. Hence, it is required that the model can be embedded into the approximate forward solution for the force calculations described in Section 2.4.1. Furthermore, due to the proximity of the magnet and the specimen in LFE the near magnetic field of the permanent magnet has to be considered.

The representation of a complex-shaped magnet with one magnetic dipole as in the proposed forward solution described in Section 2.4.1 has the disadvantage that it provides an accurate solution of the magnetic field only at large distances [83]. In order to overcome this drawback analytic solutions that provide an exact description of the magnetic field can be applied [3, 20, 34, 90, 92]. Unfortunately, such solutions are challenging to derive especially for complex shaped magnets. Even if an analytic solution exist, it might not be applicable to inverse LFE calculations, because the solution cannot be embedded into the approximate forward solution. In order to overcome these limitations the magnetic dipoles model (MDM) is introduced, in which the permanent magnet is represented with an assembly of magnetic dipoles. This approach allows to model permanent magnets of arbitrary shape by appropriate placing of magnetic dipoles in the volume of the magnet. The integral of the magnetic flux density for force calculations provided by the MDM is the linear sum of the integrals of the magnetic flux density of the single magnetic dipoles in equation (2.2). Corresponding to the current experimental setup of Lorentz force eddy current testing (LET), permanent magnets of cuboidal and cylindrical shape are evaluated.

In the near field the accuracy of the approximation with one magnetic dipole depends on the form of the modeled magnet [83]. Based on this aspect, the position of the dipoles is expected to have an impact as well. Therefore, an optimization procedure to determine optimal dipole positions is developed, instead of defining the positions of the magnetic dipoles arbitrarily. The accuracy of the MDM is evaluated in comparison to a reference

solution. The MDM, that shows the minimum error among all MDMs using equal number of dipoles, has optimal dipole positions. Moreover, the influence of the number of dipoles on the accuracy of the MDM is evaluated.

Existing analytic solutions of the magnetic field are applied as reference solutions. The charge model, also referred to as the Coulombian model, provides an analytic solution of the magnetic field of the cuboidal magnet in terms of elementary functions [33, 125]. Alternatively to the charge model, a surface current model, also referred to as Amperian model, is applied for the cylindrically shaped permanent magnet. Using this model, the magnetic flux density of an axially magnetized cylindrical permanent magnet can be described with the help of generalized complete elliptic integrals [20]. In this context, a semi-analytic model of the cylindrical permanent magnet based on substituting the permanent magnet with a set of current loops is proposed.

Further, it is demonstrated how the accuracy of the model of the permanent magnet influences the exactness of the forward solution. Therefore, selected MDMs of the cuboidal permanent magnet with optimal dipole positions are embedded into the existing first approximation for forward calculated Lorentz forces for LFE and the resulting signals are evaluated. Additionally, the computational demand required by the MDMs is addressed. This is a significant factor, because it determines considerably the practicability of the permanent magnet model.

In the remainder of this chapter, the applied methods are outlined first. These include the developed MDMs, the analytic models, and the optimization procedure. Moreover, the MDM is embedded into the approximate forward solution for LFE. In Section 3.3, the results are shown, i.e., the optimized MDMs of the cuboidal and cylindrical magnet. Further, the performance of the optimization procedure and the accuracy of the forward computed Lorentz forces are evaluated. Further, the analytic and semi-analytic model of the cylindrical permanent magnet are compared and the computational demand is assessed. Finally, in Section 3.4 the results are discussed.

3.2 Methodology

3.2.1 Magnetic Dipoles Models

The idea of MDMs consists in splitting the permanent magnet into a regular grid of N_D voxels of identical volume. The shape of the voxels depends on the shape of the permanent magnet. For cuboidal magnets the voxels are cuboids, whereas for cylindrical magnets the central voxels are cylinders and the others are hollow cylinder sectors. One magnetic dipole is positioned in each voxel. The voxels have the same volume. Consequently, the magnetic moments of the inserted magnetic dipoles are equal. The dipole positions in the MDM of the cuboidal magnet depend on one parameter and, thus, the model is referred to as α-MDM. In case of the cylindrical magnet the MDM depends on two parameters ((α,β)-MDM).

α-MDM of the Cuboidal Permanent Magnet The α-MDM applied to approximate the cuboidal permanent magnet is depicted in Figure 3.1. The permanent magnet has the edge length $a = 15\,\text{mm}$, the height $H_p = 25\,\text{mm}$, the volume $V_p = a^2 H_p$, and is magnetized in z-direction with the remanence $\mu_0 M = 1.17\,\text{T}$. Further, the permanent magnet is located at the point $\mathbf{P}_0 = [x_0, y_0, z_0]^\mathsf{T} = [0, 0, \delta z]$ corresponding to the center of gravity of the lower face of the magnet, with the liftoff distance $\delta z = 1\,\text{mm}$. The edges of the magnet are parallel to the axes of the global Cartesian coordinate system.
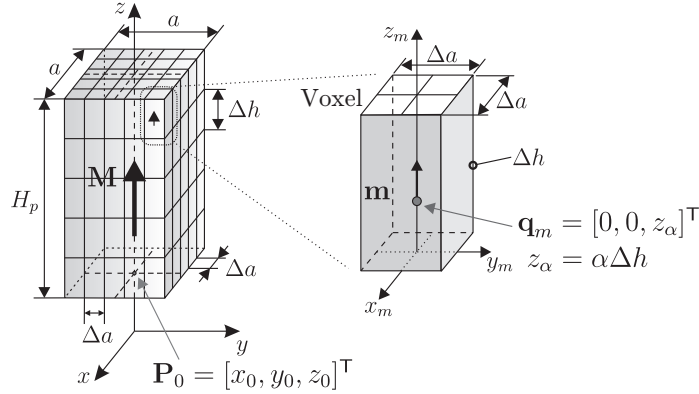

Figure 3.1: Magnetic dipoles model of a cuboidal permanent magnet.

According to the idea of the MDM, the permanent magnet is represented by a set of $N_D = N_a^2 N_h$ voxels, with N_a being the number of voxels along the base edges and N_h the number of voxels along the height edge. The volume of each voxel equals $V_E = \Delta a^2 \Delta h = (a/N_a)^2 (h/N_h) = V_p/N_D$ with V_p denoting the volume of the permanent magnet. The magnetic dipoles positioned in the voxels have the same magnetic moment $\mathbf{m} = m\mathbf{e}_z = \mathbf{M} V_p/N_D = \mathbf{M} V_E$. The magnetic flux density $\mathbf{B} = [B_x, B_y, B_z]^\mathsf{T}$ at any point $\mathbf{P} = [x, y, z]^\mathsf{T}$ outside the permanent magnet can be calculated as the linear superposition of the magnetic flux densities of all magnetic dipoles of the α-MDM

$$\mathbf{B}(x, y, z) = \sum_{m=1}^{N_D} \mathbf{b}_m(\mathbf{P}, \mathbf{Q}_m), \tag{3.1}$$

with $\mathbf{b}_m$ being the magnetic flux density of the m-th dipole located at $\mathbf{Q}_m = [x_m, y_m, z_m]^T$

$$\mathbf{b}_m = V_E \frac{\mu_0}{4\pi} \left[3\frac{\mathbf{m} \cdot (\mathbf{P} - \mathbf{Q}_m)}{|\mathbf{P} - \mathbf{Q}_m|^5} (\mathbf{P} - \mathbf{Q}_m) - \frac{\mathbf{m}}{|\mathbf{P} - \mathbf{Q}_m|^3} \right]. \tag{3.2}$$

Due to the symmetry of the cuboidal permanent magnet and the identity of all voxels it is not expected that any (x_m, y_m) position of the magnetic dipoles other than the center of gravity of the bottom and top face of the elementary voxels result in an improvement of the α-MDM. Thus, the coordinates (x_m, y_m) are fixed to this position. However, the z-coordinate of the magnetic dipoles is expected to have an impact on the model accuracy in the near magnetic field below the permanent magnet. Exploiting this aspect the

z-coordinate of the magnetic dipoles depends on a parameter $z_\alpha = \alpha \Delta h$, which defines a local z-position of the magnetic dipole in the corresponding voxel. The magnetic flux density of the α-MDM depends on a proper selection of the parameter α. Then, the position $\mathbf{Q}_m$ of the m-th magnetic dipole is defined as

$$\mathbf{Q}_m = \mathbf{P}_0 + \mathbf{q}_{ijk} + \mathbf{q}_m = \begin{bmatrix} x_m \\ y_m \\ z_m \end{bmatrix} = \begin{bmatrix} x_0 - \frac{a}{2} + (i - \frac{1}{2})\Delta a \\ y_0 - \frac{a}{2} + (j - \frac{1}{2})\Delta a \\ z_0 + (k-1)\Delta h + z_\alpha \end{bmatrix}, \begin{cases} i = 1, \dots, N_a \\ j = 1, \dots, N_a \\ k = 1, \dots, N_h \end{cases} \tag{3.3}$$

with $m = i + (j-1)N_a + (k-1)N_a^2$. The variable $\mathbf{q}_{ijk}$ denotes the position (center of gravity) of the corresponding voxel with respect to the center of gravity of the permanent magnet. Moreover, $\mathbf{q}_m$ describes the position of the magnetic dipole with respect to a local coordinate system having its origin at the center of the lower face of the corresponding voxel. The parameter α is constraint on the interval $[0,1]$ with 0 and 1 corresponding to the bottom and top face of the voxels. All magnetic dipoles in the α-MDM have an equal local position inside their respective voxel, i.e., α is equal for all voxels. In this study different α-MDM of the cuboidal permanent magnet are evaluated. They are specified by combinations of $N_a = \{2{:}2{:}14\}$ and $N_h = \{1{:}1{:}25\}$.

(α,β)-MDM of the Cylindrical Permanent Magnet The axially magnetized cylindrical permanent magnet has the radius R_p, the height H_p and the volume $V_p = \pi R^2 H_p$. It is positioned at the center of the cylinder bottom face ($\mathbf{P}_0 = [x_0, y_0, z_0]^\mathsf{T} = [0, 0, \delta z]^\mathsf{T}$) and the cylinder axis is parallel to the z-axis. The voxels in the (α,β)-MDM are of two types. The central voxels are cylinders and their main axis coincides with the main axis of the permanent magnet. The voxels off the z-axis are hollow cylinder sectors (Fig. 3.2).
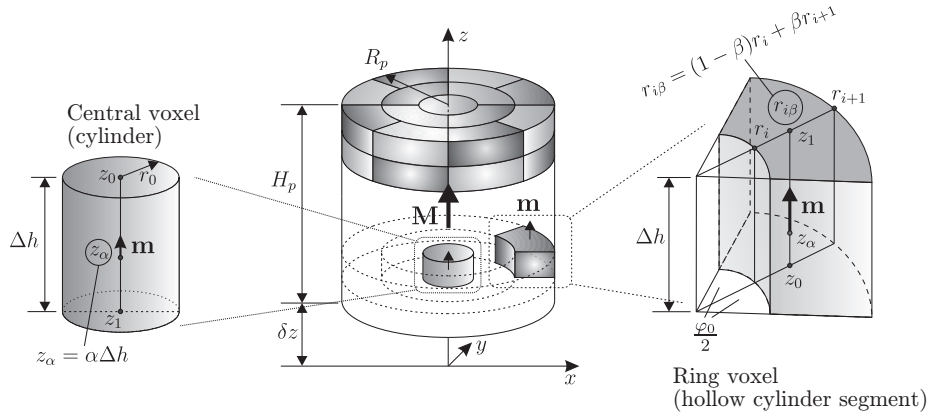

Figure 3.2: Magnetic dipoles model of a cylindrical permanent magnet.

The (α,β)-MDM is composed of N_h layers of voxels. Each layer contains one central voxel of radius r_0 and height Δh, and N_R concentric rings consisting of a number of cylinder sector voxels. These are described by the inner radius r_i, the outer radius r_{i+1} with i indexing the i-th ring of voxels, the segment angle φ, and the height Δh. The total number of magnetic

dipoles N_D is calculated as

$$N_D = N_h \left(1 + \sum_{i=1}^{N_R} N_S^i \right). \tag{3.4}$$

The variable N_S^i denotes the number of voxels in the i-th concentric ring and is defined as

$$N_S^i = N_{\text{se}} \left\lfloor \frac{\pi}{2} \left(i - \frac{1}{2} \right) \right\rfloor \geqslant N_{\text{se}}, i = 1, \cdots, N_R, \tag{3.5}$$

with N_{se} denoting the number of segments in the MDM. For a cylinder magnet $N_{\text{se}} = 4$ is chosen. Thus, N_S^i is always a multiple of 4 to ensure the symmetry of the (α,β)-MDM. The operator $\lfloor \cdot \rfloor$ denotes the greatest integer function. The magnetic dipoles in the central voxels are positioned on the cylinder main axis. Further, the radius r_0 of the central voxels is defined as

$$r_0 = \sqrt{\frac{V_E}{\pi \Delta h}}, \tag{3.6}$$

with $V_E = V_P/N_D$ denoting the volume of one voxel. The magnetic dipoles in the ring voxels are located on the symmetry plane of the corresponding voxel. Thus they are positioned at half of the segment angle spanning the ring voxel $\varphi/2$. The inner radius r_i and outer radius r_{i+1} of the voxels in the concentric rings are calculated by the following recurrence

$$r_{i+1} = \sqrt{\frac{V_E N_S^i}{\pi \Delta h} + r_i^2}, r_1 = r_0. \tag{3.7}$$

Radial and axial positions of the dipoles in the ring voxels depend on the parameters α and β, respectively. The parameters α and β are equal for all voxels and are constraint to the interval $[0, 1]$ ensuring that the dipoles are located inside the corresponding voxels. With respect to a local coordinate system placed at the center of the bottom face of the respective layer of voxels (on the z-axis), the positions of the dipoles can be summarized as

$$
\begin{aligned}
r_{i\beta} &= \begin{cases} 0, & i = 0 \quad \text{(axial voxel)} \\ (1 - \beta)r_i + \beta r_{i+1}, & i = 1, \ldots, N_R \quad \text{(ring voxels)} \end{cases}, \\
z_\alpha &= \alpha \Delta h.
\end{aligned}
\tag{3.8}
$$

Then, the position $\mathbf{Q}_m = [x_m, y_m, z_m]^{\mathrm{T}}$ of the m-th magnetic dipole in the global Cartesian coordinate system is calculated as

$$\mathbf{Q}_m = \mathbf{P}_0 + \mathbf{q}_{ijk} = \begin{bmatrix} x_m \\ y_m \\ z_m \end{bmatrix} = \begin{bmatrix} x_0 + r_{i\beta} \cos\theta_j \\ y_0 + r_{i\beta} \sin\theta_j \\ z_0 + (k-1)\Delta h + z_\alpha \end{bmatrix}, \theta_j = 2\pi \frac{j - \frac{1}{2}}{N_S^i}, \tag{3.9}$$

with $i = 1, \ldots, N_R$, $k = 1, \ldots, N_H$, and $j = 1, \ldots, N_S^i$. Further, $\mathbf{q}_{ijk}$ denotes the position of the dipole with respect to a local coordinate system placed at the center of the bottom face of the cylindrical magnet. The magnetic flux density $\mathbf{B} = [B_x, B_y, B_z]^{\mathrm{T}}$ at any point

$\mathbf{P} = [x, y, z]^{\mathrm{T}}$ outside the permanent magnet is calculated according to equation (3.1).

Figure 3.3 shows examplarily distributions of magnetic dipoles in a single layer of two (α,β)-MDMs. Dipole positions are shown for $N_R = 2, N_D = 13$ and $N_R = 6, N_D = 105$, with N_D denoting the number of dipoles in one layer.
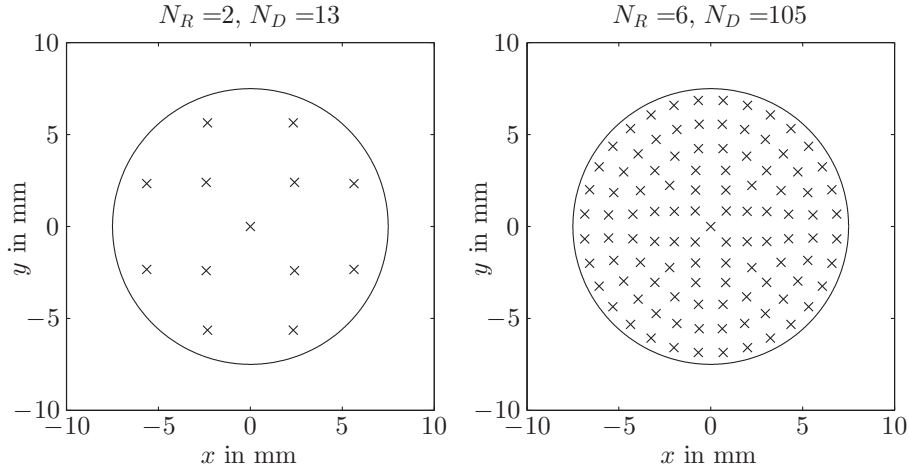

Figure 3.3: Distributions of magnetic dipoles in one layer of two (α,β)-MDMs with $N_R = 2, N_D = 13$ (left) and $N_R = 6, N_D = 105$ (right). The number of dipoles in the layer is denoted by N_D.

The permanent magnet under investigation has the dimensions $R_p = 7.5\,\mathrm{mm}$ and $H_p = 25\,\mathrm{mm}$. The liftoff distance δz equals $1\,\mathrm{mm}$. The (α,β)-MDM is assessed for different numbers of magnetic dipoles defined by all possible combinations of $N_R = \{1{:}1{:}7\}$ and $N_h = \{1{:}1{:}25\}$.

3.2.2 Analytic Models

Charge Model of the Cuboidal Permanent Magnet The charge model provides a fully analytic calculation of the magnetic flux density of the cuboidal permanent magnet at any point in space. Applying the charge model the magnet is represented by a distribution of equivalent magnetic surface charges (Figure 3.4) [33, 125]. The surface charge density is calculated as $\sigma_m = \mathbf{M} \cdot \mathbf{n}$ with $\mathbf{n}$ denoting the surface normals. Evaluating the surface normals for a cuboidal magnet with the magnetization along the z-axis $\mathbf{M} = M \cdot \mathbf{e}_z$, the surface charge density equals $\sigma_m = \mathbf{M} \cdot \mathbf{e}_z = M$ for the top face located at $z = \delta z + H_p$, and $\sigma_m = \mathbf{M} \cdot (-\mathbf{e}_z) = -M$ for the bottom face positioned at $z = \delta z$. The charge densities of the side faces vanish.

The magnetic charges are used as a source term in magnetostatic field equations. Generally, the magnetic flux density $\mathbf{B} = [B_x, B_y, B_z]^{\mathrm{T}}$ at any point $\mathbf{P} = [x, y, z]^{\mathrm{T}}$ resulting from a magnetic surface charge is calculated as

$$\mathbf{B}(\mathbf{P}) = \frac{\mu_0}{4\pi} \oint_S \frac{\sigma_m\left(\mathbf{P}'\right)\left(\mathbf{P} - \mathbf{P}'\right)}{\left|\mathbf{P} - \mathbf{P}'\right|^3} ds' \tag{3.10}$$
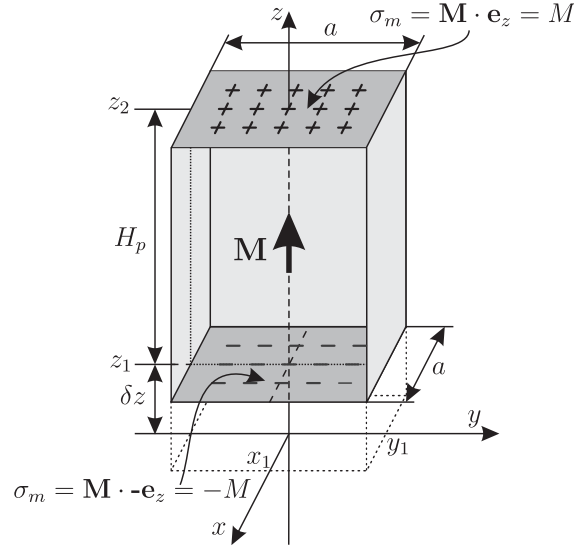
Figure 3.4: Analytic charge model of the cuboidal permanent magnet.

with $\mathbf{P}' = [x', y', z']^{\mathsf{T}}$ denoting the source point. For the cuboidal permanent magnet the integral in equation (3.10) is evaluated over the rectangular top and bottom face

$$
\mathbf{B}(\mathbf{P}) = \frac{\mu_0 M}{4\pi} \left[\left. \int_{-a/2}^{a/2} \int_{-a/2}^{a/2} \frac{(\mathbf{P} - \mathbf{P}')}{|\mathbf{P} - \mathbf{P}'|^3} dx' dy' \right|_{z=\delta z + h} \right.
$$
$$
\left. - \left. \int_{-a/2}^{a/2} \int_{-a/2}^{a/2} \frac{(\mathbf{P} - \mathbf{P}')}{|\mathbf{P} - \mathbf{P}'|^3} dx' dy' \right|_{z=\delta z} \right].
\tag{3.11}
$$

The magnetic flux density components B_x, B_y and B_z at the point $\mathbf{P} = [x, y, z]^{\mathsf{T}}$ are calculated as [33, 125]

$$
B_x(x, y, z) = \frac{\mu_0 M}{4\pi} \sum_{k=1}^{2} \sum_{m=1}^{2} (-1)^{k+m} \log \left[F(x, y, z, x_m, y_1, y_2, z_k) \right],
\tag{3.12}
$$

with

$$
F(x, y, z, x_m, y_1, y_2, z_k) = \frac{(y - y_1) + [(x - x_m)^2 + (y - y1)^2 + (z - z_k)^2]^{1/2}}{(y - y_2) + [(x - x_m)^2 + (y - y2)^2 + (z - z_k)^2]^{1/2}},
$$

$$
B_y(x, y, z) = \frac{\mu_0 M}{4\pi} \sum_{k=1}^{2} \sum_{m=1}^{2} (-1)^{k+m} \log \left[H(x, y, z, x_1, x_2, y_m, z_k) \right],
\tag{3.13}
$$

with

$$
H(x, y, z, x_1, x_2, y_m, z_k) = \frac{(x - x_1) + [(x - x_1)^2 + (y - y_m)^2 + (z - z_k)^2]^{1/2}}{(x - x_2) + [(x - x_2)^2 + (y - y_m)^2 + (z - z_k)^2]^{1/2}},
$$

and

$$B_z(x,y,z) = \frac{\mu_0 M}{4\pi} \sum_{k=1}^{2} \sum_{m=1}^{2} \sum_{n=1}^{2} (-1)^{k+m+n}$$
$$\cdot \tan^{-1} \left[\frac{(x-x_n)(y-y_m)}{z-z_k} G(x,y,z,x_n,y_m,z_k) \right], \quad (3.14)$$

with

$$G(x,y,z,x_n,y_m,z_k) = \frac{1}{[(x-x_n)^2 + (y-y_m)^2 + (z-z_k)^2]^{1/2}}.$$

The indices $n,m,k \in 1,2$ denote the edge coordinates of the charged planes (bottom and top face of the permanent magnet). Thus, it holds in equations (3.12)-(3.14) $x_1 = y_1 = a/2$, $x_2 = y_2 = -a/2$, $z_1 = \delta z$ and $z_2 = \delta z + h$.

Analytic Current Model of the Cylindrical Permanent Magnet   The existing surface current model is depicted in Figure 3.5(a). The model is represented by an equivalent infinite thin solenoid of radius R_p and height H_p [20]. Thus, the axially magnetized cylindrical permanent magnet is replaced by an equivalent surface current flowing in azimuthal direction on the lateral cylinder surface.

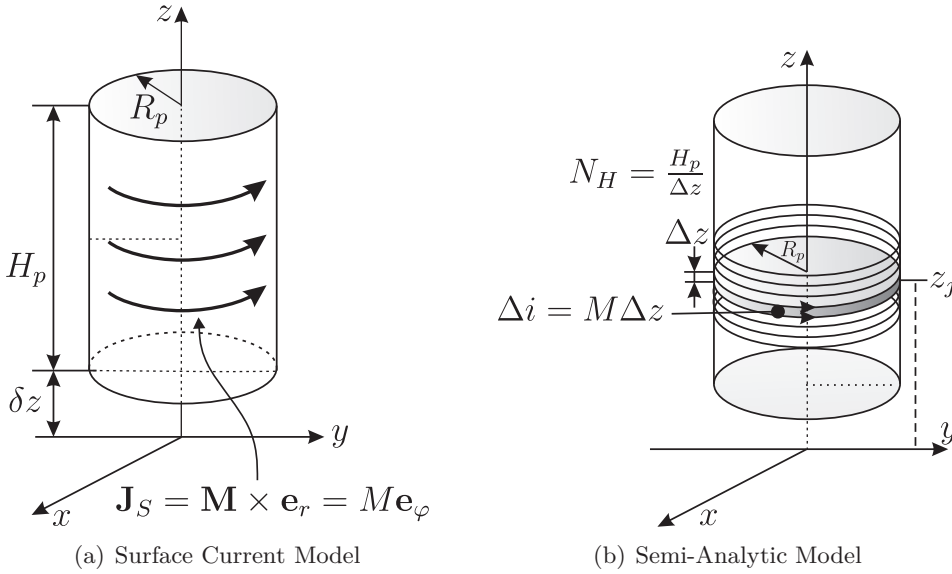(a) Surface Current Model   (b) Semi-Analytic Model

Figure 3.5: Models of cylindrical permanent magnet.

Evaluating the unit surface normals the equivalent surface current density is defined as $\mathbf{J}_S = \mathbf{M} \times \mathbf{n} = \mathbf{M} \times \mathbf{e}_r = \mathbf{M} \cdot \mathbf{e}_\phi$. Using cylindrical coordinates the magnetic flux density $\mathbf{B}(\mathbf{P})$ at the point $\mathbf{P} = [r,z]^\mathsf{T}$ is calculated as

$$\mathbf{B}(\mathbf{P}) = \frac{\mu_0}{4\pi} \oint_S \frac{\mathbf{J}_S(\mathbf{P})(\mathbf{P}-\mathbf{P}')}{\left|\mathbf{P}-\mathbf{P}'\right|^3} ds. \quad (3.15)$$

An analytic solution of the integral in equation (3.15) in terms of a generalized complete

elliptic integral is derived in [20]. With the assumption that the center of gravity of the solenoid is located at the origin of the coordinate system, the field components B_r in radial direction and B_z aligned with the coil axis at the point $\mathbf{P} = [r, z]^\mathsf{T}$ outside the magnet are calculated as

$$B_r(r, z) = \frac{\mu_0 M}{\pi} \left[\alpha_+ C\left(k_+, 1, 1, -1\right) - \alpha_- C\left(k_-, 1, 1, -1\right) \right] \tag{3.16}$$

and

$$B_z(r, z) = \frac{\mu_0 M}{\pi} \frac{R_p}{R_p + r} \left[\beta_+ C\left(k_+, \gamma^2, 1, \gamma\right) - \beta_- C\left(k_-, \gamma^2, 1, \gamma\right) \right], \tag{3.17}$$

with

$$k_\pm = \sqrt{\frac{z_\pm^2 + (R_p - r)^2}{z_\pm^2 + (R_p + r)^2}}, \ \ z_\pm = z \pm \frac{H_p}{2}, \ \ \gamma = \frac{R_p - r}{R_p + r},$$

$$\alpha_\pm = \frac{R_p}{\sqrt{z_\pm^2 + (R_p + r)^2}}, \ \ \beta_\pm = \frac{z_\pm}{\sqrt{z_\pm^2 + (R_p + r)^2}}.$$

The function $C(\cdot)$ denotes the generalized complete elliptic integral and is defined as

$$C(k_c, p, c, s) = \int\limits_0^{\pi/2} \frac{c \cos^2 \phi + s \sin^2 \phi}{(\cos^2 \phi + p \sin^2 \phi)\sqrt{\cos^2 \phi + k_c \sin^2 \phi}} d\phi. \tag{3.18}$$

Semi-Analytic Model of the Cylindrical Permanent Magnet Exploiting the equivalence between a cylindrical permanent magnet and a solenoid, the magnetic flux density of a semi-analytic model described in [20] is derived. The cylindrical permanent magnet is substituted with a set of N_h elementary circular current loops located at the lateral surface of the magnet (Fig. 3.5(b)) [20,91]. Each elementary current loop has the height $\Delta z = H_p/N_h$ and carries the current $\Delta i = M \Delta z$. The magnetic flux density at the point $\mathbf{P} = [r, z]^\mathsf{T}$ outside the permanent magnet is the linear superposition of the magnetic flux densities of the single current loops and is calculated as

$$\mathbf{B}(\mathbf{P}) = \sum_{j=1}^{N_h} \Delta \mathbf{B}^j\left(\mathbf{P}\right). \tag{3.19}$$

The magnetic flux density $\Delta \mathbf{B}^j\left(\mathbf{P}\right)$ produced by the j-th current loop at the position z_j is obtained by applying the Biot-Savart-Law integrated over the current loop. Using cylindrical coordinates the flux density components ΔB_r^j and ΔB_z^j are calculated as

$$\Delta B_r^j(r, z) = \mu_0 M \frac{\Delta z}{2\pi R_p} \frac{\gamma}{\sqrt{Q_j}} \left[E(k_j) \frac{1 + \alpha^2 + \beta_j^2}{Q_j - 4\alpha} - K(k_j) \right], \tag{3.20}$$

and

$$\Delta B_z^j(r, z) = \mu_0 M \frac{\Delta z}{2\pi R_p} \frac{1}{\sqrt{Q_j}} \left[E(k_j) \frac{1 - \alpha^2 + \beta_j^2}{Q_j - 4\alpha} + K(k_j) \right], \tag{3.21}$$

with

$$\alpha = \frac{p}{R_p}, \beta_j = \frac{z - z_j}{R_p}, \gamma_j = \frac{z - z_j}{p}, Q_j = (1 + \alpha)^2 + \beta_j^2, k_j = \sqrt{\frac{4\alpha}{Q_j}}, \tag{3.22}$$

and $p = \left| \mathbf{P} - \mathbf{P}' \right|$ denoting the distance from the center of the current loop $\mathbf{P}'$ to the field measurement point. Further, $E(k_j)$ and $K(k_j)$ are the complete elliptic integrals of the first and second kind, respectively. They are denoted by

$$K(k_j) = \int_0^{\pi/2} \frac{d\phi}{\sqrt{1 - k_j^2 \sin^2 \phi}}, \tag{3.23}$$

and

$$E(k_j) = \int_0^{\pi/2} \sqrt{1 - k_j^2 \sin^2 \phi} d\phi. \tag{3.24}$$

3.2.3 Optimization Procedure

The aim of the following optimization procedure is to determine optimal parameters α_o for the α-MDMs (equation 3.3) as well as optimal parameters α_o and β_o for the (α,β)-MDMs (equation (3.9)) with the given predefined numbers of dipoles. A test region $\mathbf{G}$ in the specimen is defined, which is positioned in the region below the permanent magnet (Figure 3.6). Motivated by the laminated structure of the specimen explained in Section 2.2, the test region consists of $N_z = 5$ XY-layers: $\mathbf{G} = \{\mathbf{G}_k, k = 1, \cdots, N_z\}$. The XY-layers are equidistantly distributed along the z-axis $\{z_k = -d_0 - (k - 1)\Delta z, \ k = 1, \ldots, N_z\}$, with $d_0 = -1\,\text{mm}$ indexing the z-coordinate of the uppermost layer and $\Delta z = 1\,\text{mm}$ the distance between adjacent layers. Considering the liftoff distance of the permanent magnet, the closest layer is located at a distance of $2\,\text{mm}$ below the permanent magnet. Due to the permanent magnets, the test region in the specimen is restricted to the first quadrant $(x \geqslant 0, y \geqslant 0)$. Each layer in the test region is composed of a regular grid of $N_x \times N_y = 31 \times 31$ points equidistantly distributed in the XY-plane. Thus, it holds $\mathbf{G}_k : \{x_i = (i - 1)\Delta x, y_j = (j - 1)\Delta y, i = 1, \cdots, N_x, j = 1, \cdots, N_y\}$, with $\Delta x = 1\,\text{mm}$ and $\Delta y = 1\,\text{mm}$ denoting the distance between the grid points.

In the test region the global normalized root mean square error NRMSE_G between the magnetic flux density obtained from the α- or (α,β)-MDMs and the flux density provided by the corresponding reference solution is evaluated. The reference solutions, which are explained in the Section 3.2.2, are the charge model for the cuboidal and the current model for the cylindrical permanent magnet.

The goal function to be minimized is defined as

$$\text{NRMSE}_\text{G} = \sqrt{\frac{1}{N_z} \sum_{k=1}^{N_z} \left[\text{NRMSE}_\text{G}^\text{k}(\cdot) \right]^2}. \tag{3.25}$$
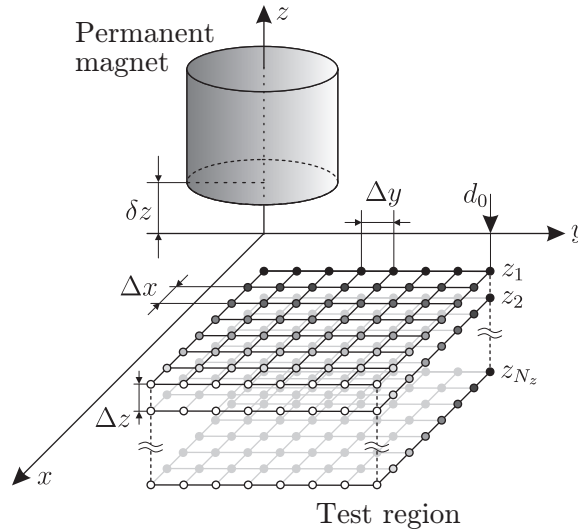
Figure 3.6: Test region in the optimization procedure to obtain optimal dipole positions in the MDM.

The $\mathrm{NRMSE_G}$ in the k-th XY-layer $\mathrm{NRMSE_G^k}(\cdot)$ is calculated in % as

$$\mathrm{NRMSE_G^k}(\cdot) = \frac{\sqrt{\dfrac{1}{N_x N_y} \sum\limits_{n=1}^{3} \sum\limits_{i=1}^{N_x} \sum\limits_{j=1}^{N_y} \left[B_n^D\left(x_i, y_j, z_k\right) - B_n^A\left(x_i, y_j, z_k\right)\right]^2}}{\max\left(\sqrt{\sum\limits_{n=1}^{3}\left(B_n^A\right)^2}\right) - \min\left(\sqrt{\sum\limits_{n=1}^{3}\left(B_n^A\right)^2}\right)\Bigg|_{z=z_k}} \cdot 100, \qquad (3.26)$$

with B_n^D being the n-th component of the magnetic flux density obtained from the α- or (α,β)-MDM, and B_n^A being the n-th component of the reference solution. Further, the index $n \in \{1, 2, 3\}$ corresponds to the $\{x, y, z\}$-components of $\mathbf{B}$.

In order to minimize equation (3.25) for the α-MDMs and (α,β)-MDMs the golden section search algorithm [87] and the simplex search method [78] are applied, respectively. The parameters are bounded to the interval $(\alpha, \beta) \in [0, 1]$. Further, the initial values for the simplex algorithm are set to $\alpha_0 = \beta_0 = 0.5$

3.2.4 Lorentz Force Evaluation using Magnetic Dipoles Model of Cuboidal Permanent Magnet

The aim is to investigate how the dipole optimization influences the error in the forward calculated Lorentz forces. Therefore, the α-MDMs with optimized positions of the cuboidal permanent magnet are embedded into the existing first approximation of the defect response signal (DRS) in LFE (Section 2.4.1). Moreover, the DRS is calculated using the α-MDMs with straightforward dipole positions, e.g., $\alpha = 0.5$. According to equation (3.1), force signals using the α-MDMs can be easily calculated as the sum of the force signals for the single dipoles.

Further, the DRS is computed using the charge model explained in Section 3.2.2. These

force signals serve as a reference solution for the data calculated with the α-MDMs with optimized and straightforward dipole positions. In contrast to the results of numerical simulations, this approach ensures that we only investigate signal errors of the α-MDMs and not the total error of the approximate forward solution.

The analysis is restricted to the cuboidal permanent magnet, because it is possible to find analytical expressions for the electric potential and eddy currents induced in the plate only for the magnet model in the form of a cuboid but not in the form of a cylinder. Using the analytic expression for the B_y-component of the magnetic flux density of the charge model in equation (3.13), the equation for the electric potential φ in an anisotropic defect-free conductor is derived to

$$
\begin{aligned}
\varphi &= \int_{-\infty}^{z} v \cdot B_y \, \partial z \\
&= \frac{v\mu_0 M}{4\pi} \left[\sum_{k=1}^{2} \sum_{m=1}^{2} (-1)^{k+m} \left[\sum_{n=1}^{2} (-1)^n \cdot \tilde{y}_m \cdot \tan^{-1}\left(\frac{\tilde{x}_n \cdot \tilde{z}_k}{\tilde{y}_m \cdot r_{kmn}}\right) \right] + \tilde{z}_k \cdot \ln \frac{\tilde{x}_1 \cdot r_{km1}}{\tilde{x}_2 \cdot r_{km2}} \right. \\
&\quad \left. + \tilde{x}_1 \cdot \ln\left(\frac{(\tilde{z}_1 + r_{111})(\tilde{z}_2 + r_{221})}{(\tilde{z}_1 + r_{121})(\tilde{z}_2 + r_{211})}\right) + \tilde{x}_2 \cdot \ln\left(\frac{(\tilde{z}_1 + r_{122})(\tilde{z}_2 + r_{212})}{(\tilde{z}_1 + r_{112})(\tilde{z}_2 + r_{212})}\right) \right), \quad (3.27)
\end{aligned}
$$

with $\tilde{x}_n = x - x_n$, $\tilde{y}_m = y - y_m$ and $\tilde{z}_k = z - z_k$. The distance between the evaluated field point and the edge of the permanent magnet is denoted by $r_{kmn} = \sqrt{\tilde{x}_n^2 + \tilde{y}_m^2 + \tilde{z}_k^2}$. The indices $n, m, k \in 1, 2$ correspond to the edge coordinates of the bottom and top face of the permanent magnet, i.e., the charged planes as shown in Figure 3.4.

Then, the components of the defect response eddy current distribution (DRCD) $\Delta \mathbf{j} = [\Delta j_x, \Delta j_y, 0]^\mathsf{T}$, which are responsible for the DRS, are calculated according to Ohm's law in equation (2.7) as $\Delta j_x = \partial\varphi/\partial x$ and $\Delta j_y = \partial\varphi/\partial y - vB_z$ with

$$
\begin{aligned}
\frac{\partial\varphi}{\partial x} &= \frac{v\mu_0 M}{4\pi} \left[\sum_{k=1}^{2} \sum_{m=1}^{2} \sum_{n=1}^{2} (-1)^{k+m+n} \cdot \left[\frac{-\tilde{y}_m^2 \cdot \tilde{z}_k}{\tilde{x}_n^2 + \tilde{y}_m^2} \cdot r_{kmn} + \frac{\tilde{z}_k + \tilde{x}_n^2}{r_{kmn}} \cdot (r_{kmn} + \tilde{z}_k) \right] \right] \\
&\quad + \ln\left(\frac{(\tilde{z}_1 + r_{111})(\tilde{z}_1 + r_{221})}{(\tilde{z}_2 + r_{121})(\tilde{z}_2 + r_{211})}\right) + \ln\left(\frac{(\tilde{z}_1 + r_{122})(\tilde{z}_1 + r_{212})}{(\tilde{z}_2 + r_{112})(\tilde{z}_2 + r_{222})}\right), \quad (3.28)
\end{aligned}
$$

$$
\begin{aligned}
\frac{\partial\varphi}{\partial y} &= \frac{v\mu_0 M}{4\pi} \sum_{k=1}^{2} \sum_{m=1}^{2} \sum_{n=1}^{2} (-1)^{k+m+n} \cdot \left[\frac{\tilde{x}_n \tilde{z}_k \left(\frac{1}{\tilde{y}_m \cdot r_{kmn}} + \frac{\tilde{y}_m}{r_{kmn}^{2/3}} \right)}{\frac{\tilde{x}_n^2 \tilde{z}_k^2}{\tilde{y}_m^2 r_{kmn}} + 1} - \tan^{-1}\left(\frac{\tilde{x}_n \tilde{z}_k}{\tilde{y}_m r_{kmn}}\right) \right. \\
&\quad \left. + \tan^{-1}\left(\frac{\tilde{z}_k}{\tilde{y}_m}\right) + \left(\frac{\tilde{y}_m \tilde{z}_k}{\tilde{x}_n + r_{kmn}} + \frac{\tilde{x}_n \tilde{y}_m}{r_{kmn}}\right) \cdot (r_{kmn} + \tilde{z}_k) \right], \quad (3.29)
\end{aligned}
$$

and B_z given in equation (3.14).

For forward calculations a benchmark problem for LFE with an anisotropic specimen containing a quadratic defect with the dimensions $6\,\text{mm} \times 6\,\text{mm} \times 2\,\text{mm}$ and depth $d = 2\,\text{mm}$ is applied (Figure 2.2). Similar to the permanent magnet, the center of gravity of the defect

is located at $x = y = 0$. Thus, the defect and the permanent magnet have the same symmetry lines. The Lorentz forces in the vicinity of the defect are examined. The observation points are equidistantly distributed in the range of $0 \leqslant x \leqslant 20 \, \text{mm}$, $0 \leqslant y \leqslant 10 \, \text{mm}$ at $z = 1 \, \text{mm}$. Due to the symmetry of the problem setup the investigated region is restricted to the first quadrant of the coordinate system. The distance between adjacent observation points in x- and y-direction equals $1 \, \text{mm}$. For comparison, the $\text{NRMSE}_{\Delta F}$ between the three-component Lorentz force perturbations obtained by the α-MDMs and the charge model is calculated.

3.2.5 Computational Resources

In practical application of the MDMs, special focus is on the computational complexity of the applied optimization procedure, i.e., of the optimization algorithm and the MDMs. Further, the computational cost required to compute the MDMs is of interest. These factors are evaluated, because they determine the efficiency of the optimization procedure.

In order to monitor the computational demand the optimizations are performed on a computer system equipped with an Intel® Xeon® E5472 processor (dual core CPU with 2x3 GHz), 12 MB of L2 cache and 64 GB of RAM. The operating system is a 64-bit Linux Gentoo Base System (release 2.2). Computations are performed using the software MATLAB® R2013b (release 8.2). In order to minimize the overall computation time multi-threaded computing is enabled. However, an even distribution of the work load on multiple CPUs is not ensured. The CPU time and additionally the number of function evaluations is measured, which is necessary for the optimization algorithms to converge. Both factors are expected to vary among MDMs with different numbers of dipoles.

Since the applied golden section search algorithm and the simplex method are deterministic optimization algorithms and the initial values are set, deviations in the optimization results for multiple trials are unlikely to be expected. Even more, differences in the CPU time among multiple trials, which can occur due to the background operating system activity, can be neglected. Thus, one trial for each preset MDM is performed.

3.3 Results

3.3.1 Magnetic Dipoles Models

α-**MDM of the Cuboidal Permanent Magnet** The results of the optimization of the α-MDM of the cuboidal permanent magnet are shown in Figure 3.7 using semi-logarithmic scaling. In the following, the MDMs with optimized dipole positions are denoted by α_o-MDM, whereas α-MDM remains a general denotation for the MDM of the cuboidal permanent magnet. The accuracy of the magnetic flux density obtained from the α_o-MDM is evaluated by assessing their NRMSE_G in groups with the group parameter N_a and the function argument N_h. Thus, an increase of the total number of magnetic dipoles N_D is caused by an increase of N_h (Figure 3.7(a)). The results show that for each group indexed

by N_a an optimal number of layers $N_{h,\min}^o = \{2, 5, 9, 13, 16, 20, 23\}$ with corresponding minimum errors $\mathrm{NRMSE}_{\mathrm{G,min}}^o = \{1.52, 0.32, 0.07, 0.017, 0.006, 0.003, 0.001\}\,\%$ exists. Further, an increase of N_a yields an increase of $N_{h,\min}^o$. Using the results of a least squares fit, the optimal number of layers depends on N_a as $N_{h,\min}^o = [1.79N_a - 1.71]$ with $[\cdot]$ denoting the nearest integer function. Further, with increasing N_a the edge-to-height ratio of the voxels converges to one. Thus, for high numbers of dipoles the optimal number of layers can be estimated by $N_{h,\min}^o = \lfloor \Delta h / \Delta a \rfloor$.
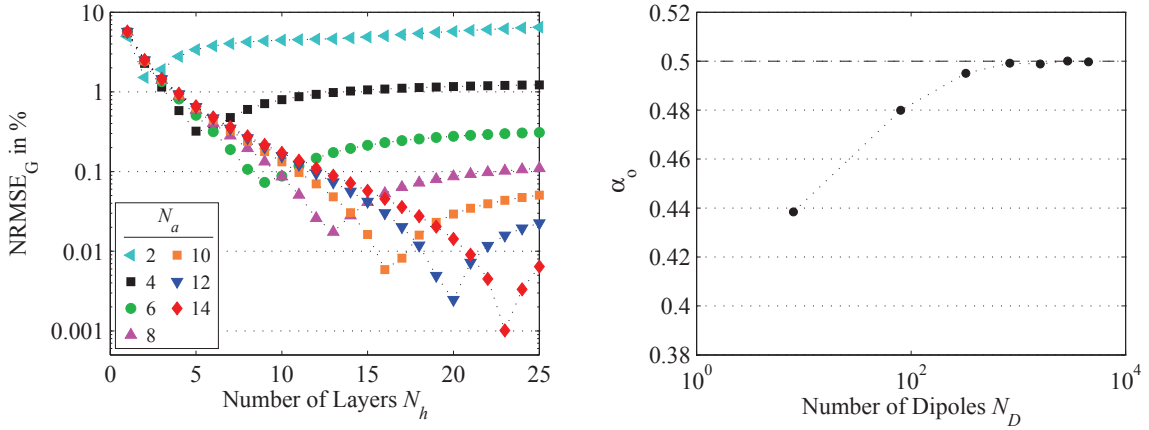
(a) $\mathrm{NRMSE}_{\mathrm{G}}$ between the α_o-MDMs and the charge model as a function of N_a and N_h in the α_o-MDM.

(b) Optimized parameter α_o depending on N_D of the α_o-MDMs corresponding to the minima in (a). The dashed line at $\alpha_o = 0.5$ indicates the center of gravity of the voxels.

Figure 3.7: Results of the optimization of the α-MDM of the cuboidal permanent magnet.

The optimized parameter α_o of the α_o-MDMs corresponding to the minimum error in each group is depicted in Figure 3.7(b) as a function of N_D. For small N_D the optimized position of the magnetic dipoles is lower than the standard choice, i.e., the center of gravity of the voxels indicated by the dashed line. With increasing number of magnetic dipoles α_o converges to 0.5.

Figure 3.8 compares the magnetic flux density components B_x and B_z of the MDMs with $N_D = 2^2 \cdot 2 = 8$ and $N_D = 8^2 \cdot 13 = 832$ dipoles and the charge model. The flux densities are evaluated in x-direction at $y = 0$ and $z = 1\,\mathrm{mm}$. This yields a total distance of $2\,\mathrm{mm}$ to the permanent magnet. Please note that due to the symmetry of the permanent magnet the B_y-component equals zero at $y = 0$. If the α_o-MDM consists of eight magnetic dipoles, the normalized root mean square error (NRMSE) of the B_x- and B_z-component equals $1.753\,\%$ and $1.651\,\%$, respectively. This α_o-MDM provides a good approximation of the magnetic flux density at far distances. However, remarkable discrepancies are observed in the region below the permanent magnet $(-7.5\,\mathrm{mm} \leqslant x \leqslant 7.5\,\mathrm{mm})$. In the region of the extremal values the magnitude of the B_x-component is smaller than the charge model. Moreover, the slopes are less steeper. Further, B_z drops to a local minimum. If the cuboidal permanent magnet is represented with 832 dipoles, the NRMSE of both components equals $0.027\,\%$. The irregularities observed in the α_o-MDM with eight dipoles vanish.
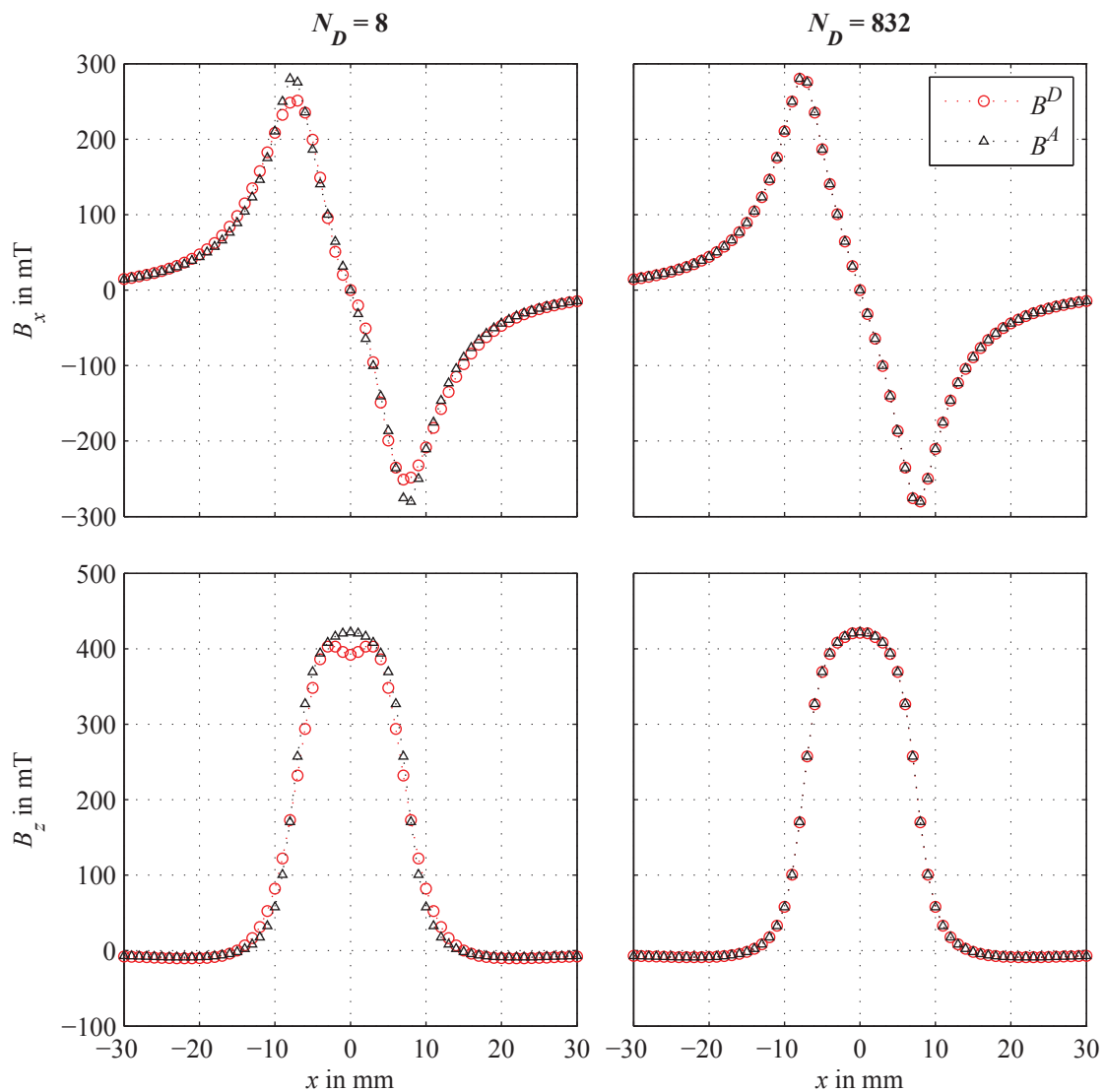
Figure 3.8: Comparison of magnetic flux densities obtained from two α_o-MDMs (B_D) and the charge model (B_A) of the cuboidal permanent magnet. The flux densities are calculated at the symmetry line of the permanent magnet ($y = 0$) and $z = 1\,\mathrm{mm}$. The α_o-MDMs are calculated for $N_D = 2^2 \cdot 2 = 8$ with $\alpha_o = 0.4384$ (left column) and $N_D = 8^2 \cdot 13 = 832$ with $\alpha_o = 0.4992$ (right column). The upper and lower row depict the magnetic flux density components B_x and B_z, respectively.

(α,β)-MDM of the Cylindrical Permanent Magnet Similar to the cuboidal permanent magnet, the $\mathrm{NRMSE_G}$ between the (α_o,β_o)-MDMs with optimized parameters and the analytic current model are depicted in groups using N_h as the group parameter and N_R as the function parameter (Figure 3.9(a)). A minimum for each N_R indicates the optimal number of dipole layers $N^o_{h,\mathrm{min}} = \{2,5,8,12,15,18,23\}$ for the (α_o,β_o)-MDMs. The corresponding errors equal $\mathrm{NRMSE^o_{G,min}} = \{2.19, 0.89, 0.36, 0.12, 0.05, 0.02, 0.01\}$ %.

Figure 3.9(b) shows the optimized parameters α_o and β_o for the (α_o,β_o)-MDMs corresponding to the minimum error in Figure 3.9(a) as a function of N_D. For intermediate N_D the MDMs tend to smaller z-coordinate (α_o), but slightly larger radial coordinate (β_o) compared to (α,β)=(0.5,0.5). With enlarging N_D the parameters converge to 0.5.
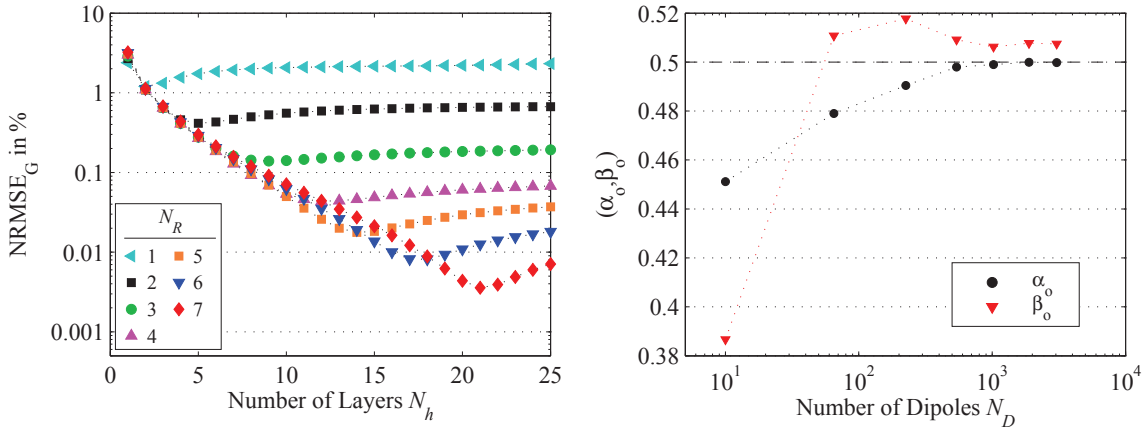
(a) $\mathrm{NRMSE_G}$ between the (α_o,β_o)-MDMs and the analytic current model as a function of N_R and N_h in the (α_o,β_o)-MDM

(b) Optimized Parameters α_o and β_o in dependence of N_D of the (α_o,β_o)-MDMs corresponding to the minima in (a). The dashed line at $\alpha_o = \beta_o = 0.5$ indicates straightforward positioning of the voxels.

Figure 3.9: Results of the optimization of the (α,β)-MDM of the cylindrical permanent magnet.

Instances of the magnetic flux densities obtained from two (α_o,β_o)-MDMs and the current model are compared in Figure 3.10. The flux densities are calculated at $y = 0\,\mathrm{mm}$ and $z = 1\,\mathrm{mm}$ yielding a total distance of $2\,\mathrm{mm}$ to the permanent magnet. If $N_D = 10$ ($N_R = 2, N^o_{h,\mathrm{min}} = 2$) holds, the NRMSE equals $2.78\,\%$ and $2.56\,\%$ for the B_x- and B_z-component, respectively. Similar to the cuboidal magnet, differences are observed in the region of $7.5\,\mathrm{mm} \leqslant x \leqslant 7.5\,\mathrm{mm}$. The B_x-component of the MDM is too small, whereas the B_z-component overshoots the current model. If the (α_o,β_o)-MDM consists of 1890 magnetic dipoles ($N_R = 6, N^o_{h,\mathrm{min}} = 18$), the NRMSE of the B_x- and B_z-component result into $0.034\,\%$ and $0.039\,\%$, respectively.
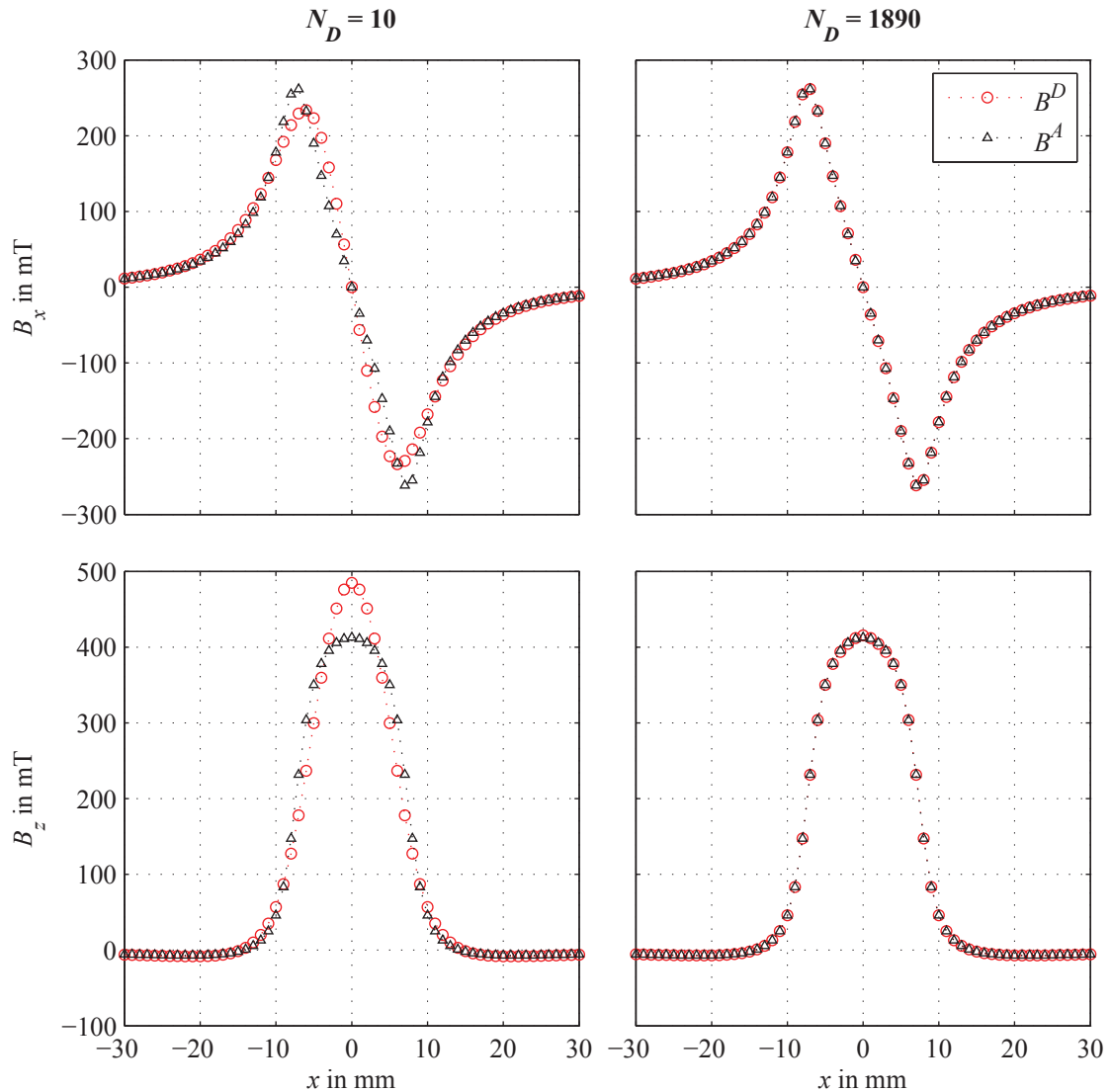
Figure 3.10: Comparison of magnetic flux densities obtained from two (α_o,β_o)-MDMs (B_D) and the current model (B_A) of the cylindrical permanent magnet. The flux densities are calculated at the symmetry line of the permanent magnet $(y=0\,\text{mm})$ and $z=-1\,\text{mm}$. The (α_o,β_o)-MDMs are calculated for $N_D=10$ with $\alpha_o=0.44$, $\beta_o=0.3892$ (left column) and $N_D=1890$ with $\alpha_o=0.4992$, $\beta_o=0.5078$ (right column). The upper and lower row depict the magnetic flux density components B_x and B_z, respectively.

3.3.2 Influence of the Optimization Procedure

In order to evaluate the efficiency of the optimization procedure the NRMSE_G of the optimized MDMs ($\alpha_o - \text{MDM}$) is compared to the NRMSE_G of the MDMs with the same dipole configurations but straightforward dipole positions (α_s-MDM). Straightforward dipole positions are indicated by $\alpha_s = 0.5$ as well as $(\alpha_s, \beta_s) = (0.5, 0.5)$ ((α_s, β_s)-MDM) for the cuboidal and cylindrical magnet, respectively. In case of the cuboidal magnet the straightforward dipole positions correspond to the center of gravity of the voxels. The comparison is made for both permanent magnets. The results are shown in Figure 3.11 using semi-logarithmic scaling. The improvement is similar for all MDMs. The optimized MDMs have approximately half the error than the MDMs with not optimized dipole positions.

(a) Cuboidal permanent magnet (b) Cylindrical permanent magnet
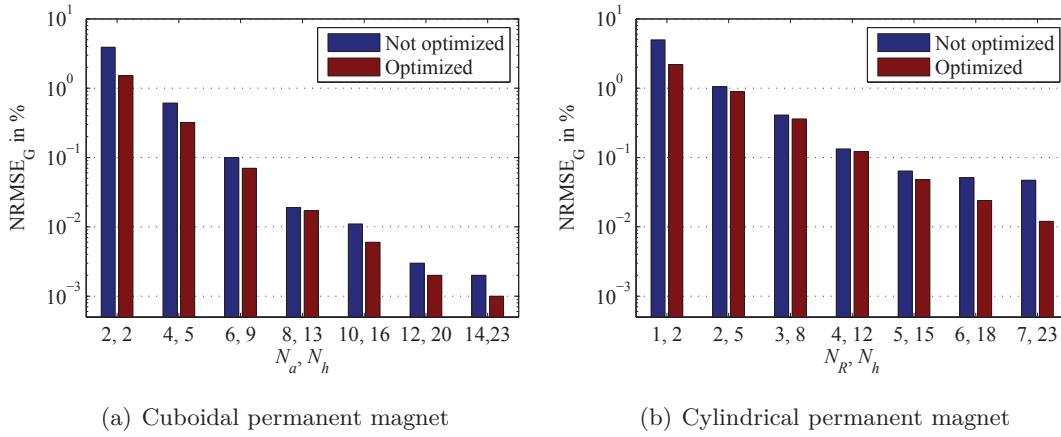
Figure 3.11: Comparison between MDMs with not optimized and optimized dipole positions ($\alpha_o - \text{MDM}$ and $\alpha_s - \text{MDM}$) using semi-logarithmic scaling. The MDMs have the same dipole configurations. The evaluated dipole configurations correspond to the minimum NRMSE_G among the groups in Figures 3.7(a) and 3.9(a).

3.3.3 Comparison of the Semi-Analytic and the Analytic Model of the Cylindrical Permanent Magnet

In order to evaluate the accuracy of the semi-analytic model for the cylindrical permanent magnet the magnetic flux density is compared to that of the analytic current model (Section 3.2.2). We vary the number of elementary current loops in a logarithmic scheme from 10 to 1000 and calculate the NRMSE. The results are depicted in Figure 3.12 using double-logarithmic scaling.

The NRMSE decreases exponentially with increasing number of current loops. If 10 current loops are considered, the NRMSE equals 2.18 %. It decreases to 0.021 % for $N_H = 100$ and $2.42 \cdot 10^{-4}$ % for $N_H = 1000$.
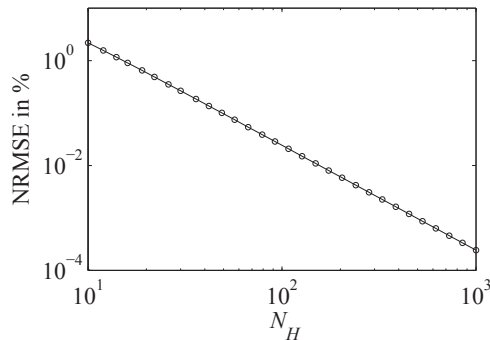
Figure 3.12: NRMSE between the semi-analytic and analytic current model of the cylindrical permanent magnet.

3.3.4 Lorentz Force Evaluation Using Magnetic Dipoles Model of Cuboidal Permanent Magnet

Figure 3.13 shows the $\mathrm{NRMSE}_{\Delta F}$ using semi-logarithmic scaling as a function of the total number of dipoles N_D in the α_o- and α_s-MDMs. As described in Section 3.2.4, the error is calculated between the DRS using MDMs of the cuboidal permanent magnet with optimized and straightforward dipole positions (α_o-MDMs and α_s-MDMs) and the DRS using the analytic charge model.
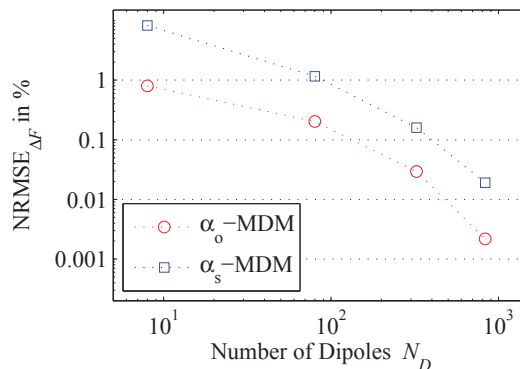
Figure 3.13: Comparison of forward computed Lorentz forces for the cuboidal permanent magnet. The force signals calculated with the α_o-MDM and the α_s-MDM are compared to force signals calculated with the charge model.

The perturbation in the force signals calculated with the α_o-MDM have a smaller error than the signals calculated with the α_s-MDMs. $\mathrm{NRMSE}_{\Delta F}$ errors introduced by α_o-MDMs equal 0.8 % and 0.002 % for $N_D = 8$ and $N_D = 832$, respectively. For the α_s-MDMs with the same number of magnetic dipoles, the error equals 8.2 % and 0.019 %, respectively. For large N_D the errors are similar.

A comparison of the errors of the magnetic flux density of the α_o-MDMs for the cuboidal permanent magnet (Figure 3.7(a), Section 3.3.1) shows that the errors in the force signals are smaller than the errors in the magnetic flux density. For $N_D = 8$ the errors in the force signals of the α_o-MDMs are smaller by half the value than the errors in the magnetic flux

density. For $N_D = 10$ the difference is approximately one decimal position. However, if the α_s-MDM are used the errors of the force signals are significantly higher for both $N_D = 8$ and for $N_D = 832$ than the NRMSE of the corresponding magnetic flux density.

A comparison of the DRS using the α_o-MDM and α_s-MDM with eight magnetic dipoles as well as the DRS using the charge model is shown in Figure 3.14. Forward calculations are performed using the first approximation of the forward solution for LFE. The force signals are depicted at $y = 2\,\mathrm{mm}$, since the ΔF_y-component vanishes at the symmetry line $(y = 0)$.
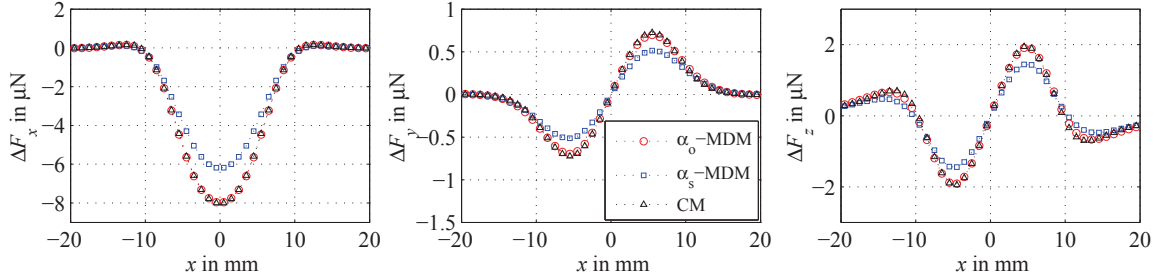
Figure 3.14: Comparison of DRS components ΔF_x, ΔF_y, and ΔF_z for the cuboidal permanent magnet. The signals are computed by applying the approximate forward solution including the α_o- and α_s-MDM with eight dipoles and the charge model (CM). The DRSs are depicted at the scanning line $y = 2\,\mathrm{mm}$.

In case of the α_o-MDM, the NRMSE of the ΔF_x-, ΔF_y- and ΔF_z-component equals $0.47\,\%$, $1.54\,\%$, and $1.68\,\%$, respectively. In case of the α_s-MDM, the NRMSE of the components equals $7.42\,\%$, $10.11\,\%$, and $6.88\,\%$.

3.3.5 Computational Resources

The worst case computational complexity of the golden section search algorithm used to optimize the α-MDM of the cuboidal permanent magnet equals $\mathcal{O}(\log n)$ [12], whereas the simplex method used for the (α, β)-MDM of the cylindrical permanent magnet has a complexity of $\mathcal{O}(2^n)$ [104]. Based on a source code evaluation is was observed that the MDM itself has a complexity of $\mathcal{O}(n)$. Thus, the optimization procedures for the cuboidal and cylindrical permanent magnet have complexities of $\mathcal{O}(n \cdot \log n)$ and $\mathcal{O}(n \cdot 2^n)$, respectively.

The measured CPU time and the number of function evaluations until convergence are shown in Figure 3.15. The evaluation is restricted to the MDMs that have the minimum NRMSE among the groups indicated by an equal N_a and varying N_h (Figures 3.7(a) and 3.9(a)).

The CPU time is depicted as a function of the number of magnetic dipoles N_D in Figure 3.15(a). It can be observed that the CPU time for all permanent magnets can be described by a linear function. This proves that the computational complexity of the MDMs is $\mathcal{O}(n)$. Optimizing the MDM of the cuboidal permanent magnet with $N_D = 8$ and $N_D = 832$ lasts with respect to the used computer system $2\,\mathrm{s}$ and $21\,\mathrm{s}$, respectively. The optimization of

(a) CPU time

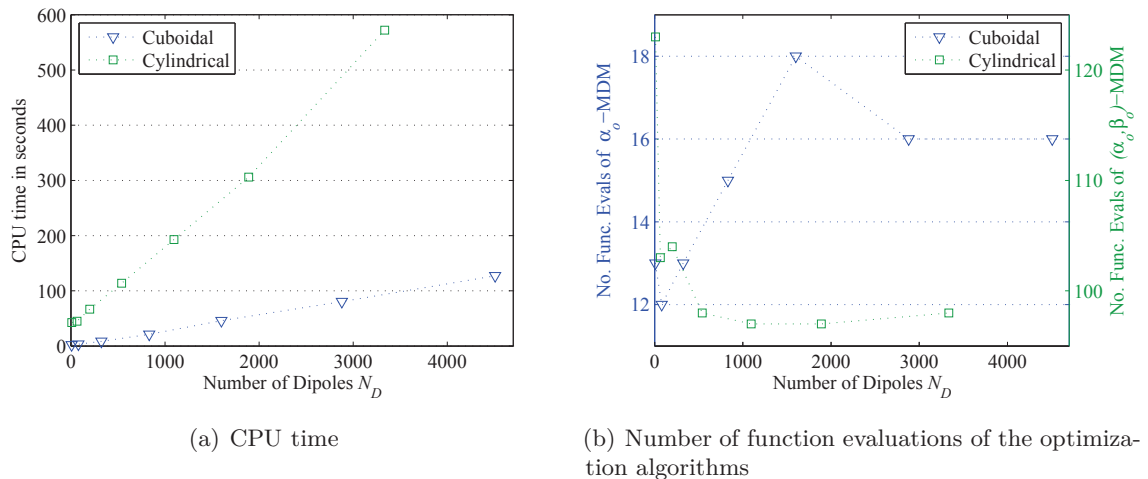(b) Number of function evaluations of the optimization algorithms

Figure 3.15: Computational resources required to optimize the MDMs of the cuboidal and cylindrical permanent magnet. The parameters are shown for MDMs having the optimal number of layers.

the (α, β)-MDM of the cylindrical magnet requires due to the two optimization variables in average over all evaluated MDMs ten times more CPU time than the α-MDM. For $N_D = 10$ and $N_D = 1890$ the CPU time equals $43 \, \mathrm{s}$ and $305 \, \mathrm{s}$, respectively.

The number of function evaluations are shown in Figure 3.15(b). Optimization of the (α, β)-MDM requires in average eight times more function evaluations than optimization of the α-MDM. The number of function evaluations of the golden section search algorithm applied to optimize the α_o-MDM is slightly larger for high numbers of dipoles. Contrary, the (α, β)-MDM executes more function evaluations for a low number of dipoles.

3.4 Discussion

In this chapter newly developed and existing models for the permanent magnets in Lorentz force evaluation (LFE) were evaluated. This study was motivated by the necessity to provide an accurate model of the permanent magnet for the forward solution of LFE, which is the basis for successful inverse calculations of defect parameters. The main contribution is the introduction of the magnetic dipoles model (MDM), which can be applied to arbitrary shaped permanent magnets with a homogeneous magnetization. In the MDM, the permanent magnet is represented with an assembly of magnetic dipoles. The model can be embedded into an analytic forward solution for LFE and the advantage to calculate the flux density and the eddy currents induced in the conductor with elementary analytic mathematics is maintained. In order to obtain optimal positions of the magnetic dipoles an optimization procedure was proposed, that is based on a comparison to existing analytic models.

The results in Figures 3.7(a) and 3.9(a), Section 3.3.1 show that 832 dipoles are necessary for the cuboidal permanent magnet, and 1890 dipoles for the cylindrical permanent magnet

to minimize the normalized root mean square error (NRMSE) to $0.02\,\%$ in the near field of the permanent magnet. Thus, for complex shaped magnets more dipoles have to be considered to achieve a similar accuracy. The higher number of dipoles compensates the fact that the dipole approximation is less accurate for cylindrical and hollow cylinder segments than for cuboidal voxels [83].

The comparison of the magnetic flux density (Section 3.3.1) and the forward calculated Lorentz forces (Section 3.3.4) obtained from the α_o-MDM and α_s-MDM shows, that the use of optimized dipole positions yields a significant improvement for MDMs with a small number of dipoles. With increasing number of dipoles the influence of the optimization is reduced. Thus, an optimized MDM requires less dipole layers to achieve the same NRMSE than the MDM with straightforward dipole positions, if the number of dipoles is small. This is especially valid for inverse calculations, since the computational costs can be reduced by using optimized instead of a larger number of dipoles, whereas both approaches yield a reduction of the modeling error. The use of the optimization procedure reduces the number of magnetic dipoles that are necessary to achieve a certain accuracy. The optimization is performed only once before any forward and inverse calculation and thus the computational demand is comparatively low.

Further, the comparison of the error differences of the magnetic flux density and the Lorentz force signals (Figures 3.7(a) and 3.13) show that for the α_o-MDMs the error in the magnetic flux density is partly compensated by the analytic forward calculations. However, this is not the case for the α_s-MDMs. For $N_D = 8$ a large error in the amplitude of the Lorentz forces can be observed. This is likely to be explained by the large differences in the α-parameter ($\alpha_o = 0.41$) determining a difference of $0.8\,\mathrm{mm}$ in the z-position of the dipoles for the used permanent magnet. This aspect strongly supports the use of the α_o-MDMs.

Apart from the cuboidal and cylindrical permanent magnet, a cubic permanent magnet with the dimensions $a = H_p = 15\,\mathrm{mm}$ was investigated. The same α-MDM-configurations as for the cuboidal magnet were optimized. The results detailed in Appendix A show that for $N_a = \{2, 4, 6\}$ the optimal number of layers equals $N_{h,min}^o = N_a - 1$, whereas for larger N_a it equals N_a. Compared with the cuboidal permanent magnet the minimum NRMSE for each group indexed by N_a are similar, but the optimal number of layers is smaller for the cubic permanent magnet. This is reasoned by the smaller height of the cubic permanent magnet.

Evaluating the results, an approximate linear dependence between the number of dipoles in one layer and the optimal number of layers for the α_o- and α_s-MDM of the cubic and cuboidal and the (α_s, β_s)-MDM of the cylindrical magnet was observed. No similar relationship could be found for the (α_o, β_o)-MDM. These results can be explained by the structure of the MDMs. In our study the dipole distributions in the MDMs are symmetric. Since the definition of the MDMs implies that the dipoles for MDMs with varying number of dipoles are positioned using the same principle, the symmetry lines are equal for all evaluated MDMs. Further, the dipoles represent an equal volume of the permanent magnet and have the same moment. Merely the (α_o, β_o)-MDM depends on two parameters. These

show a greater and non-monotonous variation in its values than the one parameter of the cubic and cuboidal permanent magnet (Figures A.1(b), 3.7(b) and 3.9(b)). Apart from symmetric dipole distributions non-symmetric distributions can be applied. The author in [108] presents a variety of non-symmetric distributions for the dipoles in the layers with the required weighting coefficients, which are different for the individual dipole moments.

In Figure 3.8 the B_z-component of the magnetic flux density of the α_o-MDM of the cuboidal magnet with $N_D = 8$ shows a drop at $x = 0$. In Figure 3.10 the B_z-component of the MDM of the cylindrical magnet shows a higher maximum than the reference solution for a low number of dipoles. Further, the extremal values of the B_x-components of both magnets are closer to the origin of the coordinate system and the slopes are steeper. These effects can be attributed to the close distance of the respective dipoles in the lower plane of the MDMs and the test region (near field of the dipoles). In the near field the inter-dipole distances have a stronger influence on the resulting magnetic flux density, if a small number of dipoles is considered. In the (α_o, β_o)-MDM with $N_D = 10$ the distance between the ring dipoles and the central dipole is reduced, because the parameter β_o is smaller than 0.5 (Figures 3.2 and 3.9(b)). Since the dipoles in the α_o-MDMs are fixed to the center of gravity of the bottom and top face, the dipoles in the (α_o, β_o)-MDM are closer to the symmetry axis ($y = 0\,\text{mm}$), at which the magnetic flux density is evaluated. A further comparison shows that the drop in the B_z-component for a small numbers of dipoles is smaller for the cubic than for the cylindrical permanent magnet (A.2). This can be explained by the number of layers in the respective MDMs. The cubic magnet is represented with one layer of dipoles, whereas the cuboidal magnet consists of 2 layers. Thus, the large drop yields from the superposition of the drops of the single dipole layers.

The results of the comparison between the semi-analytic and current model of the cylindrical magnet in Section 3.3.3 depict that 100 current loops are necessary to achieve a NRMSE of 0.02 %. The main advantage of the semi-analytic model is the mathematically less complicate derivation. It is recommended to use the semi-analytic model especially for educational purposes, since it may provide a better physical insight into the approach of modeling a cylindrical magnet with a wire-wound solenoid.

Figure 3.15(a) in Section 3.3.5 shows a linear dependence between the complexity of the MDMs (number of dipoles) and the CPU time required for the optimization procedure. Thus, the actual complexities of the optimization procedures are their best-case complexities ($\mathcal{O}(n)$). This is reasonable, since the number, the boundaries and the initial values of the optimization variables remain constant. Further, the number of function evaluations for the cylindrical magnet is significantly higher than for the cuboidal magnet. This can be explained by the fact that the MDM of the cylindrical magnet consists of two optimization variables. Moreover, with increasing numbers of dipoles the number of function evaluations of the golden section search method increases. This shows that for high numbers of dipoles the goal function is more flat in the region around the extracted minimum. Contrary, in case of the (α_o, β_o)-MDM the necessary function evaluations decrease. This results from the fact that for a high number of dipoles the initial values of the simplex method are close to the optimal values (Figure 3.9(b)).

In summary, the proposed MDM allows an efficient and accurate modeling of the permanent magnet in the forward solution for LFE.

4 Lorentz Force Evaluation using Differential Evolution

4.1 Introduction

Motivated by the advantages of stochastic optimization algorithms outlined in Section 2.5.2, an inverse calculation strategy for Lorentz force evaluation (LFE) based on the Differential Evolution (DE), an evolutionary strategy (ES), is introduced. The DE employs for mutation differences in the population member itself instead of probability density functions as in typical ES. Since its introduction in [107], the DE has become increasingly popular in a wide variety of applications. These include the system design in engineering and the determination of earthquake hypocenters in geophysics [88]. Recently, the DE has been applied for fluorescence lifetime imaging microscopy in ophthalmology [53]. Within these fields of application the DE has been used in different problem domains such as functions with equality and inequality constraints, quantized functions, multiobjective optimization, and combinatorial problems [88].

The DE has three intrinsic control parameters that determine the evolution process. In the first step parameter studies are performed to evaluate the dependence of the reconstruction results on these control parameters. Additionally, the voxel size in the reconstruction grid is assessed, because this factor is likely to have an impact on the resolution of LFE. For these purposes numerically simulated data is employed. Based on the results optimal optimization settings are selected. Then, the inverse strategy is applied to reconstruct defects in simulated and measured Lorentz force data obtained from laminated composites.

In the remaining chapter, the methods are explained in Section 4.2. This includes the DE algorithm, the proposed inverse scheme, the assessed data sets, and an outline on the performed evaluation. Then in Section 4.3, the results of the parameter studies followed by the reconstruction findings are presented. Finally, the results are discussed in Section 4.4. This chapter contains methods and results that have been accepted for publication in [71].

4.2 Material and Methods

4.2.1 Differential Evolution

The basic DE algorithm described in [107] is applied. A flow chart illustrating the main stages is shown in Figure 4.1. The DE starts with a randomly initiated population of N_p N_S-dimensional individuals $\boldsymbol{x}_n \in \mathbb{R}^{N_S \times 1}$. The elements of the individuals $x_{n,k}$ are the
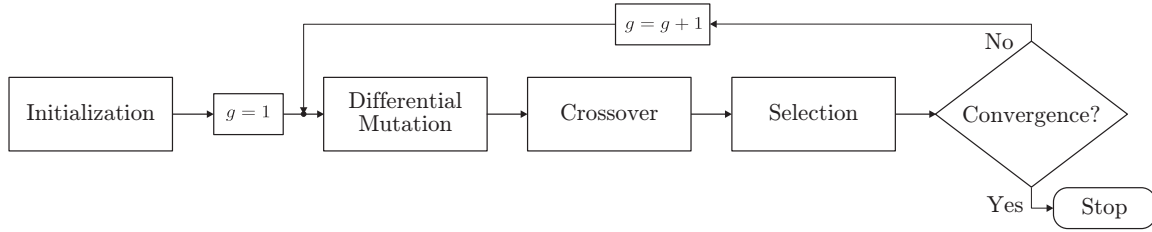
Figure 4.1: Flow chart of the Differential Evolution (DE). The variable g denotes the current generation.

conductivities bounded by the interval $[0, \sigma_0]$. Each of the N_p individuals provides a possible solution to the LFE optimization problem.

The population evolves by differential mutation, crossover, and selection. Mutation describes the change (perturbation) in successive populations using random elements. For each population member $\boldsymbol{x}$ in the target generation, a corresponding mutant $\boldsymbol{x}^{(\mathrm{m})}$ is calculated using three population members, $\boldsymbol{x}^{(1)}$, $\boldsymbol{x}^{(2)}$, and $\boldsymbol{x}^{(3)}$, as

$$\boldsymbol{x}^{(\mathrm{m})} = \boldsymbol{x}^{(1)} + F \cdot \left(\boldsymbol{x}^{(2)} - \boldsymbol{x}^{(3)} \right), \tag{4.1}$$

where F is the mutation scaling factor. The indices (1), (2), and (3) denote mutually exclusive members, which also differ from the target, and they are selected randomly from the population. For the sake of simplicity, please note that the index $n = 1, \ldots, N_p$ is not used in the notations for the individuals. Due to the use of the scaled difference of two individuals, the DE differs from other evolutionary strategies that employ predefined probability density functions during mutation [18].

During the crossover operation, the target and mutant exchange elements to form the trial vector $\boldsymbol{x}^{(\mathrm{t})}$. The elements of the trial vector $x_k^{(\mathrm{t})}$ are determined by using the crossover rate $C_r \in [0, 1]$ as

$$x_k^{(\mathrm{t})} = \begin{cases} x_k^{(\mathrm{m})} & \text{if } r_k \leqslant C_r \vee k = k_r \\ x_k & \text{otherwise} \end{cases}, \tag{4.2}$$

where $r_k \in [0, 1]$ and $k_r \in [1, N_S] \cap \mathbb{Z}$ are randomly generated numbers. Hence, the intrinsic control parameters of the DE are N_p, F, and C_r.

The individuals in the next generation $\tilde{\boldsymbol{x}}$ are selected by a one-to-one competition between the target and its corresponding trial vector

$$\tilde{\boldsymbol{x}} = \begin{cases} \boldsymbol{x}^{(\mathrm{t})} & \text{if } f(\boldsymbol{x}^{(\mathrm{t,b})}) \leqslant f(\boldsymbol{x}^{(\mathrm{b})}) \\ \boldsymbol{x} & \text{otherwise} \end{cases}, \tag{4.3}$$

where $f(\cdot)$ denotes the goal function. The superscript (b) denotes a binary vector, which is calculated prior to selection by binarizing the continuous parameters into the couple $\{0, \sigma_0\}$. The elements of $\boldsymbol{x}^{(\mathrm{b})}$ are obtained with respect to the threshold ϑ as

$$x_k^{(b)} = \begin{cases} 0 & \text{if } x_k \leqslant \vartheta \cdot \sigma_0 \\ \sigma_0 & \text{otherwise} \end{cases}. \tag{4.4}$$

The optimal value of ϑ is determined heuristically based on parameter studies in a later section of this study (Section 4.3.1).

Thresholding is motivated by the conductivity distribution used in the forward solution of LFE where only two conductivity values occur, i.e., $\sigma = \sigma_0$ or $\sigma = 0$ for the defect or non-defect regions, respectively (Section 2.4.1). Binary conductivity distributions are only used during the selection process. In DE, the individuals remain continuous during evolution. The binarization of population members for the selection operation accelerates the convergence of DE because the number of possible solutions is reduced and the DE is less likely to be trapped by local minima. Finally, the optimization is terminated if the goal function value of the overall best solution does not change within 500 iterations.

4.2.2 Inverse Calculation Strategy

The aim of the inverse calculation scheme is to reconstruct the conductivity distribution in the laminated specimen. The first approximation of the defect response signal (DRS) as outlined in Section 2.4.1 is applied for forward calculations. Since the defect is represented with a fictitious conducting region, regions with high conductivity in the inverse solution are interpreted as defect regions.

The applied defect reconstruction strategy consists of four steps (Figure 4.2). First, a one-layered regular grid of voxels with unknown conductivities, i.e., a source space, is defined for each of the N_L metal layers of the composite, where the defect is assumed to be located in. Voxels are defined with sizes of $\Delta x \times \Delta y \times \Delta z$ and they are distributed equally in quadratic source spaces, which are positioned in the $xy-$planes of the metal layers and have the dimensions $-l_s \leqslant (x, y) \leqslant l_s$. The depth of the source spaces and the height of the voxels are equal to the depth and thickness of the metal sheets, respectively. The number of voxels N_S in the source space is defined as $N_S = \lfloor 2l_s/\Delta x \rfloor \lfloor 2l_s/\Delta y \rfloor$. The unknown conductivity distribution for each metal sheet is summarized in a vector $\boldsymbol{\sigma} = [\sigma_1, \sigma_2, \cdots, \sigma_{N_S}]$.

Using the DRS profile $\Delta \mathbf{F} = [\Delta F_x^1, \Delta F_y^1, \Delta F_z^1, \ldots, \Delta F_x^M, \Delta F_y^M, \Delta F_z^M]^\mathsf{T}$ measured at M points, i.e., $\Delta \mathbf{F} \in \mathbb{R}^{3M \times 1}$, (2.9) can be reformulated into the following linear system of equations

$$\Delta \mathbf{F} = \boldsymbol{K}\boldsymbol{\sigma}, \tag{4.5}$$

where $\boldsymbol{K} \in \mathbb{R}^{3M \times N_S}$ is the gain matrix between the N_S unknown conductivities of voxels from the source space and the DRS at M measurement points.

The goal function $f(\boldsymbol{\sigma})$ that needs to be minimized in the LFE is assigned to the normalized root mean square error (NRMSE) between the forward calculated Lorentz force profiles $\Delta \mathbf{F}^{(A)}$ and the observed $\Delta \mathbf{F}^{(obs)}$, which has already been defined in equation (2.13),
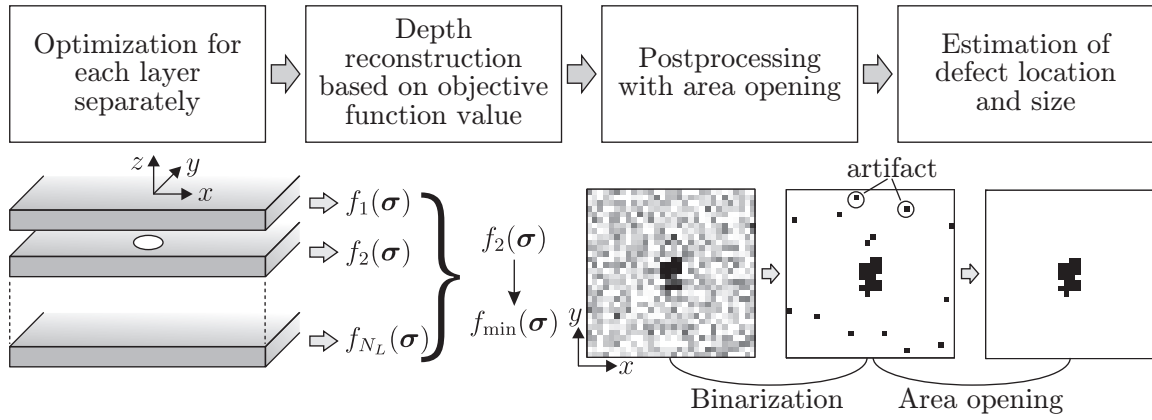
Figure 4.2: Inverse calculation strategy applied in LFE. Top: processing pipeline, bottom: illustration of the evaluation steps. Due to the conductivity substitutions in the forward solution for LFE, the voxels with $\sigma = \sigma_0$ (black) represent the defect region (see Section 2.4.1).

$$f(\boldsymbol{\sigma}) = \text{NRMSE}(\boldsymbol{\sigma}) = \frac{\sqrt{\frac{1}{3M} \sum\limits_{i=1}^{3} \sum\limits_{m=1}^{M} \left(\Delta F_{i,m}^{(A)}(\boldsymbol{\sigma}) - \Delta F_{i,m}^{(\text{obs})}(\boldsymbol{\sigma}) \right)^2}}{\max\limits_{m=1...3M} \left(\Delta \mathbf{F}_m^{(\text{obs})}(\boldsymbol{\sigma}) \right) - \min\limits_{m=1...3M} \left(\Delta \mathbf{F}_m^{(\text{obs})}(\boldsymbol{\sigma}) \right)}. \tag{4.6}$$

In this study, $\Delta \mathbf{F}^{(A)}$ profiles are calculated by the first approximation of the analytic forward procedure described in Section 2.4.1, whereas $\Delta \mathbf{F}^{(\text{obs})}$ profiles are either simulated numerically or measured.

Next, N_L successive optimizations are performed using DE, i.e., one separate optimization for each metal sheet. The conductivity distributions $\boldsymbol{\sigma}$ obtained after finishing the N_L optimizations are binarized distributions, as calculated in the last selection step of the corresponding optimization. The unknown defect depth d is assigned to the depth of the layer for which the minimum goal function value $f_{\min}(\boldsymbol{\sigma})$ is found.

Figure 4.2 shows that the binarized reconstructed conductivity distributions are not likely to comprise only one connected region of voxels that represent the defect, but instead isolated voxels with $\sigma = \sigma_0$ may be spread throughout the source space. In most cases, the isolated voxels can be treated as artifacts, i.e., non-physical solutions. In order to reduce these artifacts in the DE solution, the area opening approach is applied. This filter operation is derived from image processing, where it is applied to remove connected pixel concentrations from binary images with areas smaller than a predefined parameter [24]. Similar to the binarization of continuous-valued individuals, artifacts removal improves the convergence speed of the DE solution.

Finally, the location of the defect center is estimated as the mean of the x- and y-coordinates of the centers of gravity of the remaining voxels, i.e., the voxels that remain after removing the artifacts. The location error is calculated as the Euclidean distance between the estimated and the real position of the defect center. The size of the reconstructed defect is set to the total area of the top walls of the voxels representing the defect.

4.2.3 Investigated Data Sets

The proposed inverse calculation scheme is assessed based on two sets of numerically simulated data for an LFE problem setup and one data set of measured force signals. Simulated data are obtained using a finite element model (FEM) of the laminated specimen moving under the permanent magnet. The conductor comprised 50 aluminum sheets and the electrical conductivity of the specimen is assumed to be anisotropic, i.e., $\sigma_{zz} = 0$. In the first and second simulated data sets, a cylindrically shaped defect is positioned at the second and third aluminum sheet, respectively. A spherical permanent magnet is applied. The detailed parameter values for the conductor, defect, and permanent magnet are given in Table 4.1.

Table 4.1: Parameters of the LFE setup for simulated and measured force signals.

	Simulated Data (LFE benchmark problem)	Measured Data (Alucobond composite)
Conductor		
Dimension $L \times W \times H$ in mm × mm × mm	$400 \times 400 \times 100$	$250 \times 50 \times 4$
Thickness of metal sheets in mm	2	0.5
Conductivity of metal sheets σ_0 in MS/m	30.61	30.1
Velocity v in m/s²	0.01	0.5
Defect		
Shape	Cylinder	Cylinder
Radius R_d in mm	2.5	2.5
Height H_d in mm	2	0.5
Depth d in mm	$\{2, 4\}$	3.5
Permanent Magnet		
Shape	Sphere	Cylinder
Radius R_p in mm	7.5	7.5
Height H_p in mm	-	25
Remanence in T	1.17	1.17
Liftoff δz in mm	1	1

The simulated force signal profiles are computed along $x-$scan lines at discrete points of density $1\,\text{mm}$ in the range of $-l_x \leqslant x \leqslant l_x$ with $l_x = 25\,\text{mm}$. These scanning lines are uniformly distributed in the y-direction between $-l_y \leqslant y \leqslant l_y$ with $l_y = 15\,\text{mm}$. The scanning lines have a distance of $1\,\text{mm}$. The area in which the measurement points are distributed is called the source space.

The measured Lorentz force profiles are obtained using a three-layered composite called Alucobond. The Alucobond specimen shown in Figure 4.3 comprised two cover sheets made

of aluminum alloy with a thickness of 0.5 mm. The interface layer with a thickness of 3 mm is made of an electrically isolating polyethylene ($\sigma = 0$). The bottom cover sheet contains
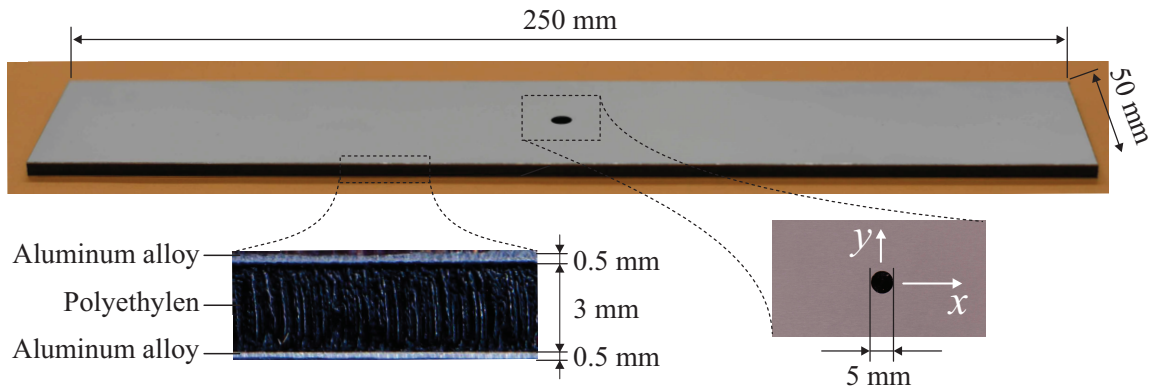

Figure 4.3: Three-layered Alucobond composite specimen used in the experimental setup: bottom view (top), side view (left), and view of the artificial defect in the lower cover sheet (right).

an artificial cylindrical hole at the center of the specimen. As in the experimental setup described by [9], the test specimen moves under the fixed cylindrical permanent magnet. The detailed parameter values for the experimental setup are summarized in Table 4.1.

The force signal profiles are recorded with 25 repetitions for 21 uniformly distributed $y-$positions of the permanent magnet ($-10\,\mathrm{mm} \leqslant y \leqslant 10\,\mathrm{mm}$) along the $x-$scan lines in the range of $-30\,\mathrm{mm} \leqslant x \leqslant 30\,\mathrm{mm}$, where x is relative to the center of the defect. The sampling frequency of the force signals is equal to $f_s = 10\,\mathrm{kHz}$.

The recorded force data are preprocessed by averaging ensembles of 25 repetitions for each $x-$scan line. Then, the preprocessing procedure shown in Figure 4.4 is applied. First, a Butterworth low-pass filter with a cut-off frequency of less than $100\,\mathrm{Hz}$ is applied to suppress the eigenfrequencies of the force sensor and high-frequency noise. The exact value depends on the frequency of the defect perturbations, i.e., the used permanent magnet and specimen containing a defect in the measurement setup. To determine the cutoff frequency, it is ascertain, based on spectral estimates of data obtained from numerical simulations, that the frequency of the defect perturbations is lower. Second, the DRS is calculated by subtracting the average force measured at points in the region that was not affected by the defect perturbations. This values represents the force coming from a defect-free specimen. Then, linear drifts are eliminated by subtracting a best fit line calculated from the same points outside the defect region. In order to reduce the complexity the data is downsampled to $f_s = 500\,\mathrm{Hz}$.
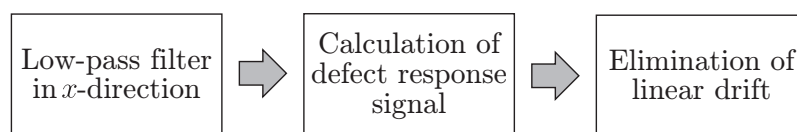

Figure 4.4: Preprocessing procedure for measured Lorentz force signals.

Figure 4.5 shows the defect response profiles $\Delta \boldsymbol{F} = [\Delta F_x, \Delta F_y, \Delta F_z]^{\mathsf{T}}$ caused by the defect in the vicinity of $x = 0$. Residual disturbances resulting from parameter deviations and inaccuracies that occurred during measurements can be seen outside the defect region.
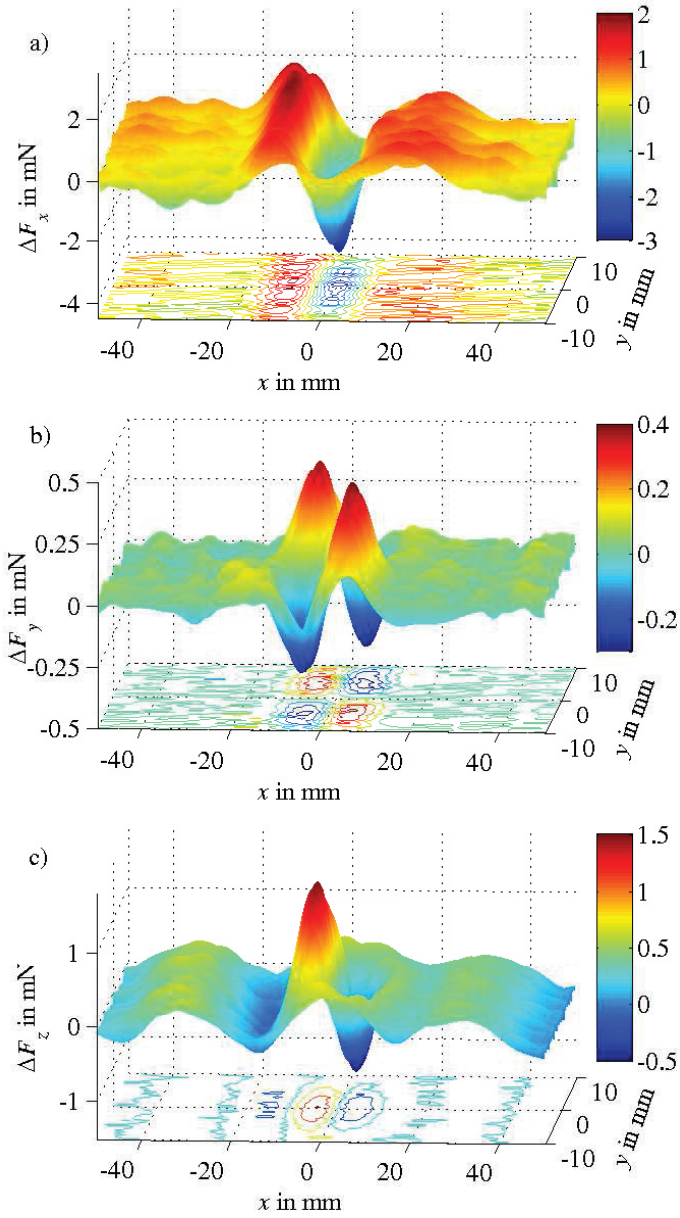

Figure 4.5: Profiles of the DRSs $\Delta \mathbf{F} = [\Delta F_x, \Delta F_y, \Delta F_z]^{\mathsf{T}}$ (top to bottom) obtained from preprocessed measured data for the Alucobond composite with a defect at the bottom cover sheet.

4.2.4 Evaluation Setup

In the first step of the evaluation, parameter studies are performed to determine the optimal values for the intrinsic DE control parameters, i.e., N_p, F, and C_r, for the threshold ϑ, as well as for the voxel extensions $\Delta x = \Delta y$. The choice of the intrinsic control parameters is especially important because they significantly affect the search for a global optimum and the speed of convergence [18]. The first set of simulated data is used and it is assumed that the defect depth is determined correctly as $d = 2$ mm. In all of these studies, the source space is quadratic and has the parameters $l_s = 15$ mm, $d = 2$ mm, $\Delta x = \Delta y = 1$ mm, and $\Delta z = 2$ mm is applied. The spherical permanent magnet is represented with one equivalent magnetic dipole positioned at the center of gravity of the permanent magnet, i.e., at $z = 8.5$ mm. The reconstruction scheme is applied to all combinations of $N_p = \{20, 40, 60\}$, $F = \{0, 0.1, \ldots, 1\}$, $C_r = \{0, 0.1, \ldots, 1\}$, $\vartheta = \{0.1, 0.2, \ldots, 0.9\}$, and $\Delta x = \Delta y = \{0.25, 0.5, \ldots, 2\}$ mm.

In the next step, defects are reconstructed for both the simulated and measured data using DE with the determined optimal parameter settings. For the simulated data, five source spaces positioned at depths of $d = \{0, 2, 4, 6, 8\}$ mm are used. For the measured data, two source spaces at the depths of $d = \{0, 3.5\}$ mm with $l_x = l_y = 10$ mm are applied. The other parameters for the source spaces are set as described previously. Furthermore, the cylindrical permanent magnet is modeled with one magnetic dipole. The x- and y-position of the magnetic dipole correspond to the center of gravity of the permanent magnet. The local z-position is set to $z_\alpha = \alpha H_p$. The parameter α is determined using the optimization procedure, which has been introduced for the magnetic dipoles model (MDM) in Section 3.2.3. The optimized α equals 0.36. The MDM with more than one magnetic dipole is not applied, because it does not allows to formulate the inverse problem into a linear system of equation as in (4.5). This would result into a significant increase in the computing time.

In all of the reconstructions, the area opening procedure is applied to the binary conductivity distribution after convergence. A 4-connected neighborhood is used and voxel concentrations that comprise less than 4 connected voxels are removed. Due to the stochastic nature of the DE, the optimization process is repeated 50 times. Since the Kolmogorov-Smirnov test [29] cannot reject the hypothesis, that the results are normally distributed, the mean value and the standard deviation are calculated for the 50 defect reconstructions.

4.3 Results

4.3.1 Parameter Studies

The average results obtained in the studies of variations in the parameters F and C_r using $\vartheta = 0.5$ and $\Delta x = \Delta y = 1$ mm are shown in Figures 4.6, 4.7, and 4.8 for $N_p = 20$, $N_p = 40$, and $N_p = 60$, respectively. In the Figures 4.6(a), 4.7(a), 4.8(a) it can be observed that for any C_r a corresponding F with minimum NRMSE of approximately 2.5 % exist. If $N_p = 40$, all minima lie at $F = 0.5$. In addition, for each C_r, the location error has a minimum with an intermediate F around 0.5. The maximum surface area can be observed for a
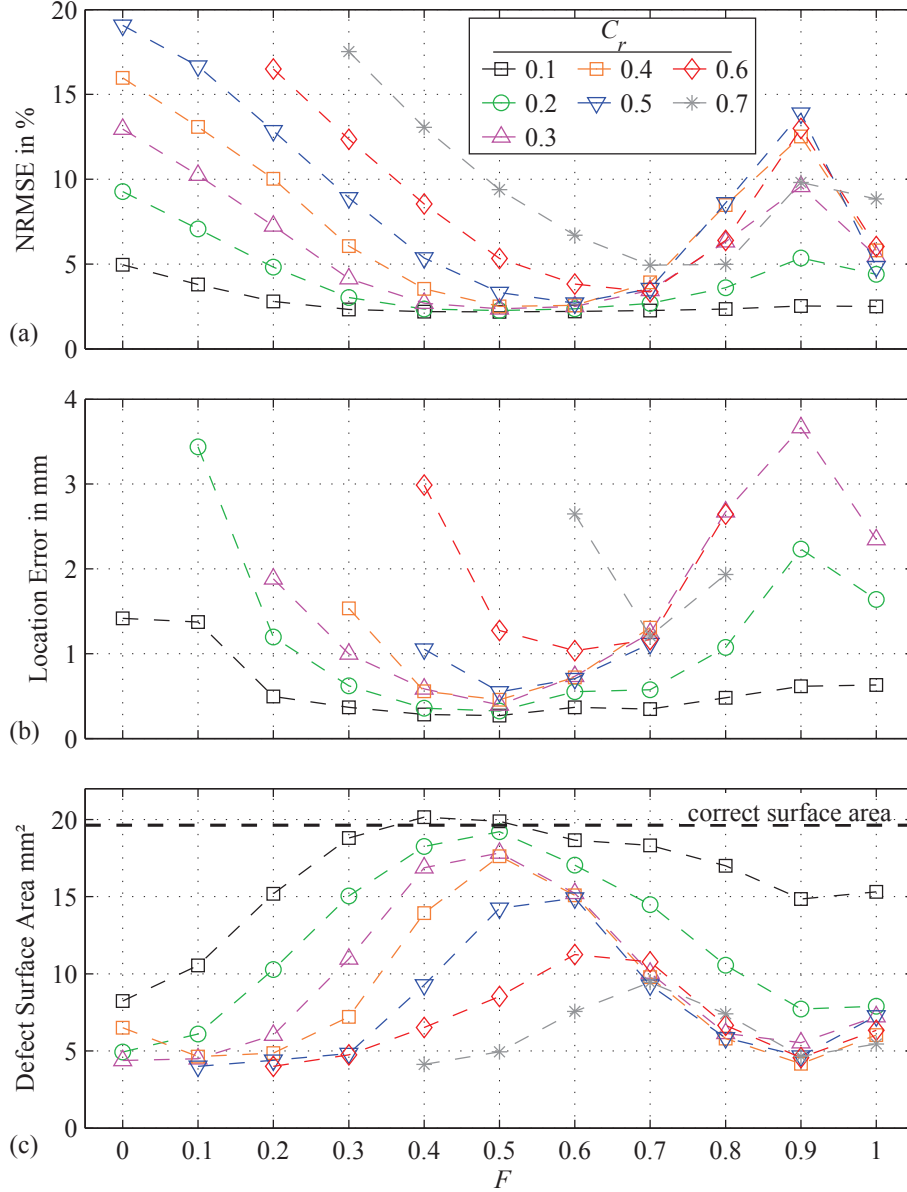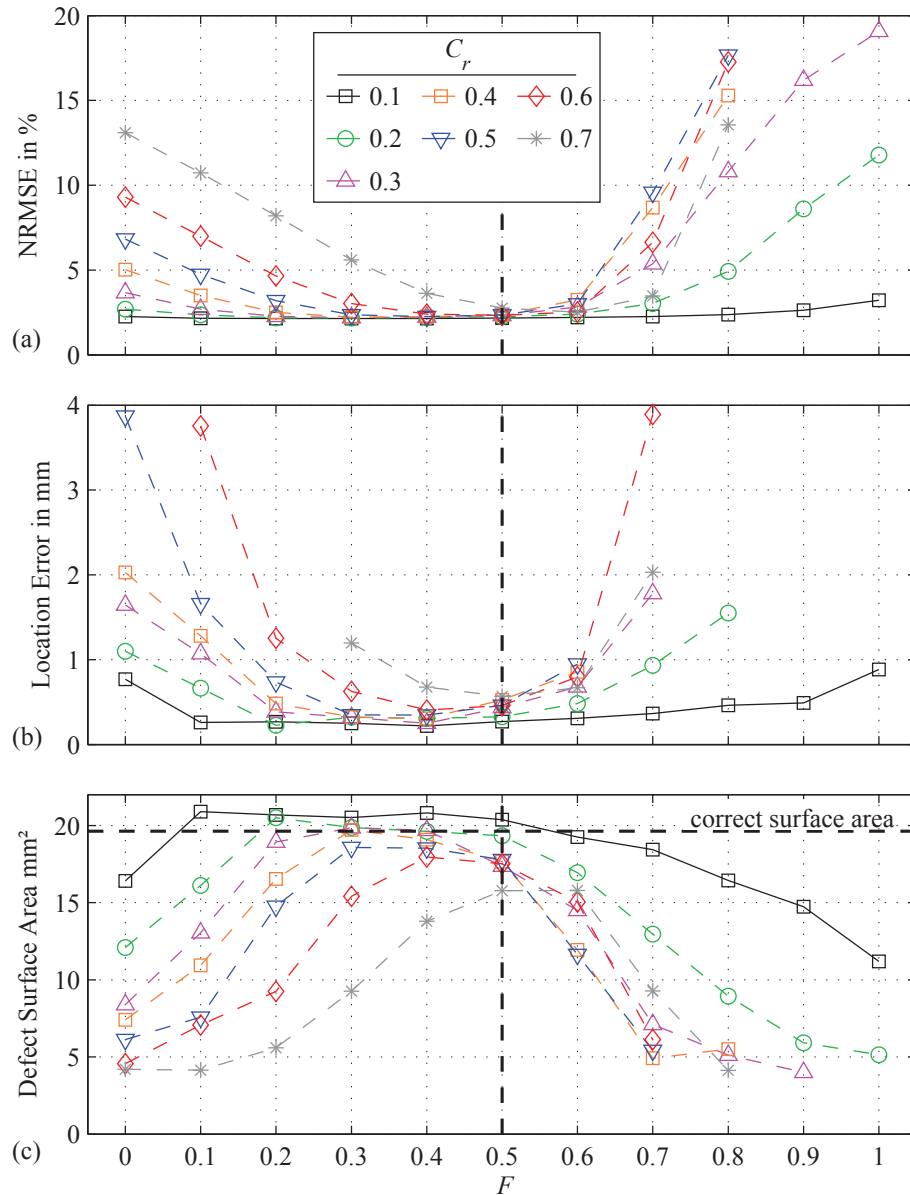
Figure 4.6: Results of parameter studies for combinations of F and C_r with $N_p = 20$, $\vartheta = 0.5$, and $\Delta x = \Delta y = 1\,\mathrm{mm}$. (a) NRMSE after termination of the DE, (b) location error, (c) estimated defect surface area. For visualization purposes C_r is restricted to $\{0.1, 0.2, \ldots, 0.7\}$. Other values did not yield better results. The results were averaged over 50 optimization runs. The bold horizontal dashed line in (c) indicates the correct surface area of the defect ($S_D = \pi R_d^2 = 19.635\,\mathrm{mm}^2$). Parameter combinations without values were outside the selected y-axis range.

minimum location error. For a constant F, the reconstruction results are approximately improved by decreasing C_r. Overall, C_r should be small and F should have intermediate values. Some of the best combinations of $\{C_r, F\}$ are $\{0.1, 0.5\}$ and $\{0.2, 0.5\}$. For any N_P the first parameter combination has a smaller error for the location but a higher one for the surface area, and vice versa. A comparison across the N_p shows that with increasing
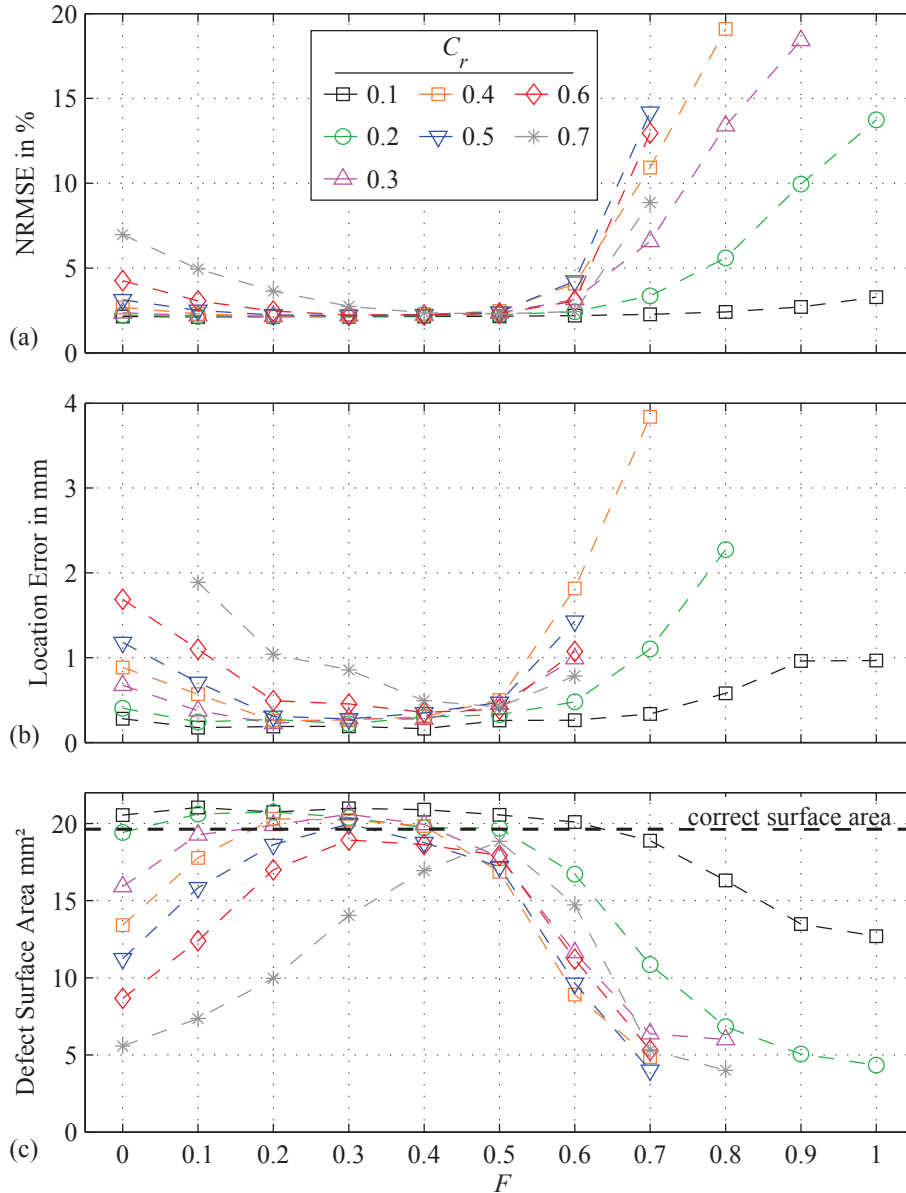
Figure 4.7: Results of parameter studies for combinations of F and C_r with $N_p = 40$, $\vartheta = 0.5$, and $\Delta x = \Delta y = 1$ mm. (a) NRMSE after termination of the DE, (b) location error, (c) estimated defect surface area. The bold vertical dashed lines indicate the optimal $F = 0.5$. The optimal $C_r = 0.1$ is shown by the solid black curves. Further information concerning the visualized values are given in the caption of Figure 4.6.

N_p the NRMSE curves flatten. However, deviations in the results for optimal parameter combinations are negligible. If $N_p = 40$ and $N_p = 60$ results are more stable across varying parameters than for $N_p = 20$.

The threshold variation results are shown in Figure 4.9. The intrinsic control parameters are set to $N_p = 40$, $F = 0.5$, and $C_r = 0.1$, as well as $\Delta x = \Delta y = 1$ mm. The NRMSE obtained

Figure 4.8: Results of parameter studies for combinations of F and C_r with $N_p = 60$, $\vartheta = 0.5$, and $\Delta x = \Delta y = 1\,\mathrm{mm}$. (a) NRMSE after termination of the DE, (b) location error, (c) estimated defect surface area. Further information concerning the visualized values are given in the caption of Figure 4.6.

at termination of the DE increases slightly as the threshold increases (Figure 4.9(a)). However, this behavior is not observed for the location error and surface area (Figures 4.9(b) and 4.9(c)). The mean values fluctuate around $0.25\,\mathrm{mm}$ and $20\,\mathrm{mm}^2$, respectively. It should be noted that the location errors are marginal compared with the defect size. Moreover, the standard deviations are in the range of $0.1\,\mathrm{mm}$ to $0.2\,\mathrm{mm}$ and $1\,\mathrm{mm}$ to $2\,\mathrm{mm}$ for the location error and estimated surface area, respectively. Thus, they are similar for all of the evaluated values of ϑ. Without showing detailed results, similar relations are obtained

for the other parameter combinations. Thus, the DE appears to be sufficiently versatile to adapt to any threshold and no explicit recommendations can be made for setting the threshold.
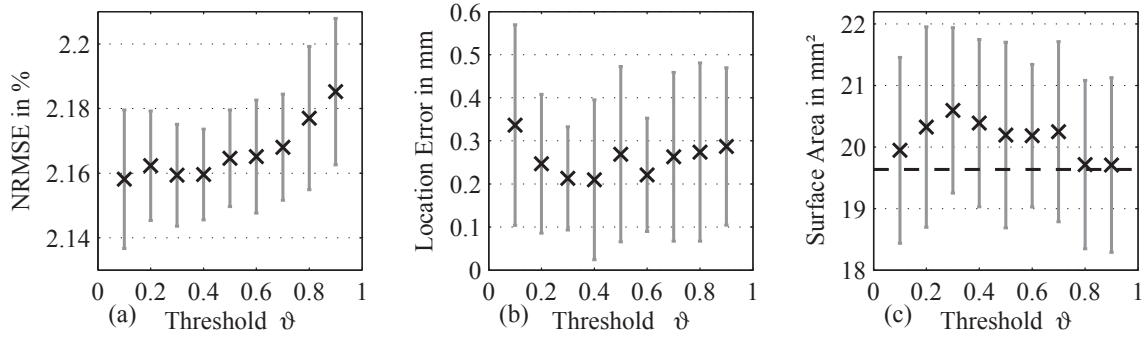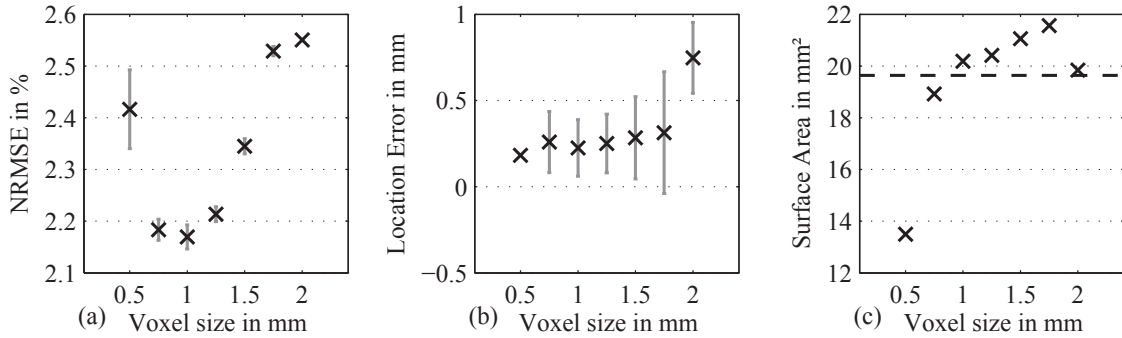

Figure 4.9: Results of the threshold variation studies: (a) NRMSE, (b) location error, (c) estimated defect surface area. The parameters are set to $N_p = 40$, $F = 0.5$, $C_r = 0.1$, and $\Delta x = \Delta y = 1\,\text{mm}$. Black crosses and gray error bars represent the mean and standard deviation over 50 optimization runs, respectively. The dashed line in (c) indicates the correct surface area of the defect.

Figure 4.10 shows the results for variation of the voxel size. Results are shown for $N_p = 40$, $F = 0.5$, $C_r = 0.1$, and $\vartheta = 0.5$. The results for $\Delta x = \Delta y = 0.25\,\text{mm}$ are not shown, because the NRMSE exceeds 15 %. A minimum NRMSE of 2.17 % can be observed at $\Delta x = \Delta y = 1\,\text{mm}$. The corresponding errors in the location and surface area equal 0.24 mm and 0.55 mm^2, respectively. These values provide a better defect estimation than the values obtained for $\Delta x = \Delta y \in \{0.75, 1.25\}$ mm.

Figure 4.10: Results of the voxel size variation study: (a) NRMSE, (b) location error, (c) estimated defect surface area. The DE parameters were set to $N_p = 40$, $F = 0.5$, $C_r = 0.1$, and $\vartheta = 0.5$. The dashed line in (c) marks the correct surface area.

In summary, the DE parameters are set to $N_p = 40$, $F = 0.5$, $C_r = 0.1$, and $\vartheta = 0.5$ for further inverse calculations. $N_p = 40$ is preferred to $N_p = 60$, because the less populations members are considered the less computational cost the algorithm requires. The voxel extensions are selected as $\Delta x = \Delta y = 1\,\text{mm}$. For these settings, the average number of generations required to converge is approximately 3000 and the averaged standard deviation

is 700. Figure 4.11 shows an example of the convergence graph obtained using a double-logarithmic scale for a single DE optimization, which indicates that the goal function value decreases monotonically. This is a property of the DE [88]. Furthermore, the CPU time required for a single DE optimization using the optimized control parameters was in the range of 15 s to 25 s (Dual CPU Intel® Xeon® E5-2687Wv3, 3.1 GHz, 128 GB RAM, 64-bit Gentoo Linux, MATLAB® R2015a).
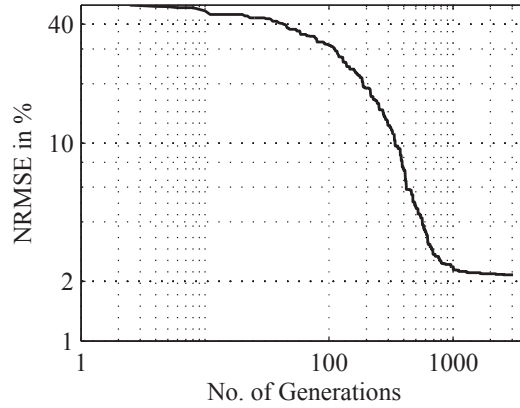

Figure 4.11: Convergence graph for one DE optimization using the optimal parameter settings: $\{N_p, F, C_r, \vartheta\} = \{40, 0.5, 0.1, 0.5\}$.

4.3.2 Inverse Solutions

Simulated Data   Using the optimization parameters determined in Section 4.3.1, the depth of the defect is localized correctly for both data sets (Figure 4.12). The minimum NRMSE for $d = 2\,\text{mm}$ is obtained with a value of 2.17 %, which is smaller than that for $d = 4\,\text{mm}$ (2.51 %).
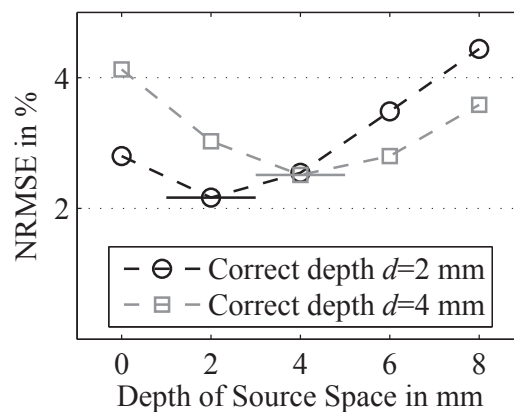
Figure 4.12: NRMSE for source spaces with different defect depths. The DE parameters are set to $N_p = 40$, $F = 0.5$, $C_r = 0.1$, and $\vartheta = 0.5$. Ensemble averages over 50 optimization runs are depicted. The horizontal lines indicate the minimum NRMSEs for the evaluated depths.

Table 4.2 shows the location error and reconstructed defect surface area for both data sets. The position errors are marginal compared with the defect size. The surface area is reconstructed with errors of $2\,\%$ and $4\,\%$ compared with the correct value. It can be observed that the inverse calculations are more accurate for the defect located in the second metal layer compared with that in the third layer.

Table 4.2: Reconstructed defect geometry parameters for the simulated data sets. The values are averaged over 50 optimization runs.

Data set index (Defect depth in mm)	1(2)	2(4)
Location error in mm	0.25	0.33
Defect area in mm^2	20.025	18.878

Figure 4.13 shows an example of a reconstructed conductivity distribution. The few artifacts visible in (a) and (b) are removed using the area opening procedure (c).
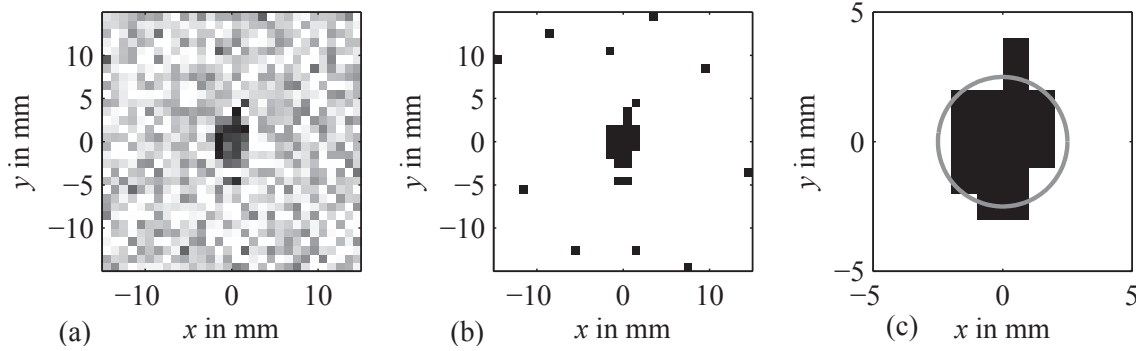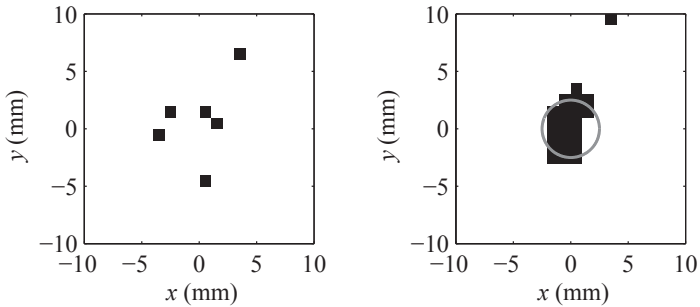
Figure 4.13: Reconstructed conductivity distribution: (a) continuous DE solution, (b) thresholded binary distribution, and (c) solution after applying the area opening procedure. The circle in (c) indicates the real defect. Black denotes $\sigma = \sigma_0$ and white denotes $\sigma = 0$.

Measured Data   The results obtained for the measured data are summarized in Table 4.3. The NRMSE is smaller for the bottom cover plate, which corresponds to the correct depth. However, the differences in the NRMSE are small between the top and bottom cover plate. To confirm the depth estimation, the inverse solutions prior to the area opening are also compared (fourth row of Table 4.3). A connected area that could be interpreted as a defect is observed only for the bottom cover plate, but not the top cover plate. The similar NRMSE for the top cover plate is due to the ill-posed nature of the problem.

For the bottom cover plate, the location error is much smaller than the defect radius. Moreover, the estimated defect surface area equals $19.93\,\text{mm}^2$, i.e. it has an error of $1.6\,\%$ relative to the real value. The mean number of generations until termination is approximately 2000 and the averaged CPU time required is $15\,\text{s}$.

Table 4.3: Reconstruction results for the measured data. The values are averaged over 50 optimization runs. The real defect is located at $d = 3.5$ mm and it has a surface area of $\pi R_d^2 = 19.635$ mm^2. Examples of the conductivity distributions before applying the area opening procedure are shown.

Depth of source space in mm	0 (top cover plate)	3.5 (bottom cover plate)
NRMSE in %	8.96	8.85
Location error in mm	-	0.33
Defect area in mm^2	-	19.93
Thresholded inverse solution		

4.4 Discussion

In this chapter, an inverse calculation strategy based on a stochastic optimization algorithm called DE was proposed. The findings show that the reconstruction scheme yielded correct depth estimates. The geometry estimates had errors less than 4 % relative to the size of the defect. Other reconstruction approaches for LFE have obtained comparable errors [81].

In the inverse strategy, the binarization of continuous-valued population members and area opening to obtain the DE solution is employed. These processing steps accelerate the convergence of the DE. Without these steps, it is likely that the DE would be able to converge to a similar final solution if the termination criterion is changed, i.e., more function evaluations would be required without changing the overall best solution.

Differential mutation and one-to-one selection are reported to be the strengths of the DE compared with other evolutionary strategies [18]. Differential mutation ensures a high population diversity and improves the convergence. Individuals adapt to the search space because the scaled difference vectors gradually conform to the space. It is not necessary to use a predefined probability density function to define the step size, which is also the case for other stochastic optimization algorithms. One-to-one selection ensures that the overall best solution is retained. These aspects have contributed to selecting the DE algorithm.

Furthermore, the continuous-valued DE individuals allow us to drop the assumption that the defect has zero conductivity in future studies. By omitting the binarization for selection operation, other defects can be analyzed in addition to metal fractures, such as corrosion. This extension would be more difficult to achieve with a binary-valued algorithm,

e.g., a genetic algorithm.

Based on parameter studies, the intrinsic control parameters of the DE were determined. The control parameters have been varied in discrete steps. This was preferred to an automatic determination of the parameters by, e.g., self-adapting techniques [18]. The approach allows to visualize and evaluate the performance over a wide range of parameter combinations. Further, it can be assessed how not only the final goal function value but also the location error and surface area of the defect depend on the control parameters. Such a distinct analysis is challenging with an automatic procedure, because the goal function has to be a function of all three parameters.

The results of the parameter studies show that the optimal DE control parameters for LFE are $N_p = 40$, $F = 0.5$, and $C_r = 0.1$. Similar values were recommended in previous studies based on problems with only a few optimization variables [18, 35, 88, 107]. It has been reported that N_p should lie between $5N_S$ and $10N_S$, where N_S is the dimensionality of the problem. However, N_p should not exceed 40. Furthermore, if C_r is small, the number of exchanged elements is small and each direction of the search space is explored more or less independently. This is effective if the goal function is separable, as found in LFE, i.e., $f(\boldsymbol{\sigma}) = \sum_{k=1}^{N_S} f_k(\sigma_k)$ (equations (2.9) and (4.6)). Moreover, it has been proposed that F should be set between 0.4 and 0.9 to ensure that the trial and mutant vectors are significantly different, while maintaining the high diversity of the population .

The reconstruction results are more accurate when the defect was located closer to the surface of the conductor (Table 4.2). The reason might be that the influence of the metal layers between the permanent magnet and the layer containing the defect on the force signals were not considered in the approximate forward solution. Further, Figure 4.13 and Table 4.3 show that the reconstructed defect has a slightly smaller x-extension but slightly larger y-extension than the real defect. This phenomenon is likely to be explained by two aspects. First, the resolution of Lorentz force eddy current testing (LET), is poorer in the y- than in the x-direction. Because the eddy currents below the permanent magnet flow in the y-direction, the magnitude decay is slower in the y- than in the x-direction (Figure 2.5). Second, the y-extension of the sensor space is too small to provide sufficient information about the y-extension of the defect. However, the current experimental setup does not allow to increase the y-extension of the sensor space. A possible solution to overcome this drawback is to measure the specimen twice, whereas in the second measurement the specimen in rotated by 90 degress in the xy-plane.

In this study, the permanent magnet was modeled with one magnetic dipole having an optimized position, although an MDM with more than one magnetic dipole would provide a more accurate solution of the magnetic field. The reason was that the use of the MDM does not allow to formulate the inverse problem into a linear system of equations. This would yield a significantly increased computing time.

Furthermore, the optimization problem considered in this study has 900 unknowns

(voxels in the source space) if $\Delta x = \Delta y = 1\,\text{mm}$. Therefore, it can be treated as a high-dimensional nonlinear problem. The complexity increases with the dimension of the problem, so the performance of the DE is often expected to be degraded for problems with a large number of optimization variables [18]. This explains the less accurate results if the voxel size is below $1\,\text{mm}$ (Figure 4.10). In the present study, it was showed that the basic DE provides robust and satisfying inverse solutions within a reasonable computational time when applied to the LFE problem with appropriate voxel size.

Two aspects can be addressed as limitations of the proposed method. These are on the one hand the errors in the approximate forward solution. Only the first approximation of forward calculated signals was considered, because the determination of the eddy currents for multiple defect regions with arbitrary shape, that are likely to occur during the optimization, is challenging (Section 2.4.1). For simulation data these errors are in the range of a few percent (Section 2.4.1). However, a comparison between the measured and forward calculated DRSs in Figure 4.14 shows that the presence of interfering signals yield significantly larger deviations for the measured Lorentz forces. This explains the larger NRMSEs obtained after DE convergence and impedes the depth reconstruction. On the other hand the resolution of the system might be not good enough to obtain more accurate depth reconstruction for measured data. The resolution can be improved by applying complex magnet systems.
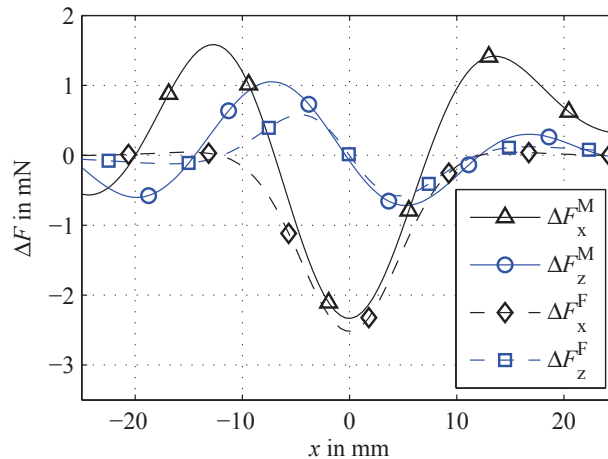

Figure 4.14: Comparison of measured (superscript "M") and forward calculated (superscript "F") DRS components ΔF_x and ΔF_z. The data is shown in the symmetry line of the LET setup. Please note that the ΔF_y-component is not shown, because it vanishes theoretically at the symmetry line.

5 Current Density Reconstructions for Lorentz Force Evaluation

5.1 Introduction

In this chapter, current density reconstructions (CDR) are performed for inverse calculations of defects in Lorentz force evaluation (LFE). It is proposed to estimate the defect geometry based on a reconstructed mean eddy current distribution. This approach is motivated by the interpretation of the defect response eddy current distribution (DRCD) in the defect region as an extended current source.

As outlined in Section 2.5.2 minimum norm estimates (MNE) are applied to calculate the solutions. In this context, the question arises which norm is most suitable for LFE, because the applied norm has significant influence on the solution. The L_2-norm tends to yield smeared solutions [31]. Contrary, the L_1-norm promotes both focused and sparse solutions [118]. In order to balance these constraints, the general L_p norm with $1 \leqslant p \leqslant 2$ is used and the inverse solutions are compared.

For comparison purposes, the inverse solutions for different norms are analyzed statistically. An equivalent ellipsoid approach is used, which has been introduced for postprocessing of distributed current sources in biomagnetic inverse problems. This approach enables a parametrization and easy visualization of the dominant components of the reconstructed current density distributions [106, 130].

In general, the MNE approach results in an ill-posed inverse problem. Since the condition of the inverse problem depends on the used sensor and source spaces [27], the condition number of the gain matrix is calculated for different setups prior to inverse calculations. Based on the results, appropriate sensor and source spaces are selected.

The CDR are applied to the measured Lorentz force data obtained from the Alucobond composite described in Section 4.2.3. The data preprocessing is the same as outlined in Section 4.2.3.

The remainder of this chapter is structured as follows. In Section 5.2 the methods used are outlined. The interpretation of the defect as an extended current source is justified and inverse solutions for the CDR are described. The applied matrix condition measure is explained, followed by the postprocessing operations. In Section 5.3 the results are presented, i.e., the evaluation of the gain matrices and the statistical comparison of the CDR. Finally, the results are discussed in Section 5.4. The main methods and results of this study are published in [68, 70].
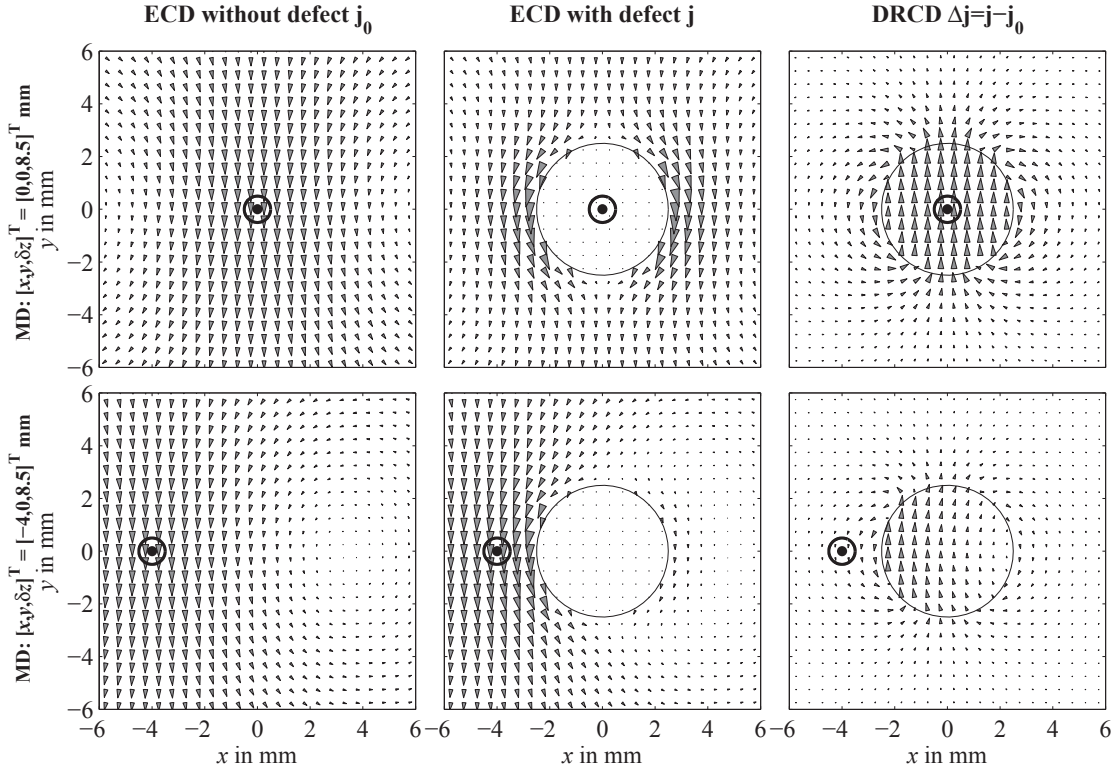
Figure 5.1: Two-dimensional eddy current distributions (ECDs) $\mathbf{j}_0$, $\mathbf{j}$, and $\Delta\mathbf{j}$ shown for two measurement points with a time difference of 0.4 s. They are calculated using methods and parameters given in Section 2.4.1. The circle indicates the defect. The magnetic field is directed out of the page. The position of the magnetic dipole is marked with $\odot$.

5.2 Methodology

5.2.1 Current Density Reconstruction Methods

Basic Concepts Figure 5.1 shows the eddy current distribution without a defect $\mathbf{j}_0$, with a defect $\mathbf{j}$, and the DRCD $\Delta\mathbf{j}$ for a laminated specimen in the mid-plane of the defect, i.e., the xy-plane. Eddy current distributions are calculated for the Lorentz force eddy current testing (LET) benchmark problem outlined in Section 2.4.1 using the forward solution with the extended area approach (EAA). Note that $\mathbf{j}$ is calculated as $\Delta\mathbf{j} + \mathbf{j}_0$. Eddy current distributions are depicted for two measurement points with a time difference of 0.4 s. For the upper and lower rows, the magnetic dipoles are positioned at the points $\mathbf{r}_0 = [0, 0, 8.5]^\mathrm{T}$ and $\mathbf{r}_0 = [-4, 0, 8.5]^\mathrm{T}$ mm above the conducting plate respectively.

Due to the relative movement and the inhomogeneous magnetic field, the eddy current distribution varies during measurements. The eddy currents $\mathbf{j}_0$ are strongest below the location of the magnetic dipole and form two counterrotating eddies [86, 117]. In the defect region the DRCD $\Delta\mathbf{j}$ must counterbalance $\mathbf{j}_0$, so that $\Delta\mathbf{j} = -\mathbf{j}_0$. Since the current dipoles in the defect region serve as eddy current sources, the DRCDs are characterized by large magnitudes concentrated in the defect region. Outside the defect region, the magnitudes of

the eddy currents decay. Therefore, the defect can be interpreted as a distributed current source. It is the most dominant region in the DRCD. Despite the time-varying nature of the system, this holds for all measurement points.

Because of $\nabla \cdot \mathbf{j} = 0$, averaging the current density in the source space over all force measurement points would yield a vanishing eddy current distribution if the sensor and source spaces had the same xy-dimensions as the conductor. However, in LFE, the sensor and source spaces have significantly smaller extents than the test specimen. They are constrained to the vicinity of the defect because only the perturbations in the force signals are of interest (Figure 5.2). Note that due to the influence of the dimensional differences, the boundary conditions at the edges of the source space can be neglected.
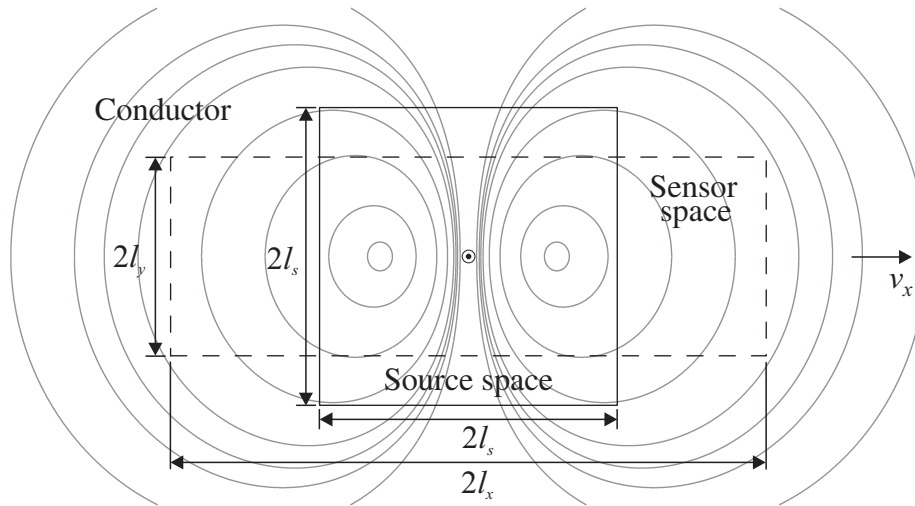
Figure 5.2: Schematic setup of the the dimensional differences between the conductor, the sensor space, and the source space. The streamlines indicate the DRCD calculated for the benchmark problem and the forward solution in Section 2.4.1. The magnetic dipole is positioned above the center of the source and sensor spaces ($\odot$). The edges of the conductor are not shown. The extents of the sensor space in the x- and y-direction are denoted by l_x and l_y respectively. The size of the quadratic source space is denoted by l_s.

If the eddy current density is averaged using the constraint source and sensor spaces, it does not vanish. Figure 5.3 shows $\mathbf{j}_0$, $\mathbf{j}$ and $\Delta\mathbf{j}$ from Figure 5.1 averaged over 357 measured points uniformly distributed in the region $-25\,\mathrm{mm} \leqslant x \leqslant 25\,\mathrm{mm}$, $-6\,\mathrm{mm} \leqslant y \leqslant 6\,\mathrm{mm}$, $z_0 = 8.5\,\mathrm{mm}$. The corresponding LFE parameters are given in Section 2.4.1. Compared to the eddy current distributions for one measured point (Figure 5.1), differences in $\mathbf{j}_0$ and $\mathbf{j}$ are visible. The decrease in the magnitude of the eddy currents $\mathbf{j}_0$ and $\mathbf{j}$ in the negative and positive x-directions is reduced. However, a dominant region with highest magnitudes in the defect region is visible. Therefore, the interpretation of the defect as an extended current source also holds for the average DRCD. Note that the magnitude of the DRCD in Figure 5.3 is smaller than in Figure 5.1. This line of argument justifies to reconstruct a mean current density distribution, which provides a sufficient representation of the correct DRCD.
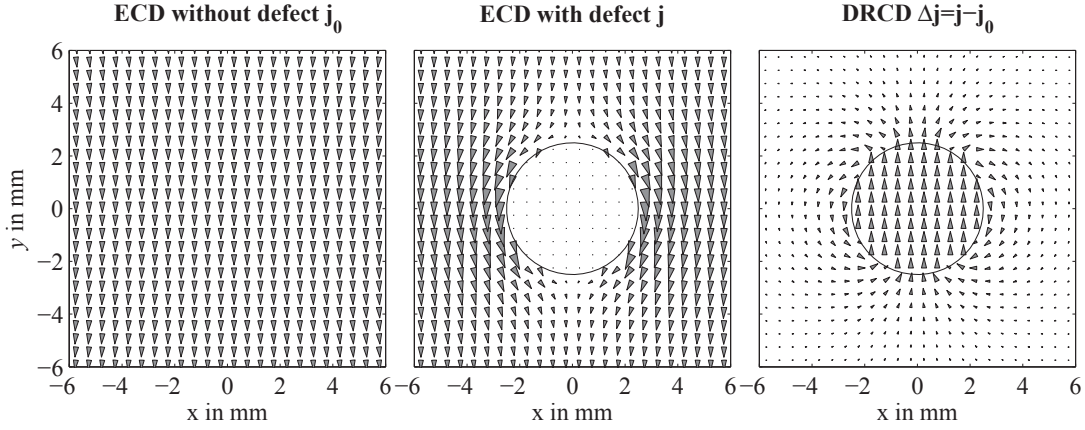
Figure 5.3: Eddy current distributions (ECDs) $\mathbf{j}_0$, $\mathbf{j}$, and $\Delta\mathbf{j}$ averaged over 357 measured points, which are uniformly distributed in the region $-25\,\text{mm} \leqslant x \leqslant 25\,\text{mm}$, $-6\,\text{mm} \leqslant y \leqslant 6\,\text{mm}$, $z_0 = 8.5\,\text{mm}$.

Inverse Solution Based on the preceding analysis the linear inverse problem for the CDR is formulated as

$$\Delta\mathbf{F} = \boldsymbol{K} \cdot \mathbf{p} + \mathbf{e}. \tag{5.1}$$

The vector $\mathbf{p} \in \mathbb{R}^{2N_S \times 1}$ contains the moments of the N_S two-dimensional dipoles representing the average DRCD. The matrix $\boldsymbol{K} \in \mathbb{R}^{3M \times 2N_S}$ is the gain matrix between the N_S unknown conductivities of voxels from the source space and the defect response signal (DRS) at M measurement points. The gain matrix comprises information about the relation between sensor and source space. The inverse problem is formulated using one magnetic dipole as the magnetic field source. If more than one magnetic dipoles are used, the formulation of the inverse problem into a linear system of equations would not be possible.

The dipoles have two dimensions (p_x and p_y), because the thickness of the cover plates of the composite are much smaller than its extent. Thus, the z-component of the eddy currents is set to zero (Section 2.4.1). The vector $\mathbf{e}$ compensates for the error resulting from averaging the DRCDs over all measured points. Furthermore, $\mathbf{e}$ contains additional information about noise and disturbances in the data.

For reconstruction the L_p-norm approach is used. The squared deviation Δ^2 between the forward calculated Lorentz forces ΔF in equation (5.1) and the DRS [31, 119] is minimized

$$\underset{\mathbf{p} \in \mathbb{R}^{2N_S \times 1}}{\arg\min}\ \Delta^2(\mathbf{p}) = \|\boldsymbol{K}\mathbf{p} - \Delta\mathbf{F}\|^2. \tag{5.2}$$

Introducing a regularization term in equation (5.2) yields

$$\underset{\mathbf{p} \in \mathbb{R}^{2N_S \times 1}}{\arg\min}\ \Delta^2(\mathbf{p}) = \|\boldsymbol{K}\mathbf{p} - \Delta\mathbf{F}\|^2 + \lambda\|\boldsymbol{W}\mathbf{p}\|^2 = \mathbf{D}(\mathbf{p}) + \lambda\mathbf{M}(\mathbf{p}), \tag{5.3}$$

where λ denotes the regularization parameter and $\boldsymbol{W} \in \mathbb{R}^{3M \times 2N_S}$ the weighting matrix. The

data and the model term are defined as

$$\mathbf{D}(\mathbf{p}) = \|\boldsymbol{K}\mathbf{p} - \Delta\mathbf{F}\|_{p_d} \quad \text{and} \quad \mathbf{M}(\mathbf{p}) = \|\boldsymbol{W}\mathbf{p}\|_{p_m}, \tag{5.4}$$

respectively. The applied norm is denoted by $1 \leqslant p_d, p_m \leqslant 2$. Regularization is of special interest in CDR for LFE because an optimal inverse solution reflects an average best fit for all measured points. Therefore, the inverse solution can have a residual error even if the problem is well-posed.

To address the issue of a suitable norm, the applied norm $p = p_d = p_m = \{1, 1.25, 1.5, 1.75, 2\}$ was varied. A component-wise depth weighting of the current components compensates for the bias towards superficial and nearby sources. The diagonal elements of the weighting matrix $\boldsymbol{W}_{i,i}$ are calculated from the columns $\mathbf{k}_i$ of the gain matrix $\boldsymbol{K}$ with $i = 1 \ldots 2N_S$ as

$$\boldsymbol{W}_{i,i} = \frac{1}{\sqrt{\|\mathbf{k}_i\|_2}}. \tag{5.5}$$

Furthermore, the regularization parameter was varied according to a logarithmic scheme $\lambda = \{0.1, 0.316, 1, 3.16, 10, 31.6, 100, 316, 10^3, 3.16 \cdot 10^3, 10^4\}$. This approach was chosen because well-known methods to determine λ, e.g., L-curve [42] or generalized cross-validation [37], did not yield satisfactory results. To minimize equation (5.3), an iteratively reweighted least-squares optimization algorithm [79] incorporated in the CURRY Neuroimaging Suite (Version 7.0, Compumedics Neuroscan Inc., Charlotte, USA) software was used.

The CDR are applied to the measured data obtained from the Alucobond composite (Section 4.2.3). The cylindrical permanent magnet used in the experimental setup is modeled with one magnetic dipole positioned at $\mathbf{P}_0 + z_\alpha \mathbf{e}_z = \mathbf{P}_0 + \alpha H_p \mathbf{e}_z$, where $\mathbf{P}_0 = [0, 0, \delta z]$ denotes the position of the permanent magnet and z_α the local position of the magnetic dipole in the permanent magnet. The local position depends on the parameter $\alpha = 0.36$ that is determined using the optimization procedure for the magnetic dipoles model described in Section 3.2.3.

5.2.2 Condition of the Gain Matrices

To determine the degree of ill-conditioning of the gain matrix $\boldsymbol{K}$ the measure of condition ρ is calculated [27]

$$\rho(\boldsymbol{K}) = \frac{\sigma_1(\boldsymbol{K})}{\frac{1}{N}\sum\limits_{i=1}^{N}\sigma_i(\boldsymbol{K})}. \tag{5.6}$$

Thus, ρ represents the ratio between the largest and the mean singular value of $\boldsymbol{K}$. Unlike the well-known condition number with respect to the L_2-norm κ [98], ρ is more robust to compute and does not depend heavily on the smallest singular value. Numerical errors are less likely to occur during computation. A larger value of ρ indicates a more ill-posed problem.

Sixteen sensor space setups are investigated. They differ in four parameters: the extent

in x-direction l_x with $-l_x \leqslant x \leqslant l_x$, the extent in y-direction l_y with $-l_y \leqslant y \leqslant l_y$, the distance between observation points in the x-direction d_x, and the distance between the scanning lines d_y (Figure 5.2). All combinations of $l_x = \{25, 35\}$ mm, $l_y = \{6, 10\}$ mm, $d_x = \{1, 2\}$ mm, and $d_y = \{1, 2\}$ mm are assessed. For the measured data, the d_x values correspond to a downsampling of the data to $f_{s,x} = \{250, 500\}$ sps. The sensor spaces are positioned at the z-positions of the magnetic dipoles representing the corresponding cylindrical magnet, i.e., at $z = \delta z + {}^{H_P}\!/_2 = 1\,\mathrm{mm} + 12.5\,\mathrm{mm} = 13.5\,\mathrm{mm}$.

The number of assessed source spaces equals 35. The source spaces consist of a two-dimensional quadratic plane located in the middle of the bottom cover plane at $z = -3.75\,\mathrm{mm}$. The dipoles are regularly distributed in the range of $-l_s \leqslant (x, y) \leqslant l_s$. The distance between adjacent dipoles is equal in the x- and y-directions and denoted by d_s. All combinations are considered of $l_s = \{10, 12.5, 15, 17.5, 20\}$ mm and $d_s = \{0.5, \ldots, 2\}$ mm with $\Delta d_s = 0.25$ mm. This yields dipole numbers in the range of 128 ($l_s = 10$ mm, $d_s = 2$ mm) to 12 800 ($l_s = 20$ mm, $d_s = 0.5$ mm).

5.2.3 Postprocessing of the Estimated Current Densities

First, the edge artifacts, which are likely to occur in the CDR [44], are eliminated. Edge artifacts are dipoles positioned at the edges of the source space and having a moment which is twice higher than the mean dipole moment. Secondly, an equivalent ellipsoid is fitted to that region of the current density distribution in which the magnitude was above a certain threshold. Applied to CDR for LFE, it enables extraction of the defect region because this region is defined by the most dominant component of the current distribution (Figure 5.1). The threshold to extract the most dominant region was defined as

$$t_m(\bar{\mathbf{p}}) = 1 - \frac{\sigma_{\bar{\mathbf{p}}}}{\max \bar{\mathbf{p}}}. \tag{5.7}$$

The vector $\bar{\mathbf{p}} \in \mathbb{R}^{2N_S \times 1}$ contains the magnitudes of the dipoles. It holds that $\bar{\mathbf{p}}_n = \|\mathbf{p}_n\|_2 = \sqrt{p_{nx}^2 + p_{ny}^2}$ with $n = 1 \cdots N_S$. Furthermore, $\sigma_{\bar{\mathbf{p}}}$ denotes the standard deviation of $\bar{\mathbf{p}}$. It was possible that more than one connected region would remain after thresholding. In this case, the artifact was eliminated by clustering. The most dominant region is the connected region which contains the most dipoles, i.e., has the largest volume.

Thereafter, the location of the defect is estimated by the center of gravity of the ellipsoid $\mathbf{r}_c = [x_c, y_c]^\mathsf{T}$, which is calculated as the mean position of the dipoles in the dominant region. The direction and lengths (e_x, e_y) of the semi-axis give an estimate of the defect extent and are determined using the weighted dipole distances. The weighting parameters are the respective dipole moments [130].

Then, the root mean square error for location RMSE_c and extent RMSE_{sa} is calculated by comparing the estimated values with the real center of gravity and real radius of the defect. Finally, the reconstruction error is calculated as

$$e_R = \sqrt{\frac{\mathrm{RMSE}_c^2 + \mathrm{RMSE}_{sa}^2}{2}}. \tag{5.8}$$

5.3 Results

5.3.1 Condition Number ρ of the Gain Matrices

Figure 5.4 shows the condition number ρ of the gain matrix for four sensor spaces. These are called A1, A2, B1, and B2 and have 175, 275, 343, and 539 measured points, respectively. All four sensor spaces have the parameters $l_x = 25\,\mathrm{mm}$ and $\Delta y = 2\,\mathrm{mm}$. The letters "A" and "B" represent $f_{s,x} = 250\,\mathrm{sps}$ and $f_{s,x} = 500\,\mathrm{sps}$ respectively. Furthermore, the sensor spaces indexed by "1" and "2" are specified by $l_y = 6\,\mathrm{mm}$ and $l_y = 10\,\mathrm{mm}$ respectively. The results are shown in groups with l_s being the group parameter. In the double-logarithmic scaled figure, the abscissa represents the number of dipoles in the source space K. Therefore, within each group, the distance between adjacent dipoles d_s decreases with increasing K. The vertical dashed lines indicate that value of N_S above which the inverse problem is underdetermined. At this point, it holds $2N_S = 3M$ with respect to the two-component current dipoles and the three-component force signals.
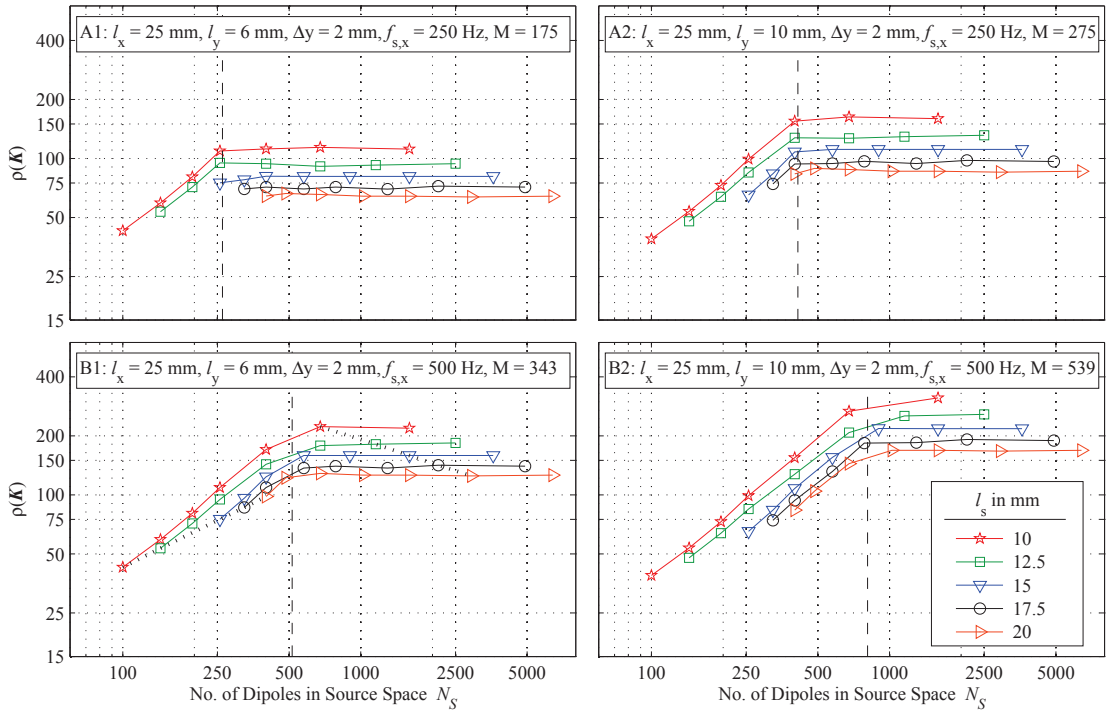
Figure 5.4: Condition number ρ of the gain matrix for the two-dimensional inverse calculations. The subplots depict ρ for four different sensor spaces. The dotted lines in the lower left subplot indicate a comparison among different l_s. The dashed line indicates $2N_S = 3M$.

For an overdetermined inverse problem, ρ increases with increasing K, i.e., with decreasing d_s. If the inverse problem is underdetermined, ρ is approximately constant. If source space B1 is used and the sensor space is defined by $l_s = 15\,\mathrm{mm}$ and $d_s = 1\,\mathrm{mm}$, i.e., $N_S = 900$, ρ is equal to 159.

Moreover, the condition numbers are compared for a fixed sensor space and fixed d_s, but

varying l_s, which determines the number of sources. This evaluation is performed across the groups, as indicated by the dotted lines in the lower left subplot. To evaluate the relationship between ρ and l_s, nth-degree polynomials with $n = \{1, 2, 3\}$ are fitted separately to the data for over- and underdetermined problems, and evaluate the residual fitting errors. It is observed that for an overdetermined problem, ρ increases exponentially with increasing l_s. However, the results show an exponential decrease if the inverse problem is underdetermined. For $l_s = \{10, 15, 20\}$ and $d_s = 0.75\,\text{mm}$ (dashed line), the condition number is equal to $\rho = \{223, 158, 125\}$.

Furthermore, a comparison of the source spaces indexed by "A" and "B" (rows of subplots) shows that an increase in $f_{s,x}$ has a marginal influence for an overdetermined problem. However, it results in an increase in ρ if the inverse problem is underdetermined. A doubled sampling frequency results in an approximately doubled condition number. Additionally, an increase in the number of y-lines used, i.e., $\Delta y = 1\,\text{mm}$, has an impact similar to an increase in $f_{s,x}$.

A comparison between the source spaces indexed by "1" and "2" (columns of subplots) shows that for an underdetermined problem, a larger y-extent yields an increase in ρ. However, for an overdetermined problem, an increase in l_y leads to a slight decrease in ρ. Moreover, if is found without showing detailed results that an enlargement of the x-extent of the source space to $l_x = 35\,\text{mm}$ has no significant influence on the condition number.

5.3.2 Inverse Solutions

The sensor and source spaces for inverse calculations are selected based on the results in Section 5.3.1. A small number of measured points, as in A1, leads to a small condition number because it introduces a relatively small amount of redundancy in the measurement values. However, the amount of information covered is smaller than in a larger sensor space, i.e., B2. With respect to these factors, the sensor spaces A2 and B1 are a good compromise. Moreover, the LFE resolution is higher in the x-direction than in the y-direction. This means that a variation of the defect size in the x-direction can be more accurately detected than a variation in the y-direction [127]. Since sensor space B1 is more in compliance with this aspect than sensor space A2, B1 is applied.

A small sized source space yields a large ρ, and edge artifacts are likely to occur. On the other hand, a larger source space has a smaller ρ, but long computing times as long as d_s is constant. If d_s is small, the computing time is long. Because of the application-oriented nature of this work, all inverse calculations should be able to be carried out on a standard personal computer. Furthermore, the resolution of the source space depends on the desired resolution of the reconstruction. Based on these aspects, a source space specified by $l_s = 15\,\text{mm}$, $d_s = 1\,\text{mm}$, and $N_S = 900$ two-component dipoles is used. This source space exceeded the diameter of the defect by six times. This selection is in good agreement with the recommendations in [11, 27].

In a first evaluation, all inverse solutions are assessed based on two criteria. If both criteria are fulfilled, the inverse solution is rejected.

**First criterion:** The reconstruction error e_R in equation (5.8) exceeds $5\,\text{mm}$.

Second criterion: A visual inspection of the estimated current density distribution does not show any dominant region.

The results for the measured data for the composite are shown in Figure 5.5. An evaluation of the reconstruction error e_R from equation (5.8) for the investigated L_p-norms and the regularization parameter λ is shown in Figure 5.5(a). The L_1-norm is not shown because all results for this norm met the two rejection criteria. For each L_p-norm with $p = \{1.25, 1.5, 1.75, 2\}$, an optimal $\lambda = \{10^3, 3.16, 10, 31.6\}$ with corresponding minimum reconstruction errors $e_R = \{0.88, 0.96, 1.1, 1.1\}$ mm can be observed. Therefore, the $L_{1.25}$ norm has the smallest error and the $L_{1.5}$ norm the second smallest error. The $L_{1.5}$ norm has the
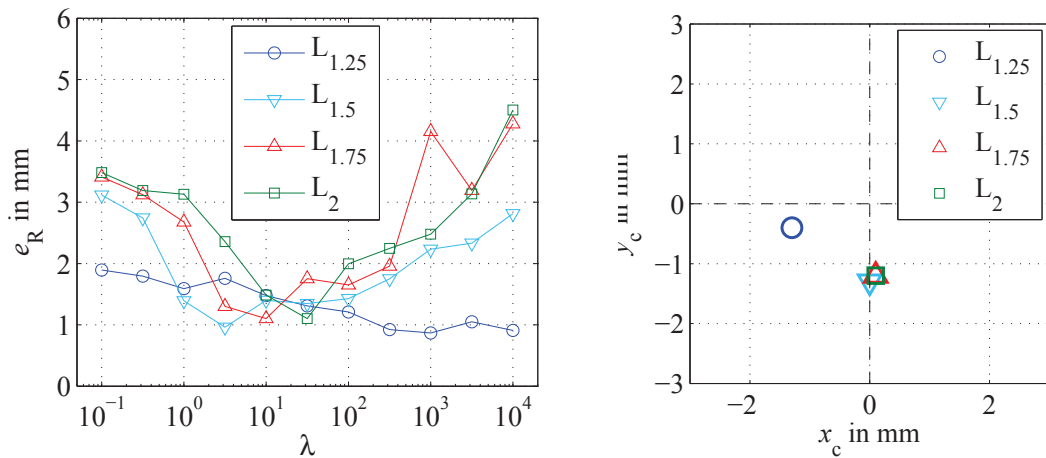
(a) Reconstruction error e_R for all evaluated λ and L_p-norms.

(b) Center of gravity of the ellipsoids. The values are shown for an optimal λ. The real defect is located at $x_c = y_c = 0$ (dashed lines).
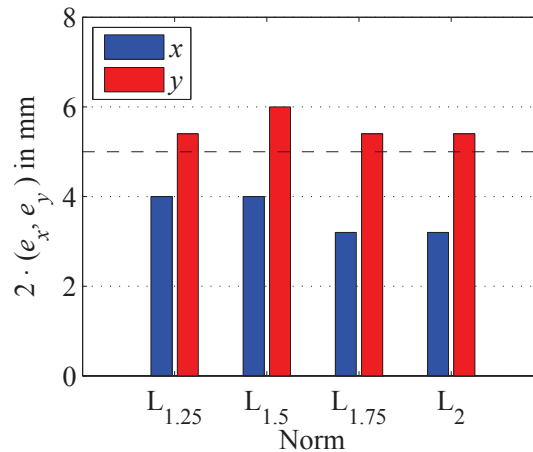
(c) Reconstructed extent of the defect. The results are shown for optimal λ. The dashed line indicates the real diameter of the defect.

Figure 5.5: Results of the inverse calculations and the equivalent ellipsoid fitting procedure. The inverse calculations were performed in a two-dimensional source space.

lowest optimal λ. The differences between the norms using optimal λ is marginal compared to the deviations for different λ within each norm. If $p = \{1.5, 1.75, 2\}$, e_R increases significantly towards the edges of the evaluated interval compared to the optimal values. However, for $p = 1.25$, deviations in e_R between optimal and non-optimal λ are smaller.

Considering the correct position of the defect at $x_c = y_c = 0$, the location errors of the inverse solutions (centers of gravity of the equivalent ellipsoids) corresponding to the minimum e_R for optimal λ have values less than $1.5\,\text{mm}$ (Figure 5.5(b)). The differences in the location errors among the various norms are marginal. For $L_{1.25}$, the error is equal to $-1.3\,\text{mm}$ in the x- and $-0.4\,\text{mm}$ in the y-direction. For the $L_{1.5}$ norm, it is equal to 0 in the x- and $-1.3\,\text{mm}$ in the y-direction.

The reconstructed extents of the defect were estimated using twice the length of the semi-axes of the equivalent ellipsoids, $2 \cdot e_x$ and $2 \cdot e_y$ (Figure 5.5(c)). For all L_p norms, the estimated extent is too small in the x-direction, but too large in the y-direction. The errors for the $L_{1.25}$ and $L_{1.5}$ norms were similar and in the range of $1\,\text{mm}$. Considering the x-extent, they were smaller than for the other two norms. For the $L_{1.5}$ norm, both directions had an error of $1\,\text{mm}$.

Figure 5.6 depicts the estimated and postprocessed current density distributions for $p = 1.5$ and $\lambda = 3.16$. In the unprocessed current density distribution shown at the left-hand side of the figure, the dominant region representing the defect is clearly visible. The edge artifacts have been removed (white spaces). Due to the simplifications in the forward and inverse calculations (Section 5.2.1), the estimated current density distribution is physically not exact, i.e., $\nabla \cdot \mathbf{j} \neq 0$. The right-hand side of the figure shows the equivalent ellipsoid fitted to the thresholded and clustered region. The small errors in the location and extent are clearly visible.

Further, the unexplained variance is calculated for all inverse solutions (Figure 5.7). The unexplained variance is a measure for the goodness of fit of the inverse solutions. The lower the unexplained variance is, the better the solution explains the measured data. Again, the results for combinations of p and λ with $e_R > 5$ are not shown. With increasing λ the unexplained variance increases approximately linear for all L_p norms and a wide range of the evaluated λ. However, at the lower and upper edges of the investigated interval the gradient decreases. Moreover, with increasing p the unexplained variance decreases. The additional squares mark the unexplained variances that correspond to the minimum reconstruction errors. For $p = \{1.25, 1.5, 1.75, 2\}$ these values equal $\{97.3, 56.6, 71.2, 56.4\}$ %. Thus, the solutions obtained from the $L_{1.5}$ and L_2 norm explain the data more reasonably than the solutions obtained from the $L_{1.25}$ and $L_{1.75}$ norm.

The computations of the CDR using the L_p norm are performed on a desktop computer that has the following specifications: Quad-Core CPU Intel® Core™ i7-3770, 3.4 GHz, 16 GB RAM, 64-bit Microsoft Windows 8, Curry 7, MATLAB® R2013a. The CPU time necessary to perform a single inverse calculation is less than $30\,\text{s}$.
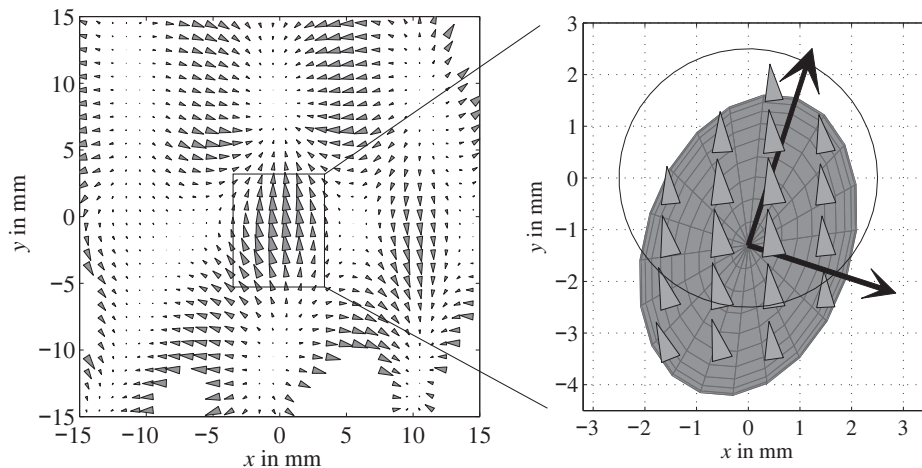
Figure 5.6: Reconstructed current distribution with $p=1.5$ and $\lambda=3.16$. Due to the simplifications in the forward solution the unprocessed current density distribution shown at the left hand side is physically not exact, i.e., $\nabla \cdot \mathbf{j} \neq 0$. Edge artifacts have been removed (white spaces). The right-hand side shows the equivalent ellipsoid fitted to the thresholded distribution. Artifacts remaining after thresholding have been removed by clustering. The circle marks the real defect.
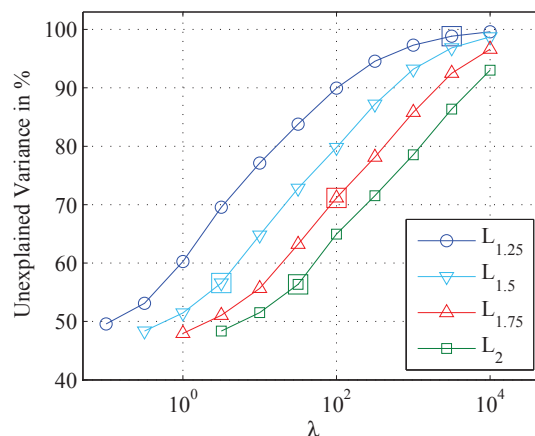

Figure 5.7: Unexplained variances of the inverse solutions. The squares mark the unexplained variances and λ that correspond to the minimum reconstruction error for each L_p norm.

5.4 Discussion

In this chapter, a novel approach for reconstructing defects based on measured data from LET was presented. CDR calculated using MNE with varying L_p norm are used. Measured data obtained from a laminated metal composite, named Alucobond, were investigated. The results show that the reconstruction quality is best for the $L_{1.5}$ norm. The estimate of the lateral position of the defect has an error of $1\,\mathrm{mm}$, i.e., $20\,\%$ relative to the defect diameter. The defect extensions are determined with the same error. However, the error in the total

defect size, i.e., in the surface area of the equivalent ellipsoid $\pi \cdot e_x \cdot e_y$, equals $1.04\,\%$ relative to the real surface area. The large extension errors result from the fact that the x-extension is estimated too small, but the y-extension too large. This has already been observed in the results of the inverse calculation strategy with the Differential Evolution (Figure 4.13 and Table 4.3).

Figure 5.5(a) shows that the reconstruction errors of the $L_{1.25}$ and $L_{1.5}$ norms for the measured data are the lowest among all norms. The optimal regularization parameter is smallest for the $L_{1.5}$ norm. The optimal λ for $p = 1.25$ is comparatively large. Furthermore, it is approximately constant for $\lambda \geqslant 3.16 \cdot 10^2$. These two observations indicate that the data term might be underfitted. The inverse solution would show very little adaptation to the measured data and contain only little information about it. Therefore, the $L_{1.25}$ norm seems not to provide an equally good approach to the $L_{1.5}$ norm.

The study was motivated by the interpretation of the defect as an extended current source (Figures 5.1 and 5.3). As a simplification a current density distribution averaged over all measured points was assessed. This modeling approach lacks physical exactness, i.e., $\nabla \cdot \mathbf{j} \neq 0$, because the extents of the sensor and source spaces are significantly smaller than the conductor. The validity of the assumptions is supported by the reconstruction errors which are in an acceptable range (Figure 5.5).

However, the large unexplained variances in Figure 5.7 show that the inverse solutions explain less than $50\,\%$ of the measured data for any L_p norm. This value is larger compared to CDR in the fields of biomedical engineering, where the residual variances are usually less than $30\,\%$ [38]. This indicates that CDR are a more promising method for biomedical engineering than for LFE.

In contrast to MNE solutions in other applications where the regularization parameter is selected so that no over- or underfitting of the data occurs [31], larger regularization parameters were used for LFE. One source of error could be the simplified model approach, i.e., the averaging over the measured points. Another aspect is that the regularization parameter can be expected to be large if the inverse problem has a large number of observation points as in LFE [38]. For conductivity reconstructions in LFE regularization was also high [81].

Further, it was assumed that the depth has been determined correctly beforehand. This simplification is based on results obtained from previous depth reconstructions with CDR, which have not been successful. Geometry reconstructions for numerically simulated data have a similar accuracy than the presented findings for the measured data under the assumption of correct depth estimation (results not shown). In the numerical simulations a spherical permanent magnet has been applied, which can be accurately represented by one magnetic dipole. Thus, the reconstruction errors are unlikely to result from the error due to modeling the cylindrical permanent magnet applied in the experimental setup with one magnetic dipole.

Inverse calculations using the other source and sensor spaces defined in Section 5.3.1 were performed for further evaluation. Enlargement of the source space in x-direction up

to $l_x = 25$ mm, enlargement of the sensor space in the x- and y-directions, as well as increased resolutions did not yield improved results. However, reductions caused impairment of the inverse solutions. This confirms that appropriate sensor and source spaces were selected. Their parameters and dimensions are not likely to be a reason for any inaccurate inverse solution. The results for ρ in Section 5.3.1 are in good agreement with the results of the condition assessment in [27].

In summary, the reconstruction results indicate that CDR provide a good approximation of the geometry of material defects in LFE. However, a comparison to the results in Chapter 4 and [81] shows that CDR are not the most appropriate method for LFE.

As an extension of the present model, an eddy current density depending on the relative position between conductor and the permanent magnet should be considered. Further, other norms, e.g., the Sobolev norm, can be applied for regularization [1]. Even more, an elastic net regularization, which is a linear combination of the L_1 and L_2 norms, can be employed [132].

6 LET and LFE of Glass Laminate Aluminum Reinforced Epoxy (GLARE)

6.1 Introduction

Glass laminate aluminum reinforced epoxy (GLARE) is of rapidly growing interest in the transport industry, especially in aerospace. This composite has been developed at the Delft University of Technology starting in the 1980s [116]. It consists of alternating thin aluminum alloy sheets bonded together with glass-fiber reinforced epoxy resin [124]. This material, which forms the intermediate layers and is a composite itself, is called prepreg. The name originates from the pre-impregnated fibers in an epoxy resin matrix. GLARE can be classified according to the fiber orientation in the prepreg as unidirectional or cross-ply. In order to manufacture cross-ply prepreg, two or more prepreg sheets with unidirectional orientated fibers are arranged and bonded twisted towards each other. GLARE components differ in the lay-up, i.e., in the number of metal and prepreg sheets. Typical are 3/2, 4/3, and 5/4 lay-ups. Nominal thicknesses for the aluminum alloy and prepregs vary in the range of 0.2 mm to 0.5 mm. The thicker the material, the higher is its strength.

It is the objective of this chapter to demonstrate the flaw detectability of Lorentz force eddy current testing (LET) and Lorentz force evaluation (LFE) (LET&LFE) for the aluminum alloy layers in the GLARE material. One GLARE test object that contains an artificial predefined defect is applied for this purpose. The test object is manufactured by the company Premium Aerotec in Nordenham, Germany, a supplier of the leading aircraft manufacturer Airbus.

On the basis of experimental LET studies of the GLARE specimens, a further aim is to evaluate the performance of an advanced permanent magnet system, the cylindrical Halbach structure [123]. Based on numerical simulations it has been shown that the cylindrical Halbach structure has compared to a cylindrical permanent magnet a superior performance in detecting small subsurface defects. For assessing the performance of the cylindrical Halbach structure based on measured data, Lorentz force signals measured with the cylindrical Halbach magnet are compared to Lorentz force signals measured with a cylindrical permanent magnet.

Moreover, a goal function scan is performed in order to reconstruct the defect. Similar to the approach in Chapter 4, the goal function value is the normalized root mean square error (NRMSE) between the forward calculated and measured Lorentz force signals. The goal function scan is performed for Lorentz force signals measured with the cylindrical Halbach structure. The forward solution including the extended area approach (EAA)

described in Section 2.4.1 is used for the force calculations. A finite element model (FEM) is used to calculate the magnetic flux density because of two reasons. First, no analytic solution exists. Second, the cylindrical Halbach structure contains components with a nonlinear $B(H)$ curve, that cannot be modeled with the magnetic dipoles model.

For comparison purposes, further nondestructive testing (NDT) of the GLARE test object is performed by applying two imaging techniques. These are radiographic and through-transmission ultrasonic testing.

In the following Section 6.2, the experimental setup for GLARE measurements is outlined. Evaluation methods for the measured data are addressed. Also, the forward calculations including the FEM of the cylindrical Halbach structure are explained. Thereafter, the setup for the goal function scan is outlined. Moreover, the applied imaging techniques are explained. Thereafter, the results are outlined in Section 6.3. The Lorentz force data measured with the cylindrical Halbach structure and the cylindrical permanent magnet are compared. Further, the results of the goal function scan are evaluated and compared to the results of the imaging testing techniques. Finally, the findings are discussed in Section 6.4.

6.2 Methodology

6.2.1 Measurements

Figure 6.1 depicts the setup for LET measurements of the GLARE test object. GLARE with 5/4 lay-up is used, i.e., the composite is composed of five layers of aluminum alloy and four intermediate layers of prepreg. The thickness of the metal and the prepreg layers equals $\Delta z = 0.4$ mm and $\Delta z = 0.25$ mm, respectively. The electrical conductivity of the aluminum alloy 3.1354 used for GLARE equals $\sigma_0 = 17$ MS [74].

The test specimen contains one long defect with the nominal dimensions $d_x \times d_y \times \Delta z = 10$ mm $\times$ 1 mm $\times$ 0.4 mm. The defect is positioned in the second aluminum alloy layer, i.e., at the depth $d = 0.65$ mm.

The applied magnet systems are a cylindrical Halbach structure and a cylindrical permanent magnet, both positioned at the liftoff distance $\delta z = 1$ mm. The cylindrical Halbach structure is composed of 12 outer segments, one inner cylindrical magnet and one cylinder of iron-cobalt alloy, which is a soft magnetic material with a high saturation magnetization. (Figure 6.1(c)). The Halbach structure is characterized by the inner and outer radius, $R_{p,i} = 2.7$ mm and $R_{p,o} = 12.4$ mm, the total height $H_p = 14.5$ mm, as well as the height of the iron-cobalt alloy cylinder $H_{IC} = 7.9$ mm. The outer segments have a subtendend angle of 30° and are radially magnetized with a nominal magnetic remanence of $B_r = 1.44$ T. The inner cylindrical magnet, which is axially magnetized with the same nominal remanence, is situated above the iron-cobalt cylinder. The cylindrical permanent magnet has the parameters $R_p = 11.3$ mm and $H_p = 17.6$ mm. It is magnetized in z-direction with a nominal magnetic remanence of $B_r = 1.44$ T. The dimensions of both magnet systems are the result of an optimization procedure performed by the authors in [123]. The objective of this study was to determine optimal magnet geometries for LET that maximize the absolute
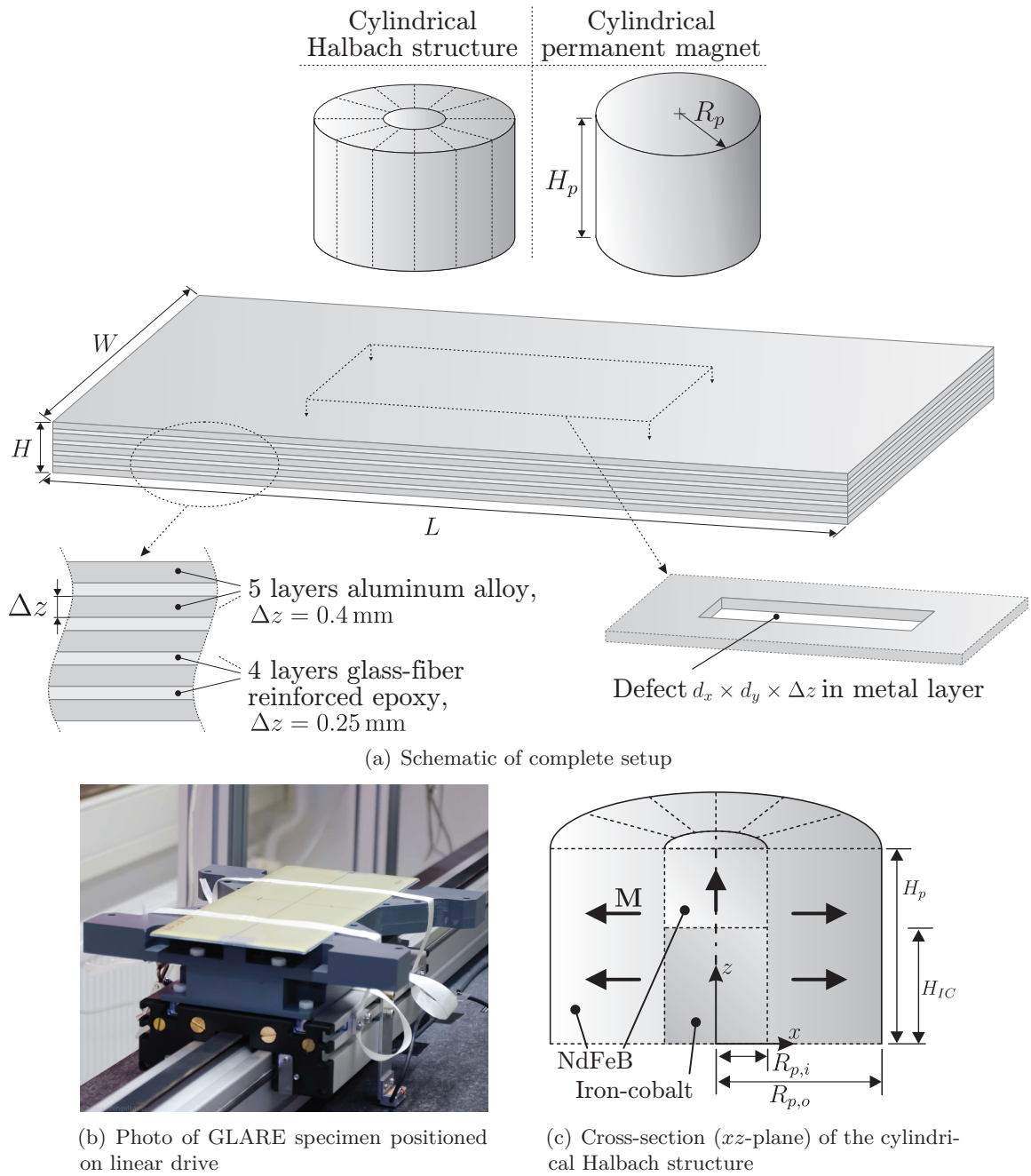
Cylindrical
Halbach structure

Cylindrical
permanent magnet

(a) Schematic of complete setup

5 layers aluminum alloy,
$\Delta z = 0.4\,\mathrm{mm}$

4 layers glass-fiber
reinforced epoxy,
$\Delta z = 0.25\,\mathrm{mm}$

Defect $d_x \times d_y \times \Delta z$ in metal layer

(b) Photo of GLARE specimen positioned
on linear drive

(c) Cross-section (xz-plane) of the cylindri-
cal Halbach structure

Figure 6.1: Experimental setup of LET for the GLARE test specimen. The specimen has
a 5/4 lay-up and contains a single defect with dimensions $10\,\mathrm{mm} \times 1\,\mathrm{mm} \times 0.4\,\mathrm{mm}$ po-
sitioned in the second aluminum alloy layer. Two different magnet systems are applied:
a cylindrical Halbach structure ($R_{p,i} = 2.7\,\mathrm{mm}$, $R_{p,o} = 12.4\,\mathrm{mm}$, $H_p = 14.5\,\mathrm{mm}$, $H_{IC} =$
$7.9\,\mathrm{mm}$) and a cylindrical permanent magnet ($R_p = 11.3\,\mathrm{mm}$, $H_p = 17.6\,\mathrm{mm}$).

amplitude of the defect response signal (DRS).

Figure 6.2 compares the magnetic flux densities of the applied magnet systems using filled
contour plots. The magnetic flux density of the Halbach structure is calculated using FEM,
whereas the analytic current model explained in Section 3.2.2 is applied for the cylindrical
permanent magnet. The flux densities are shown in the xy-plane at $z = -0.85\,\mathrm{mm}$. This

corresponds to the mid-plane of the second aluminum alloy sheet of the GLARE specimen, in which the defect is positioned. The contour lines for the Halbach structure are significantly denser than for the cylindrical permanent magnet. Thus, the magnetic flux density provided by the cylindrical Halbach structure is more focused and concentrated compared to those of the cylindrical permanent magnet. Further, the maximum absolute amplitude is larger, if the Halbach structure is applied. The values for the B_x-component are approximately 0.5 T and 0.35 T for the Halbach structure and cylindrical permanent magnet, respectively. For the B_z-component, the values are approximately 1 T and 0.45 T.
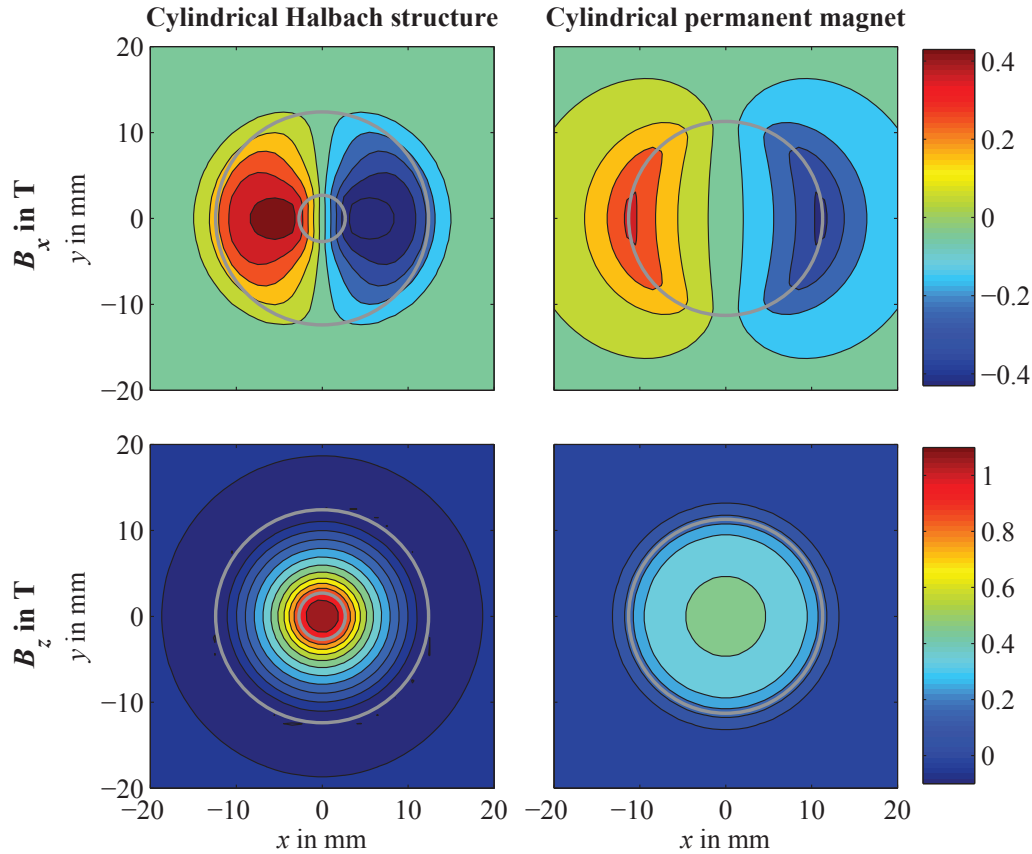
Figure 6.2: Magnetic flux densities produced by the cylindrical Halbach structure (left column) and the cylindrical permanent magnet (right column). The components of the magnetic flux density B_x- and B_z are shown in the upper and lower row, respectively. They are constant along each contour line. The contour lines are drawn at increments of 0.1 T. The gray shaded circles indicate the dimensions of the magnet system.

Two sets of Lorentz force data are measured. The data range consist of 17 y-lines that are equidistantly distributed in the region $-8\,\mathrm{mm} \leqslant y \leqslant 8\,\mathrm{mm}$ and span the range $-30\,\mathrm{mm} \leqslant x \leqslant 30\,\mathrm{mm}$. The sampling frequency is set to 500 sps. The procedure explained in Section 4.2.3 is applied for data preprocessing. The cutoff frequency of the low pass filter is set to 100 Hz for all data sets, because defect perturbations resulting from the cylindrical Halbach system have an increased frequency range than those resulting from the cylindrical magnet.

The performance of the cylindrical Halbach structure and of the cylindrical permanent magnet is compared based on two values. In accordance with [123] the first measure is the percentage increase of the maximum of the absolute ΔF_x-component, $\max |\Delta F_x|$, for the Halbach structure compared to the cylindrical magnet.

The signal-plus-noise-and-distortion-to-noise ratio (SINAD) of the measured and preprocessed data is used as the second measure. The SINAD is an extension of the well-known signal-to-noise ratio (SNR). It is used in practical applications such as LET where the signal component without noise cannot be measured and the signal is influenced by uncorrelated noise and deterministic disturbances [97]. The SINAD is defined as

$$\text{SINAD} = 10 \cdot \log_{10} \frac{P_{\text{snd}}}{P_{\text{nd}}}, \tag{6.1}$$

where P_{snd} denotes the power of the signal of interest, i.e., the DRS, together with noise and distortions, and P_{nd} is the power of the noise and distortions. If P_{nd} is much smaller than P_{snd}, then the SINAD converges to the SNR. In order to determine the range in which the DRS occurs, the x-coordinates at which the maximum and minimum in the F_z-component at the symmetry line $y = 0$ are located are calculated. Then, the starting point of the range containing the DRS is defined by subtracting half of the difference between the x-coordinates at which the extreme values are located from the x-coordinate assigned with the maximum value. Similarly, the sum of the x-coordinates assigned with the minimum and half of the difference range determines the end point.

6.2.2 Forward and Inverse Calculations

In the first part of this section, the forward solution including the FEM for the cylindrical Halbach structure are explained. Thereafter, the setup of the goal function scanning method for defect reconstructions is outlined.

The approximate forward solution including the EAA is used for forward calculations, because the first approximation of the forward solution has a large error for cuboidal shaped defects as present in the GLARE specimen (Section 2.4.1). In the extended forward solution the defect response eddy current distribution (DRCD) flowing in the region composed of the defect region and the region surrounding the defect is represented by a set of regularly distributed current dipoles, the source space. The moments of the current dipoles in the defect region are calculated using the first forward approximation, whereas outside the defect the dipole moments are calculated by using the current dipoles in the defect region as current sources.

The use of a FEM to calculate the magnetic field implies a numerical calculation of the electric potential φ in the conductor. For this purpose, the definite integral to calculate φ at the position $\mathbf{p} = [x_k, y_k, z]^{\mathsf{T}}$ in the source space, with $k = 1 \ldots N_S$ denoting the number of grid points (current dipoles in the source space), is approximated using the Simpson's

rule [101] as

$$
\varphi\left(x_k, y_k, z\right) = \int\limits_{-\infty}^{z} B_y(x_k, y_k, z) dz
$$

$$
\approx v \frac{z_{N_\infty} - z_0}{6 N_\infty} \left[B_y(x_k, y_k, z_0) + 2 \sum_{n=1}^{N_\infty - 1} B_y(x_k, y_k, z_{2n}) \right.
$$

$$
\left. + 4 \sum_{n=0}^{N_\infty - 1} B_y(x_k, y_k, z_{2n+1}) + B_y(x_k, y_k, z_{N_\infty}) \right] + \mathcal{O}\left(\Delta z^4\right).
$$

(6.2)

The last term $\mathcal{O}\left(\Delta z^4\right)$ is the truncation error. The scalar N_∞ is an even number of grid points in the integration domain $\mathbf{L}_k = \{[x_k, y_k, z_n] \, z_n = (n-1)\Delta z, n = 0 \ldots N_\infty\}$, with Δz denoting the distance between two integration points (Figure 6.3). The values N_∞ and Δz should be selected in such a way that their product is large enough to ensure a low approximation error.
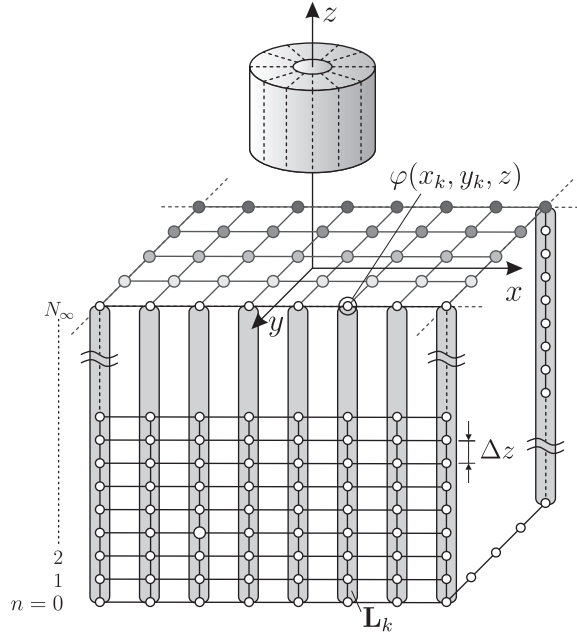
Figure 6.3: Integration domain to calculate the electric potential φ in the conductor.

In order to obtain the components of the current dipoles in the DRCD in the source space (equation (2.3)), the gradient of φ is approximated by the difference quotient calculated on the regular dipole grid. For interior points the central difference quotient is applied, whereas for edge dipoles the single-sided difference quotient is used.

In this study, the DRCD for both magnet systems is modeled with a regular grid of $N_S = 6400$ current dipoles equidistantly distributed in the range $-10\,\mathrm{mm} \leqslant x \leqslant 10\,\mathrm{mm}$ and $-10\,\mathrm{mm} \leqslant x \leqslant 10\,\mathrm{mm}$ with $\Delta x = \Delta y = 0.25\,\mathrm{mm}$.

The parameters for the numerical integration are set to $N_\infty = 150$ and $\Delta z = 0.5\,\mathrm{mm}$. Lorentz force signals are calculated for a grid of measurement points having the same

positions as the measured Lorentz force signals.

For inverse calculations, the goal function scanning method is applied. In this method, the landscape of the goal function is investigated for a set of grid points uniformly distributed in the search space. Similar as in the previous chapters, the goal function is defined as the NRMSE between forward calculated and measured data (equation (4.6)). The forward procedure described beforehand is applied for forward calculations. Since the goal function scanning method is limited to one defect, it is evident to use the geometry parameters of the defect as design variables. The location of the defect, i.e., the x- and y-coordinate of the center of gravity, can be determined straightforwardly. The defect location is assigned to the position at which the ΔF_x-component of the DRS has the largest absolute amplitude. Thus, the depth and the x- and y-extension of the defect remain to be determined. The goal function is evaluated for all combinations of the x-extension $d_x = \{5\!:\!0.5\!:\!15\}$ mm, the y-extension $d_y = \{0.5\!:\!0.5\!:\!5\}$ mm, and the defect depth $d = -\{0, 0.65, 1.3, 1.95, 2.6\}$ mm.

6.2.3 Nondestructive Testing of GLARE using Imaging Techniques

For comparison purposes, the NDT techniques radiographic and through-transmission ultrasonic testing are applied to detect the defect in the GLARE specimen. In the radiographic testing, the used X-ray generator is operating with 15 kV and a current flow of 35 µA. The ultrasonic testing is performed by the company Premium Aerotec, which has manufactured the GLARE test object. An automatic scanning system using water-coupling of the ultrasonic waves with the squirter technique is applied [49]. The used probes work with a frequency of 5 MHz. The resolution of the method equals 1 mm in either direction. Both methods scan the GLARE specimen in z-direction, i.e., perform projections on its xy-plane. A scanning in x- and y-direction is due to the setup and specifications of the NDT testing systems not possible. The x- and y-extension of the GLARE specimen are too large in order to position the specimen accordingly. Further, neither the used X-rays nor the ultrasonic waves are able to penetrate the specimen in x- and y-direction.

6.3 Results

6.3.1 Experimental Verification

Figure 6.4 shows the DRS measured from the GLARE specimen containing a defect in the second aluminum alloy layer. The DRS obtained with the cylindrical Halbach structure is compared to the DRS obtained with the cylindrical permanent magnet. The DRS of the Halbach structure has a significantly larger absolute amplitude than that of the cylindrical permanent magnet. In particular, defect perturbations in the ΔF_y-component are hardly to be distinguished from noise and interfering signals, if the cylindrical permanent magnet is used. Contrary, they are distinctly visible if the cylindrical Halbach structure is applied. Further, the slopes in the DRS are steeper if the Halbach structure is applied. Thus, the area spanned by the DRS is in either coordinate direction smaller than for the cylindrical permanent magnet.

(a) Cylindrical Halbach structure

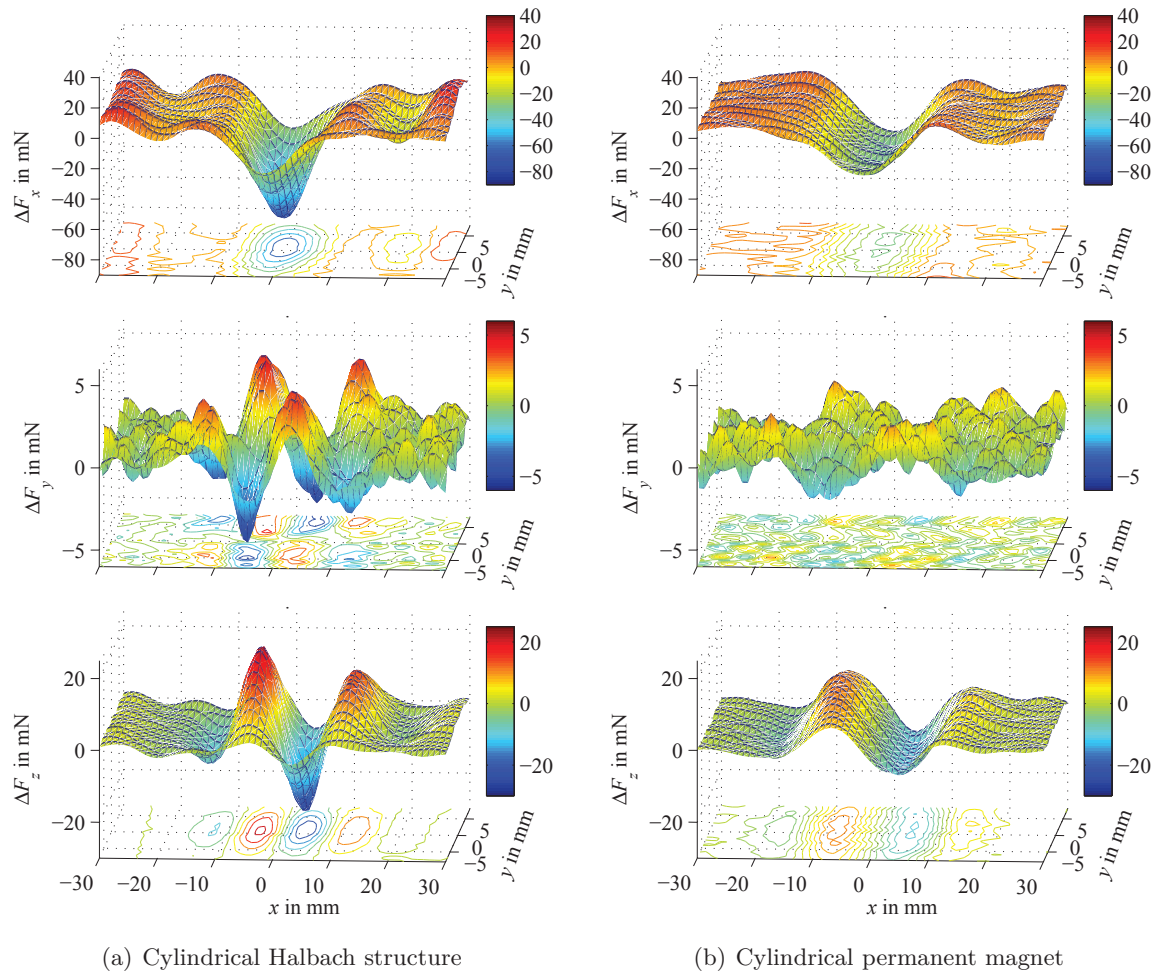(b) Cylindrical permanent magnet

Figure 6.4: Measured and preprocessed DRS obtained from the GLARE specimen. LET experiments are performed twice using different magnet systems: the cylindrical Halbach structure and a cylindrical permanent magnet. The defect is positioned in the second aluminum alloy layer, i.e., at $d = 0.65$ mm.

The percentage increase of the maximum of the absolute ΔF_x-component for Halbach structure compared to the cylindrical magnet equals 116 %. The calculated SINAD values for both magnet systems are shown in Table 6.1. The SINAD values of the ΔF_x- and ΔF_z-component are similar. However, the values of the ΔF_y-component are significantly higher, if the cylindrical Halbach structure is applied.

Table 6.1: SINAD values in dB of measured DRSs obtained from the GLARE composite. The defect is positioned in the second aluminum alloy layer.

Applied PM	Halbach PM			Cylindrical PM		
DRS component	ΔF_x	ΔF_y	ΔF_z	ΔF_x	ΔF_y	ΔF_z
SINAD in dB	13.9	5.5	7	13.5	0.9	7.6

6.3.2 Forward Calculations and Goal Function Scan

Figure 6.5 compares the ΔF_x- and ΔF_z-component of the forward calculated DRS to the measured data at the symmetry line $y = 0$. Note that the ΔF_y-component vanishes theoretically at the symmetry line. The forward calculated DRS has a smaller absolute amplitude than the measured data. The corresponding NRMSE of the ΔF_x- and ΔF_z-component equals 8.94 % and 8.18 %, respectively.
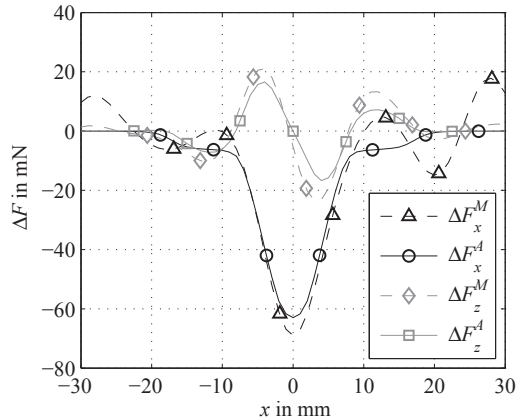
Figure 6.5: Comparison of DRSs obtained from measured data (ΔF^M) and forward calculated Lorentz force signals using the EAA (ΔF^A). The defect is positioned in the second aluminum alloy layer. The cylindrical Halbach structure is applied.

Figure 6.6 shows the landscape of the goal function using contour plots. The results are shown in groups, where each group refers to one of the five aluminum alloy layers of the GLARE specimen. The global minimum of the goal function is in the third metal layer and has a value of 5.26 %. This does not correspond to the correct defect depth, i.e., the second metal layer. The defect extensions assigned with the global minimum are $\{d_x, d_y\} = \{10.5, 5\}$ mm. Thus, the y-extension is significantly higher. Considering the course of the contour lines it cannot be excluded that the global minimum lies at other parameter combinations, if the assessed parameter range is extended.

Moreover, the results show that one local minimum exists in each single aluminum alloy layer. Thus, if the optimization function is considered separately for each layer, it is convex. The minimum NRMSE in the layer corresponding to the correct defective second layer equals 5.34 %. The corresponding defect extensions are $\{d_x, d_y\} = \{9.5, 2.5\}$ mm. It can be observed that with increasing depth of the metal layer the defect extensions corresponding to the local minima in the single layers increase. Further, the goal function is relatively flat and the minima are not distinct. All minima, global and local, differ from each other by less than 1.4 %. Additionally, the CPU time required for the goal function scan is approximately two days (Dual CPU Intel® Xeon® E5-2687Wv3, 3.1 GHz, 128 GB RAM, 64-bit Gentoo Linux, MATLAB® R2015a). The significant increase in comparison to the inverse calculations in Chapters 4 and 5 results from the use of the EAA for forward calculations.

Figure 6.6: Landscape of the goal function for the GLARE specimen. The goal function value is the NRMSE between measured and forward calculated Lorentz force signals. Error values are shown using contour plots separately for each aluminum alloy layer. The bold "L" indicates the number of the layer counted from the top of the specimen. The numbers associated with the contour lines show the NRMSE in %. The black cross and the corresponding value in bold face marks the minimum NRMSE of the respective layer. The gray dashed lines show the nominal defect extensions, $d_y = 1\,\text{mm}$ and $d_x = 10\,\text{mm}$.
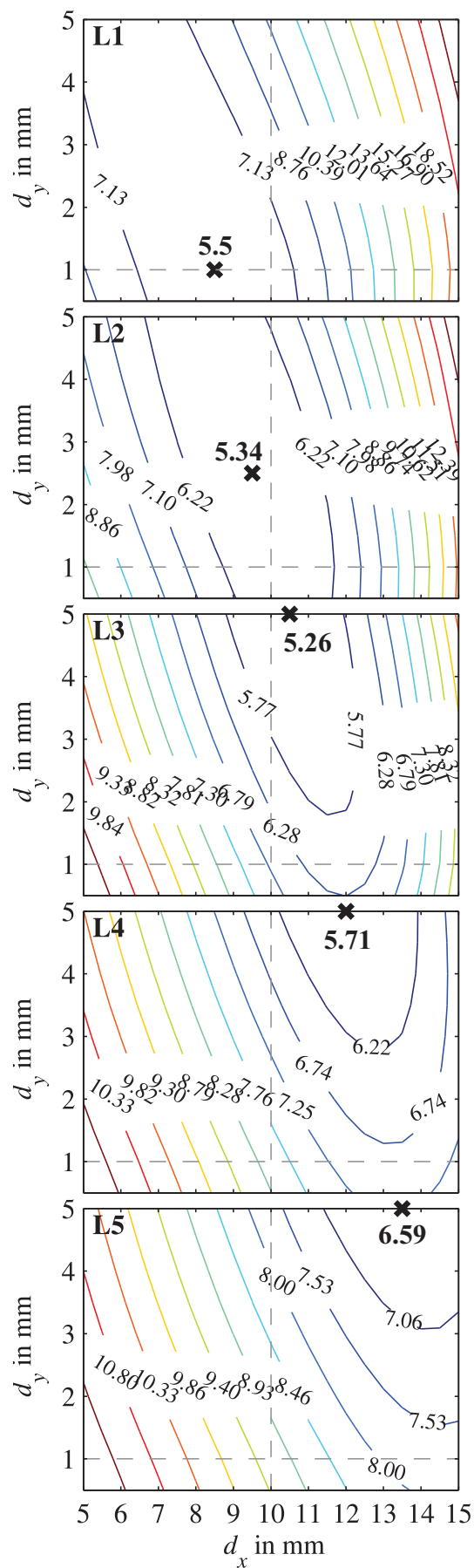
6.3.3 Comparison of the Imaging Techniques and LFE

Figure 6.7 shows the resulting images obtained from radiographic and through-transmission ultrasonic testing. It can be observed that the resolution of the radiography is superior than the resolution of the ultrasonic testing. In the radiographic image, the cutting edge in x-direction is clearly visible. The boundary of the defect in y-direction is blurred. This might result from the fact that it is challenging to manufacture clean cuts with a length of $1\,\text{mm}$. In the ultrasonic results, the yellow colored region represents the defect.

(a) Radiographic testing

(b) Through-transmission ultrasonic testing (figure provided by the company Premium Aerotec)
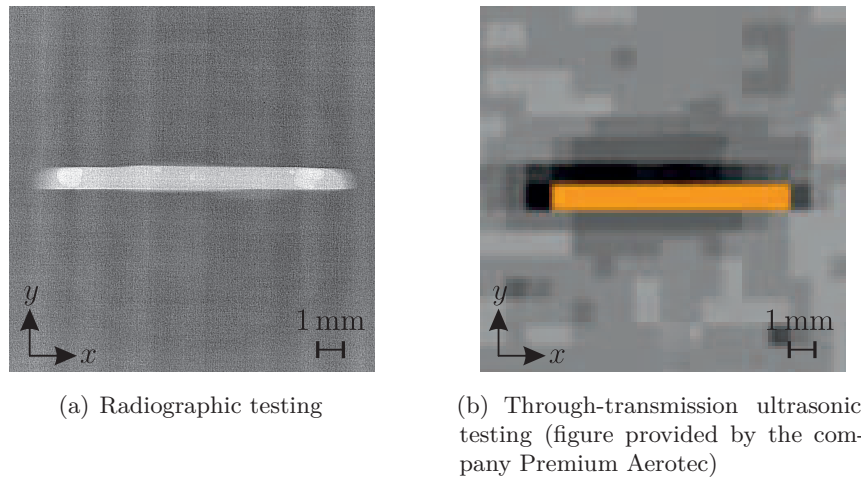
Figure 6.7: Results of radiographic and ultrasonic testing of the GLARE specimen. Projections are performed on the xy-plane of the specimen.

Table 6.2 depicts the defect parameters estimated from the images in Figure 6.7, and compares them to the results of LFE, i.e., the defect parameters assigned to the global minimum in the goal function (Section 6.3.2). Considering, the x-extension the radiography provides a slightly larger estimate than the nominal value. Contrary, with ultrasonic testing the x-extension is estimated smaller. The results of the goal function scan in LFE are comparable to those of the radiographic testing. In case of the y-extension, the imaging techniques provide accurate results and outperform the LFE method. However, a depth estimation is not possible with either imaging technique. Only LFE allows to perform a

Table 6.2: Comparison of the results obtained from the radiographic testing, the ultrasonic testing, and the goal function scan in LFE. The NDT methods are applied to estimate the parameters of the defect in the GLARE material. The nominal defect parameters equal $d_x = 10\,\text{mm}$ (x-extension), $d_y = 1\,\text{mm}$ (y-extension), and $d = 0.65\,\text{mm}$ (depth).

	Radiography	Ultrasonics	LET&LFE
d_x in mm	10.6	8.3	10.5
d_y in mm	0.9	1	5
d in mm	-	-	1.3

depth estimation.

6.4 Discussion

In this chapter, LET was applied to detect defects in an aluminum alloy layer of GLARE material. GLARE is nowadays the leading composite material in the aircraft industry. The artificial defect in the object under test can be clearly identified in the measured Lorentz force signals shown in Figure 6.4. Thus, the defect detectability of LET for GLARE was proved. The high SINAD values in Table 6.1 indicate that LET is likely to be able to identify even smaller internal defects than the one evaluated.

The performance of a cylindrical Halbach structure was compared to that of a cylindrical permanent magnet. Figure 6.4 shows that the area spanned by the DRS is smaller if the cylindrical Halbach structure is applied instead of the cylindrical permanent magnet. Further, the absolute amplitude of the DRS is larger. The improvement in the absolute amplitude of the ΔF_x-component of the DRS signal equals 116 % (Section 6.3.1). This is in very good agreement with the findings in [123]. Both aspects are the consequence of the magnetic flux density distributions shown in Figure 6.2. The magnetic flux distribution of the Halbach structure is more concentrated underneath the magnet and has a larger amplitude than the flux distribution of the cylindrical permanent magnet. The discussed findings prove that the cylindrical Halbach structure has compared to the cylindrical permanent magnet a superior performance in detecting small subsurface defects.

Further, a comparison between the SINAD values for the Halbach and the cylindrical magnet in Table 6.1 shows that the SINAD values for the ΔF_x- and ΔF_z-component are similar. The ΔF_y-component has a significant higher value if the cylindrical Halbach structure is applied. This indicates that the absolute amplitude of the distortions and noise in the ΔF_x- and ΔF_z-component is higher if the Halbach structure is applied. In consideration of the SINAD values the superior performance of the cylindrical Halbach structure can be confirmed only for the ΔF_y-component.

The evaluation of the goal function in Figure 6.6 shows that the reconstruction of the x-extension of the defect has a very small error. However, the reconstruction error in y-direction is large. In the previous Chapters 4 and 5 the y-extension of the defect has also been reconstructed too large. The reasons might be that the resolution of LET in y-direction is worse than in x-direction, and that the y-extension of the sensor space is not large enough.

The aluminum alloy layer assigned to the global minimum of the goal function is positioned directly below the layer in which the defect is positioned. Thus, the error in the depth reconstruction equals 0.65 mm. However, this error can be considered as very small, because the aluminum alloy layers of GLARE are really thin compared to the layers of the composites evaluated in the Chapters 4 and 5. This aspect also explains why the local minima of the goal function (one local minimum in each layer) lie in the range of only 1.4 %.

Instead of the goal function scanning method, the Differential Evolution (DE) optimization algorithm introduced in Chapter 4 can be applied to minimize the goal function. It is to be expected that the DE optimization converges to the global minimum of the goal function. Thus, similar as the DE strategy the goal function scanning method outperforms the current density reconstructions, which are applied in Chapter 5.

In future studies, it is the aim to enhance the experimental setup in such a way as to reduce the interfering signals and noise in the measured data (Figure 6.4(a)). As a consequence, it can be expected that the reconstruction results of the goal function scanning method will be improved.

7 Concluding Remarks

7.1 Summary and Discussion

The objective of this thesis was the development and evaluation of forward and inverse calculation methods in Lorentz force evaluation (LFE). The evaluation technique LFE was applied to reconstruct conductivity anomalies, which occur in the metal layers of laminated composites. The inverse calculations in LFE are based on Lorentz force signals that are measured using the nondestructive testing method Lorentz force eddy current testing (LET). Inverse calculations require a forward solution for the Lorentz force signals, which incorporates a model of the components used in the LET setup.

The working principle of LET is based on a relative movement between a permanent magnet and an electrically conducting material under test. Due to the relative movement eddy currents are induced in the conductor. The eddy currents interact in turn with the magnetic field. This interaction results into a Lorentz force exerted on the conductor and in opposite direction also on the permanent magnet, where it is measured. Material deficiencies cause perturbations in the Lorentz force signals. Inverse calculations evaluate the information that are present in the perturbations.

In this thesis, the magnetic dipoles model (MDM) was developed in order to represent the permanent magnet in the forward solution for LFE. In the MDM, the permanent magnet is replaced by a regular distributed assembly of magnetic dipoles. Compared to analytic solutions the MDM has the advantage that it can be applied to permanent magnets of arbitrary geometry. Moreover, it allows to calculate the magnetic field in the near field of the permanent magnet with high accuracy. This is not possible by using a single magnetic dipole except for spherical permanent magnets. Further, the use of the MDM maintains the advantage to calculate the Lorentz force signals solely with elementary analytic mathematics.

An optimization procedure was developed to obtain optimal magnetic dipole positions in the MDM. It was shown that the optimization procedure provides a significant improvement especially if a low number of magnetic dipoles is used. In this thesis, the MDM was applied to a cuboidal and a cylindrical permanent magnet. Analytic solutions of the magnetic field served as a reference solution to evaluate the accuracy of the MDM. The results showed that the investigated cuboidal permanent magnet can be accurately modeled with a MDM consisting of 832 magnetic dipoles. The remaining error equals 0.02 %. The same accuracy can be achieved for the cylindrical permanent magnet, if 1890 magnetic dipoles are used in the MDM. Apart from forward and inverse calculations in LFE, the MDM can be used in

other applications, in which precise simulations of permanent magnets are required. These include eddy current brakes, electrical machines, and electromagnetic damping.

In this thesis, three inverse calculation methods were introduced for defect reconstruction in LFE. First, a stochastic optimization algorithm, the Differential Evolution (DE), was applied to perform conductivity reconstructions. Thereby, a region in the conductor, in which the defect was assumed to be present, was discretized by a regular grid of elementary volume elements with unknown conductivities. The aim of the optimization procedure was to determine the conductivities. The intrinsic control parameters of the DE were selected prior to inverse calculations. Parameter studies were performed for this purpose. In each iteration the continuous-valued optimization variables employed in the DE were binarized. Further, an area opening procedure was applied to the inverse solutions. Both operations accelerate the convergence of the optimization.

Second, current density reconstructions (CDR) using minimum norm estimates (MNE) were applied for flaw reconstructions. This approach is based on the fact that the defect can be interpreted as an extended current source in the forward solution for LFE. For CDR a regular grid of current dipoles was defined in the conductor. The current dipoles represent the eddy current distribution in the conductor. In the inverse method, the moments of the current dipoles were determined. Thereby, a current density averaged over all measurement points was assessed.

These two inverse calculation strategies were validated based on measured Lorentz force signals. A sandwich-structured composite named Alucobond was investigated. The results showed that the geometry of the defect, i.e., the location and size, can be well reconstructed with either approach. Thereby, the findings of the DE optimization strategy had a slightly higher accuracy for the defect location than the CDR. Contrary, the defect size was slightly better approximated with the CDR. Further, the depth of the defect was correctly determined by the Differential Evolution reconstruction scheme. Contrary, the CDR did not yield correct depth reconstruction.

Another aspect to verify the reconstruction quality is to compare the final objective function value, i.e., the normalized root mean square error (NRMSE), of the Differential Evolution strategy (Figure 4.7), to the unexplained variance of the CDR (Figure 5.7). Both parameters are a measure for the goodness of fit of the inverse solution. The NRMSEs of values less than $10\,\%$ indicate a more accurate inverse calculation than unexplained variances of approximately $50\,\%$. In summary, the Differential Evolution strategy provides more accurate defect approximations than the CDR. Therefore, we suggest the application of the Differential Evolution reconstruction strategy to other electromagnetic nondestructive testing and evaluation (NDT&E) techniques.

The third inverse method applied in this thesis was the goal function scan. This method was applied to Lorentz force signals that were measured using a glass laminate aluminum reinforced epoxy (GLARE) specimen. GLARE is nowadays increasingly used in the aircraft industry, because it has outstanding fatigue characteristics. The geometry parameters extension and depth were defined as the unknown variables. The differences of the defect

parameters assigned with the global minimum in the goal function and the correct defect parameters are in an acceptable range. Similar to the DE strategy, the goal function scanning method outperforms the CDR.

All in all, the application and evaluation of LET and LFE for the Alucobond and the GLARE material contribute to the ongoing development of reliable NDT&E methods to enhance the quality assurance for laminated composite materials in industrial applications.

7.2 Outlook

Apart from the inverse methods introduced in this thesis, there are still a variety of methods that can be analyzed. In the framework of topology optimization, level-set methods can be employed. These methods allow to model curved surfaces that propagate in time. The idea is to represent the surface of interest at any time in terms of a level-set function. By changing the level-set function and thus the surface using a speed function, the surface can be optimized. Level-set methods allow the surface in question to split and merge during evolution. This is not possible with methods that parametrize the surface boundaries. Level-set methods have already been applied in a wide variety of fields such as fluid mechanics, computer-aided design, and image segmentation [103]. Further, they have been used for shape optimization of electromagnetic devices [47] and for material reconstruction in nondestructive testing [23].

Furthermore, a deconvolution approach can be applied. This method is based on the aspect that the LET system meets the requirements of a linear time-invariant system, as long as only one defect is present in the material. Then, the measured Lorentz force in each scanning line can be modeled as the convolution of a function describing the conductivity of the material of the conductor along the scanning line and the impulse response of the system. The impulse response can be easily obtained as the derivative of the step function of the system, i.e., the measured Lorentz force at the edge of the conductor. The aim is to solve for the unknown conductivity distribution.

In the framework of introducing new inverse methods it is the objective to investigate material deficiencies of arbitrary shape, e.g., curvilinear anomalies. This includes corrosion or shallow cracks. Further, composites with multiple inhomogenities are of interest.

A α-MDM of the Cubic Permanent Magnet

In addition to the cuboidal and cylindrical permanent magnet described in Section 3.3.1, the magnetic dipoles model (MDM) is applied to a magnet of cubic shape. Since the cubic magnet is a special case of a cuboidal magnet, the α-MDM was used. The cubic magnet under investigation has the dimensions $a = H_p = 15\,\mathrm{mm}$, the magnetic remanence $\mu_0 M = 1.17\,\mathrm{T}$, and the liftoff $\delta z = 1\,\mathrm{mm}$. We optimized the α-MDMs specified by all combinations of $N_a = \{2:2:14\}$ and $N_h = \{1:1:25\}$.

Similar to the results of the cuboidal and cylindrical permanent magnet, a minimum $NRMSE^o_{G,\min} = \{2.165, 0.341, 0.094, 0.022, 0.006, 0.003, 0.001\}\,\%$ can be observed for each N_a-group (Figure A.1(a)). The minimum error occurs at the optimal number of layers $N^o_{h,\min} = \{1, 3, 5, 8, 10, 12, 14\}$ in the optimized MDMs. Thus, an increase of N_a yields an increase of $N^o_{h,\min}$. A least squares fit shows that the optimal number of layers depends on N_a as $N^o_{h,\min} = [1.11 \cdot N_a - 1.28]$. Further, for $N_a \geqslant 8$ it is $N_a = N_h$. Thus, the voxels are elementary cubes. This can be reasoned by the fact that the cube shows the smallest error among all cuboid voxels modeled with a single magnetic dipoles [83].

Figure A.1(b) shows that for small numbers of dipoles, α_o is smaller than 0.5. With increasing N_D it increases to a maximum value of 0.5002 for $N_D = 64$ ($N_a = N_h = 8$). For larger N_D, the dipole positions converge to the center of gravity of the voxels.
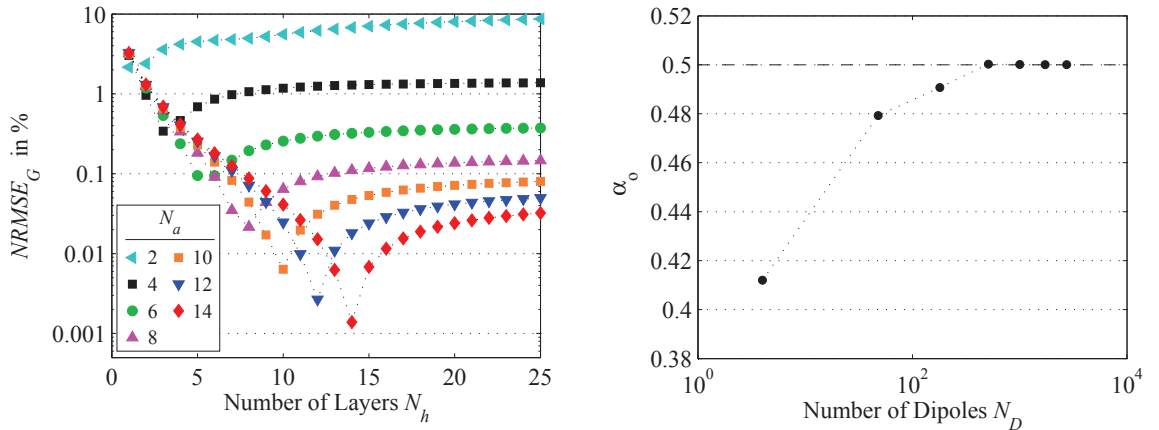
(a) $NRMSE_G$ between the α_o-MDMs and the charge model as a function of N_a and N_h in the α_o-MDM

(b) Optimal parameter α_o depending on N_D of the α_o-MDMs corresponding to the minima in (a). The dashed line at $\alpha_o = 0.5$ indicates the center of gravity of the voxels.

Figure A.1: Results of the optimization of the α-MDM of the cubic permanent magnet.

In Figure A.2 the magnetic flux density components B_x and B_z of two α_o-MDMs and the charge model are compared. The α_o-MDMs are calculated with $N_D = 2^2 \cdot 1 = 4$ and $N_D = 8^2 \cdot 8 = 512$ dipoles. The flux densities are observed at $y = 0$ (symmetry line of the permanent magnet), and $z = -1\,\mathrm{mm}$. If $N_D = 4$, the normalized root mean square error (NRMSE) of the B_x- and B_z-component equals $2.17\,\%$ and $2.05\,\%$, respectively. Differences can be observed in the region below the permanent magnet ($-7.5\,\mathrm{mm} \leqslant x \leqslant 7.5\,\mathrm{mm}$). If $N_D = 512$, the NRMSE decreases to $0.032\,\%$ (B_x) and $0.033\,\%$ (B_z) and no irregularities can be observed.
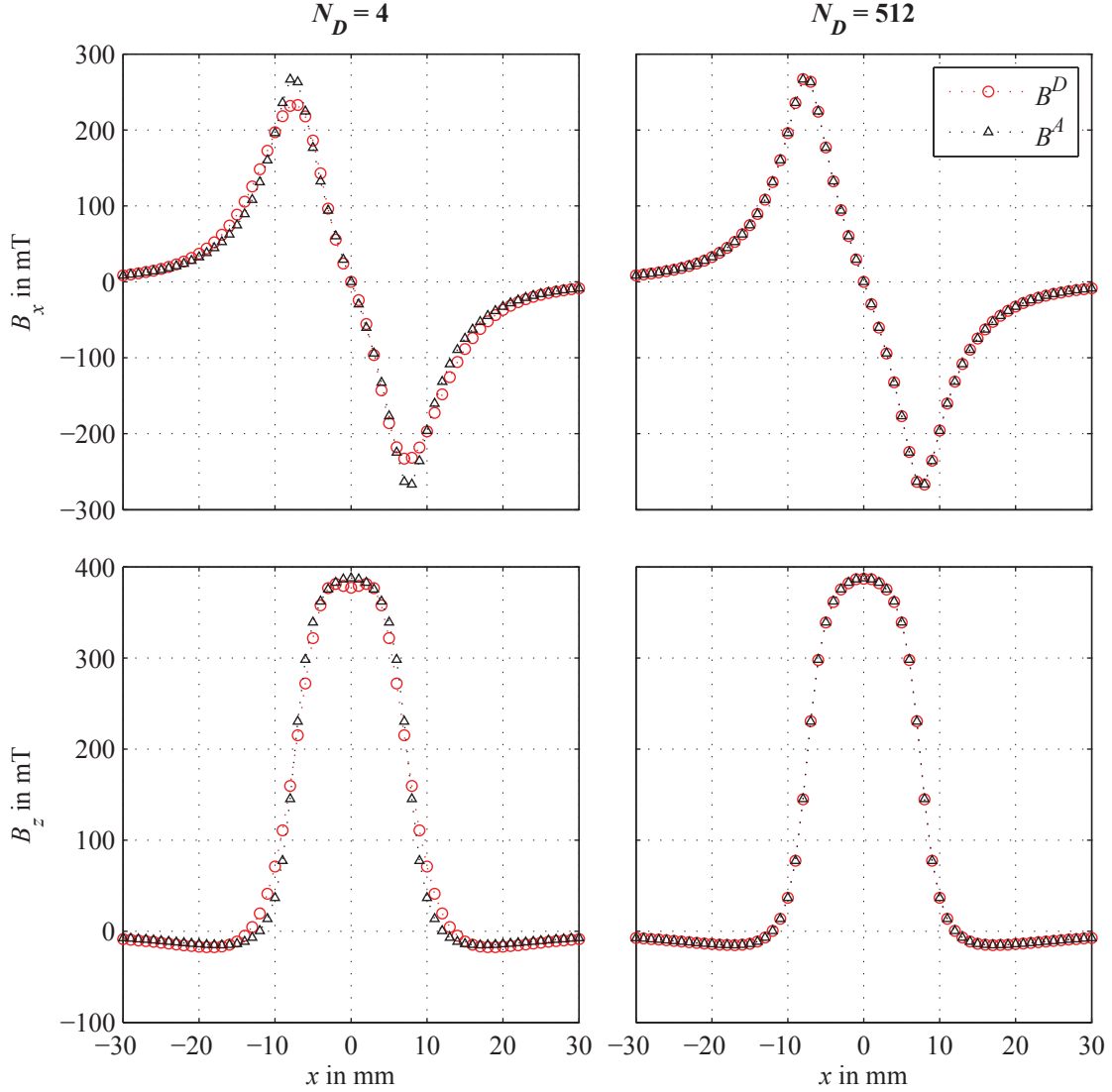
Figure A.2: Comparison of magnetic flux densities obtained from two α_o-MDMs (B_D) and the charge model (B_A) of the cubic permanent magnet. The α_o-MDMs are calculated for $N_D = 2^2 \cdot 1 = 4$ with $\alpha_o = 0.412$ (left column) and $N_D = 8^2 \cdot 8 = 512$ with $\alpha_o = 0.5002$ (right column). The upper and lower row depict the magnetic flux density components B_x and B_z, respectively.

B Validation of the Weak Reaction Approach

In order to justify the applicability of the weak reaction approach for low velocities, the Lorentz force signals calculated by the weak reaction approach are compared to the Lorentz force signals computed by the transient approach. The transient approach considers the electromagnetic field diffusion-convection equation including parts in relative motion, which has to be solved in LET studies, in its full form [129]. Contrary, the weak reaction approach neglects the secondary magnetic field. Since it is not possible to calculate the Lorentz force signals with the transient approach analytically, the finite element method is applied for numerical computations. For comparison purposes the finite element method is also used for the weak reaction approach. In the simulations, the aluminum alloy block has the dimensions $L_c \times W_c \times H_c = 250\,\text{mm} \times 50\,\text{mm} \times 50\,\text{mm}$. The metal sheets have the height $\Delta z = 2\,\text{mm}$ and the conductivity $\sigma_0 = 30.61\,\text{MS}$. The second metal sheets contains an artificial cylindrical defect with the radius $R_d = 2.5\,\text{mm}$ and height $H_d = 2\,\text{mm}$. The applied permanent magnet is of spherical shape with the radius $R_p = 7.5\,\text{mm}$ and the liftoff $\delta z = 1\,\text{mm}$. We compare finite element model (FEM) simulations for two velocities: $v = 0.5\,\text{m/s}$ and $v = 7.5\,\text{m/s}$. For these configurations the magnetic Reynolds number equals $R_\text{m} = \mu_0 \sigma_0 |\mathbf{v}| L = 0.96$ and $R_m = 14.42$, respectively. Thereby, $\mu_0 = 4\pi \cdot 10^{-7}$ is the magnetic permeability in the vacuum and $L = H_c$ is the characteristic length scale.

Figure B.1 compares the resulting Lorentz force components ΔF_x and ΔF_z at the symmetry line ($y = 0$). It can be observed that for $v = 0.5\,\text{m/s}$ the deviations of the transient approach and the weak reaction approach are small. The normalized root mean square error (NRMSE) calculated according to Equation (2.13) is 2.09 %, which can be considered as sufficiently small. If $v = 7.5\,\text{m/s}$, the NRMSE increases to 40.1 %, indicating that the weak reaction approach should not be applied for high velocities.
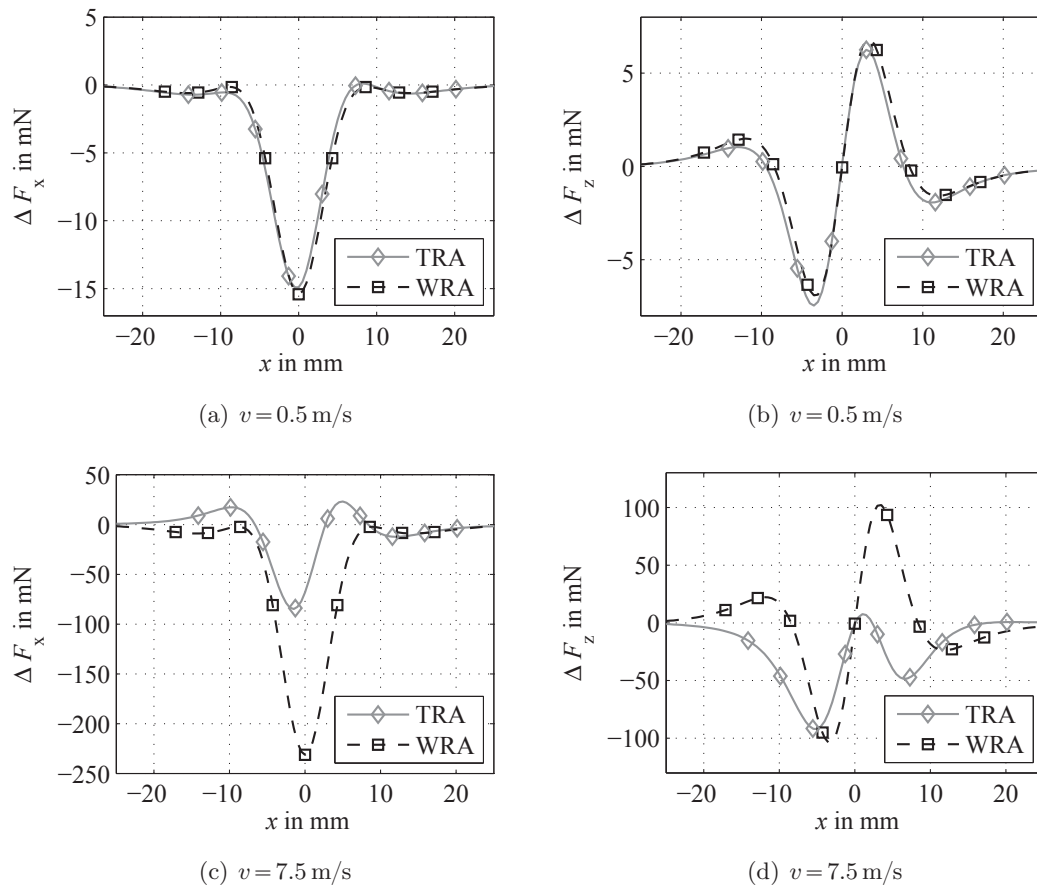
Figure B.1: DRS components ΔF_x and ΔF_z for low and high velocities calculated with FEM using the transient approach (TRA) and the weak reaction approach (WRA). Please note that ΔF_y vanishes at the symmetry line.

List of Figures

List of Tables

Glossary of Acronyms and Symbols

Acronyms

CDR	current density reconstructions
CPU	central processing unit
DE	Differential Evolution
DRCD	defect response eddy current distribution
DRS	defect response signal
EA	evolutionary algorithm
EAA	extended area approach
ECD	eddy current distribution
ECT	eddy current testing
EP	evolutionary programming
ES	evolutionary strategy
FEM	finite element model
GA	genetic algorithm
GLARE	glass laminate aluminum reinforced epoxy
LET	Lorentz force eddy current testing
LFE	Lorentz force evaluation
LFV	Lorentz force velocimetry
MDM	magnetic dipoles model
MFL	magnetic flux leakage
MNE	minimum norm estimates
NDT	nondestructive testing
NDT&E	nondestructive testing and evaluation
NRMSE	normalized root mean square error
SINAD	signal-plus-noise-and-distortion-to-noise ratio
SNR	signal-to-noise ratio
TRA	transient approach
TSVD	truncated singular value decomposition
WRA	weak reaction approach

Symbols

α	parameter to define the z-position of the magnetic dipoles in a magnetic dipoles model
α_o	optimized α
α_s	straightforward dipole positioning, $\alpha_s = 0.5$
β	parameter to define the radial position of the magnetic dipoles in a magnetic dipoles model
β_o	optimized β
β_s	straightforward dipole positioning, $\beta_s = 0.5$
B	magnetic flux density

Glossary of Acronyms and Symbols

B_r	magnetic remanence
d	depth of defect, depth of metal layer
(d_x, d_y)	(x, y)-extension of defect
δz	liftoff distance
$\Delta \mathbf{F}$	defect response signal
$\Delta \mathbf{j}$	defect response eddy current distribution
Δz	height of the defect (metal layer)
E	number of voxels (current dipoles) in extended region
ε_i	normalized root mean square error of the i-th Lorentz force component
(e_x, e_y)	semi-axes of an ellipse
(E_x, E_y)	(x, y)-extension of the extended region
$\mathbf{F}, \mathbf{F}_0$	Lorentz force coming from a specimen with and without a defect
H_c	height of specimen
H_p	height of permanent magnet
$\mathbf{j}$	eddy current density in a defective conductor
$\mathbf{j}_0$	eddy current density in a defect-free conductor
K	number of voxels (current dipoles) in defect region
$\boldsymbol{K}$	gain matrix
L_c	length of specimen
(l_x, l_y)	half of (x, y)-extension of sensor space
l_s	half of (x, y)-extension of quadratic source space
$\mathbf{m}$	moment of magnetic dipole
M	number of measurement points
$\mathbf{M}$	magnetization of permanent magnet
μ_0	magnetic permeability of vacuum
N_D	number of dipoles in magnetic dipoles model
N_h	number of dipole layers in magnetic dipoles model
N_H	number of current loops
N_L	number of metal sheets in laminated composite
N_S	number of voxels (current dipoles) in the source space
N_S^i	number of voxels in the i-th ring in the magnetic dipoles model of the cylindrical permanent magnet
$\mathbf{p}$	moment of current dipole
φ	electric potential
R_m	magnetic Reynolds number
R_p	radius of permanent magnet
σ	conductivity
σ_0	conductivity of metal sheets in laminated composite
σ_d	conductivity of defect
$\boldsymbol{\sigma}$	vector containing voxel conductivities
ϑ	threshold for conductivity reconstruction
$\mathbf{v}$	velocity vector
V	volume of conductor without defect
V_d	volume of defect
V_E	volume of elementary voxel
V_p	volume of permanent magnet
W_c	width of specimen
ξ_D	dipolar correction factor

Bibliography

[1] R. A. Adams and J. J. Fournier, *Sobolev spaces.* Oxford, United Kingdom: Elsevier, 2003. 79

[2] A. Alaknanda, R. Anand, and P. Kumar, "Flaw detection in radiographic weld images using morphological approach," *NDT & E International*, vol. 39, no. 1, pp. 29–33, 2006. 5

[3] F. Bancel, "Magnetic nodes," *Journal of Physics D: Applied Physics*, vol. 32, pp. 2155–2161, 1999. 25

[4] D. Baumgarten, M. Liehr, F. Wiekhorst, U. Steinhoff, P. Münster, P. Miethe, L. Trahms, and J. Haueisen, "Magnetic nanoparticle imaging by means of minimum norm estimates from remanence measurements," *Medical & Biological Engineering & Computing*, vol. 46, no. 12, pp. 1177–1185, 2008. 23

[5] M. Bertero, T. A. Poggio, and V. Torre, "Ill-posed problems in early vision," *Proceedings of the IEEE*, vol. 76, no. 8, pp. 869–, 1988. 20

[6] J. Blitz and G. Simpson, *Ultrasonic methods of nondestructive testing.* London, United Kingdom: Chapman & Hall, 1996. 5

[7] R. H. Borcherts and L. C. Davis, "Force on a coil moving over a conducting surface including edge and channel effects," *Journal of Applied Physics*, vol. 43, no. 5, p. 2418, 1972. 5

[8] M. Brandstein and D. Ward, Eds., *Microphone arrays: signal processing and applications.* Berlin, Germany: Springer, 2001. 21

[9] H. Brauer, K. Porzig, J. Mengelkamp, M. Carlstedt, M. Ziolkowski, and H. Töpfer, "Lorentz force eddy current testing: a novel NDE technique," *The International Journal for Computation and Mathematics in Electrical and Electronic Engineering (COMPEL)*, vol. 33, no. 6, pp. 1965–1977, 2014. 8, 16, 54

[10] H. Brauer and M. Ziolkowski, "Eddy current testing of metallic sheets with defects using force measurements," *Serbian Journal of Electrical Engineering*, vol. 5, no. 1, pp. 11–20, 2008. 2, 5

[11] H. Brauer, J. Haueisen, M. Ziolkowski, U. Tenner, and H. Nowak, "Reconstruction of extended current sources in a human body phantom applying biomagnetic measuring techniques," *IEEE Transactions on Magnetics*, vol. 36, no. 4, pp. 1700–1705, 2000. 74

[12] J. Brinkhuis and V. Tikhomirov, *Optimization: insights and applications.* New Jersey, United Kingdom: Princeton University Press, 2005. 44

[13] M. Cacciola, S. Calcagno, F. C. Morabito, and M. Versaci, "Swarm optimization for imaging of corrosion by impedance measurements in eddy current test," *IEEE Transactions on Magnetics*, vol. 43, no. 4, pp. 1853–1856, 2007. 24

[14] M. Carlstedt, K. Porzig, R. Uhlig, M. Zec, M. Ziolkowski, and H. Brauer, "Application of Lorentz force eddy current testing and eddy current testing on moving nonmagnetic conductors," *Int. Journal of Applied Electromagnetics and Mechanics*, vol. 45, no. 1, pp. 519–526, 2014. 11

[15] M. Carlstedt, "A contribution to the experimental validation in Lorentz force eddy current testing," Ph.D. dissertation, Technische Universität Ilmenau, Ilmenau, Germany, 2016. 11

[16] M. Carlstedt, K. Porzig, M. Ziolkowski, R.-P. Uhlig, H. Brauer, and H. Töpfer, "Comparison of Lorentz force eddy current testing and common eddy current testing - measurement and simulation," *Studies on Applied Electromagnetics & Mechanics*, vol. 39, pp. 218–225, 2013. 6

[17] D. Colton and R. Kress, *Inverse acoustic and electromagnetic scattering theory.* New York, USA: Springer, 2010. 19

[18] S. Das and P. N. Suganthan, "Differential evolution: a survey of the state-of-the-art," *IEEE Transactions on Evolutionary Computation*, vol. 15, no. 1, pp. 4–31, 2011. 50, 56, 63, 64, 65

[19] L. C. Davis, "Drag force on a magnet moving near a thin conductor," *Journal of Applied Physics*, vol. 43, no. 10, p. 4256, 1972. 5

[20] N. Derby and S. Olbert, "Cylindrical magnets and ideal solenoids," *American Journal of Physics*, vol. 78, no. 3, pp. 229–235, 2010. 25, 26, 32, 33

[21] G. Donoso, C. L. Ladera, and P. Martín, "Damped fall of magnets inside a conducting pipe," *American Journal of Physics*, vol. 79, no. 2, p. 193, 2011. 6

[22] T. D'Orazio, C. Guaragnella, M. Leo, and P. Spagnolo, "Defect detection in aircraft composites by using a neural approach in the analysis of thermographic images," *NDT & E International*, vol. 38, no. 8, pp. 665–673, 2005. 5

[23] O. Dorn, E. L. Miller, and C. M. Rappaport, "A shape reconstruction method for electromagnetic tomography using adjoint fields and level sets," *Inverse Problems*, vol. 16, pp. 1119–1156, 2000. 97

[24] E. R. Dougherty and J. T. Astola, *Nonlinear filters for image processing*. Washington, USA: Wiley IEEE Press, 1999. 52

[25] A. Duca, M. Rebican, L. Janousek, M. Smetana, and T. Strapacova, "PSO based techniques for NDT-ECT inverse problems," in *Proceedings of the 18th International Workshop on Electromagnetic Nondestructive Evaluation*, Bratislava, Slovak Republic, June 2013, pp. 323–330. 24

[26] R. Eichardt, D. Baumgarten, L. Di Rienzo, S. Linzen, V. Schultze, and J. Haueisen, "Localisation of buried ferromagnetic objects based on minimum-norm-estimations: a simulation study," *The International Journal for Computation and Mathematics in Electrical and Electronic Engineering*, vol. 28, no. 5, pp. 1327–1337, 2009. 23

[27] R. Eichardt, D. Baumgarten, B. Petković, F. Wiekhorst, L. Trahms, and J. Haueisen, "Adapting source grid parameters to improve the condition of the magnetostatic linear inverse problem of estimating nanoparticle distributions," *Medical & Biological Engineering & Computing*, vol. 50, no. 10, pp. 1081–1089, 2012. 20, 67, 71, 74, 79

[28] M. Faraday, "Experimental researches in electricity," *Philosophical Transactions of the Royal Society of London*, vol. 122, pp. 125–162, 1892. 5

[29] R. M. Feldmann and C. Valdez-Flores, *Applied probability and stochastic processes*, 2nd ed. Berlin, Germany: Springer, 2014. 56

[30] L. J. Fogel, A. J. Owens, and M. J. Walsh, *Artificial intelligence through simulated evolution*. New York, USA: John Wiley, 1966. 24

[31] M. Fuchs, M. Wagner, T. Köhler, and H.-A. Wischmann, "Linear and nonlinear current density reconstructions," *Journal of Clinical Neurophysiology*, vol. 16, no. 3, pp. 267–295, 1999. 23, 67, 70, 78

[32] M. Fuchs, H.-A. Wischmann, M. Wagner, R. Drenckhahn, and T. Köhler, "Source reconstructions by spatial deviation scans," in *Proceedings of the 10th International Conference on Biomagnetism*, Santa Fé, New Mexico, February 1996, pp. 213–216. 21

[33] E. P. Furlani, *Permanent magnet and electromechanical devices*. New York, USA: Academic Press, 2001. 26, 30, 31

[34] E. Furlani, "A three-dimensional field solution for axially-polarized multipole disks," *Journal of Magnetism and Magnetic Materials*, vol. 135, no. 2, pp. 205–214, 1994. 25

[35] R. Gämberle, S. Müller, and P. Koumoutsakos, "A parameter study for Differential Evolution," *Advances in Intelligent Systems, Fuzzy Systems, and Evolutionary Computation*, vol. 10, pp. 293–298, 2002. 64

[36] D. E. Goldberg, *Genetic algorithms in search, optimization and machine learning*. Boston, USA: Addison-Wesley, 1989. 24

[37] G. H. Golub, M. Heath, and G. Wahba, "Generalized cross-validation as a method for choosing a good ridge parameter," *Technometrics*, vol. 21, no. 2, pp. 215–223, 1979. 71

[38] T. Götz, R. Huoker, O. W. Witte, and J. Haueisen, "Thalamocortical impulse propagation and information transfer in EEG and MEG," *Journal of Clinical Neurophysiology*, vol. 31, pp. 253–260, 2014. 78

[39] J. Hadamard, "Sur les problèmes aux dérivées partielles et leur signification physique," *Princeton University Bulletin*, vol. 13, no. 28, pp. 49–52, 1902. 20

[40] K. D. Hahn, E. M. Johnson, A. Brokken, and S. Baldwin, "Eddy current damping of a magnet moving through a pipe," *American Journal of Physics*, vol. 66, no. 12, pp. 1066–1076, 1998. 6

[41] M. S. Hämäläinen and R. J. Ilmoniemi, "Interpreting magnetic fields of the brain: minimum norm estimates," *Medical & Biological Engineering & Computing*, vol. 32, pp. 35–42, 1994. 23

[42] P. C. Hansen and D. P. O'Leary, "The use of the L-curve in the regularization of discrete ill-posed problems," *SIAM Journal on Scientific Computing*, vol. 14, no. 6, pp. 534–553, 1993. 71

[43] P. Hansen, "The truncated SVD as a method for regularization," *BIT Numerical Mathematics*, vol. 27, pp. 534–553, 1987. 22

[44] J. Haueisen, R. Unger, T. Beuker, and M. Bellemann, "Evaluation of inverse algorithms in the analysis of magnetic flux leakage data," *IEEE Transactions on Magnetics*, vol. 38, no. 3, pp. 1481–1488, 2002. 23, 72

[45] C. Hellier, *Handbook of nondestructive evaluation*, 2nd ed. New York, USA: McGraw Hill, 2012. 5

[46] H. Heuer, M. H. Schulze, and N. Meyendorf, "High resolution inspection of carbon fiber materials by eddy current techniques," in *Proc. 2nd Int. Symp. NDT Aerospace*, vol. 2, no. 3, 2010, pp. 1–13. 5

[47] Y. Hidaka, T. Sato, and H. Igarashi, "Topology optimization method based on on–off method and level set approach," *IEEE Transactions on Magnetics*, vol. 50, no. 2, pp. 617–620, 2014. 97

[48] J. H. Holland, "Outline for a logical theory of adaptive systems," *Journal of the Association for Computing Machinery*, vol. 3, pp. 297–314, 1961. 24

[49] V. M. Karbhari, Ed., *Nondestructive evaluation of polymer matrix composites.* Cambridge, United Kingdom: Woodhead Publishing Limited, 2013. 87

[50] J. Kennedy and R. Eberhart, "Particle swarm optimization," in *Proceedings of the IEEE International Conference on Neural Networks*, 1995, vol. 4, pp. 1942–1948. 24

[51] S. Kirkpatrick, C. D. Gelatt, and M. P. Vecchi, "Optimization by simulated annealing," *Science*, no. 220, pp. 671–680, 1983. 23

[52] A. Kirsch, *An introduction to the mathematical theory of inverse problems.* Berlin, Germany: Springer, 2011. 19

[53] M. Klemm, D. Schweitzer, S. Peters, L. Sauer, M. Hammer, J. Haueisen, and V. E. Degtyar, "FLIMX: a software package to determine and analyze the fluorescence lifetime in time-resolved fluorescence data from the human eye," *PLoS ONE*, vol. 10, no. 7, pp. 1–28, 2015. 49

[54] F. Kojima, N. Kubota, F. Kobayashi, and T. Takagi, "Shape recovery of natural crack using evolutionary programming related to eddy current testing," *International Journal of Applied Electromagnetics and Mechanics*, vol. 15, pp. 243–247, 2002. 24

[55] J. Langerholc, "Torques and forces on a moving coil due to eddy currents," *Journal of Applied Physics*, vol. 44, no. 4, p. 1587, 1973. 5

[56] U. Leder, J. Haueisen, M. Huck, and H. Nowak, "Non-invasive imaging of arrythmogenic left-ventricular myocardium after infarction," *The Lancet*, vol. 325, no. 9143, p. 1825, 1998. 23

[57] S.-W. Lee and R. C. Menendez, "Force on current coils moving over a conducting sheet with application to magnetic levitation," *Proceedings of the IEEE*, vol. 62, no. 5, 1974. 5

[58] E. Lenz, "Über die Bestimmung der Richtung der durch elektrodynamische Verteilung erregten galvanischen Ströme," *Annalen der Physik*, vol. 107, no. 31, pp. 483–494, 1834. 5

[59] K. Levenberg, "A method for the solution of certain nonlinear problems in least squares," *Quarterly of Applied Mathematics*, vol. 2, pp. 164–168, 1944. 23

[60] Y. Li, L. Udpa, and S. Udpa, "Three-dimensional defect reconstruction from eddy current NDE signals using a genetic local search algorithm," *IEEE Transactions on Magnetics*, vol. 40, no. 2, pp. 410–417, 2004. 24

[61] H. A. Lorentz, "La théorie électromagnétique de Maxwell et son application aux corps mouvants," *Archives Néerlandaises des Sciences Exactes et Naturelles*, vol. 25, pp. 363–552, 1892. 5

[62] L. Ma and M. Soleimani, "Hidden defect identification in carbon fiber reinforced polymer plates using magnetic induction tomography," *Measurement Science Technology*, vol. 25, pp. 1–9, 2010. 5, 23

[63] P. Mallick, *Fiber-reinforced composites.* New York, USA: CRC Press, 2008. 7

[64] K. Mandal and D. L. Atherton, "A study of magnetic flux leakage signals," *Journal of Physics D: Applied Physics*, vol. 31, pp. 3211–3217, 1998. 5

[65] D. Marquardt, "An algorithm for least-squares estimation of nonlinear parameters," *Journal of the Society for Industrial and Applied Mathematics*, vol. 11, no. 2, pp. 431–441, 1963. 23

[66] A. Massa, M. Pastorino, and A. Randazzo, "Reconstruction of two-dimensional buried objects by a Differential Evolution method," *Inverse Problems*, vol. 20, no. 6, pp. 135–150, 2004. 24

[67] *Mehrachsen-Kraftsensor K3D40*, ME-Messsysteme GmbH, Henningsdorf, Germany, 2014. 11

[68] J. Mengelkamp, M. Carlstedt, K. Weise, M. Ziolkowski, H. Brauer, and J. Haueisen, "Current density reconstructions for inverse calculation of defects in Lorentz force evaluation," in *Proceedings of the 9th International Workshop on Optimization & Inverse Problems in Electromagnetism*, Delft, The Netherlands, September 2014, pp. 44–45. 67

[69] J. Mengelkamp, K. Porzig, M. Carlstedt, M. Ziolkowski, H. Brauer, and J. Haueisen, "Forward solution for Lorentz force evaluation with different models of the permanent magnet," in *Proceedings of the 9th IET International Conference on Computation in Electromagnetics*, London, United Kingdom, March 2014, pp. 1–2. 2, 25

[70] J. Mengelkamp, M. Carlstedt, K. Weise, M. Ziolkowski, H. Brauer, and J. Haueisen, "Current density reconstructions for Lorentz force evaluation," *Research in Nondestructive Evaluation*, pp. 1–25, 2016. [Online]. Available: http://dx.doi.org/10.1080/09349847.2015.1111483 3, 12, 67

[71] J. Mengelkamp, D. Lattner, J. Haueisen, M. Carlstedt, K. Weise, M. Ziolkowski, H. Brauer, and R. Eichardt, "Lorentz force evaluation with Differential Evolution," *IEEE Transactions on Magnetics*, vol. 52, no. 5, pp. 6 201 310(1–10). 2, 49

[72] J. Mengelkamp, M. Ziolkowski, K. Weise, M. Carlstedt, H. Brauer, and J. Haueisen, "Permanent magnet modeling for Lorentz force evaluation," *IEEE Transactions on Magnetics*, vol. 51, no. 7, pp. 6 201 211(1–11), 2015. 2, 25

[73] C. Meola, G. M. Carlomagno, A. Squillace, and A. Vitiello, "Non-destructive evaluation of aerospace materials with lock-in thermography," *Engineering Failure Analysis*, vol. 13, no. 3, pp. 380–388, 2006. 5

[74] C. Moosbrugger, Ed., *Electrical and magnetic properties of metals.* Ohio, USA: The Materials Information Society, 2000. 82

[75] M. Morozov, G. Rubinacci, A. Tamburrino, and S. Ventre, "Numerical models of volumetric insulating cracks in eddy current testing with experimental validation," *IEEE Transactions on Magnetics*, vol. 42, no. 5, pp. 1568–1576, 2006. 12

[76] J. C. Mosher, P. S. Lewis, and R. M. Leahy, "Multiple dipole modeling and localization from spatio-temporal MEG data," *IEEE Transactions on Biomedical Engineering*, vol. 39, no. 6, pp. 541–557, 1992. 21

[77] A. Mouritz, C. Townsend, and M. Shah Khan, "Nondestructive detection of fatigue damage in thick composites by pulse-echo ultrasonics," *Composite Science and Technology*, vol. 60, no. 1, pp. 23–32, 2000. 5

[78] J. A. Nelder and R. Mead, "A simplex method for function minimization," *The Computer Journal*, vol. 7, pp. 308–313, 1965. 23, 35

[79] M. R. Osborne, *Finite algorithms in optimization and data analysis.* New York, USA: Wiley, 1985. 71

[80] D. W. Pepper and J. C. Heinrich, *The finite element method: basic concepts and applications*, 2nd ed. New York, USA: Taylor & Francis Group, 2006. 19

[81] B. Petković, J. Haueisen, M. Zec, R. Uhlig, H. Brauer, and M. Ziolkowski, "Lorentz force evaluation: a new approximation method for defect reconstruction," *NDT & E International*, vol. 59, pp. 57–67, 2013. 2, 7, 12, 14, 23, 63, 78, 79

[82] B. Petković, "Assessment of linear inverse problems in magnetocardiography and Lorentz force eddy current testing," Ph.D. dissertation, Technische Universität Ilmenau, Ilmenau, Germany, 2013. 20

[83] A. J. Petruska and J. J. Abbott, "Optimal permanent magnet geometries for dipole field approximation," *IEEE Transactions on Magnetics*, vol. 49, no. 2, pp. 811–819, 2013. 25, 46, 99

[84] D. L. Phillips, "A technique for the numerical solution of certain integral equations of the first kind," *Journal of the ACM*, vol. 9, no. 1, pp. 84–97, 1962. 22

[85] A. Pirani and M. Ricci, "3D reconstruction of flaws in metallic materials by eddy current inspections," *Electromagnetic Nondestructive Evaluation*, pp. 109–116, 2008. 23

[86] K. J. W. Pluk, T. A. van Beek, J. W. Jansen, and E. A. Lomonova, "Modeling and measurements on a finite rectangular conducting plate in an eddy current damper," *IEEE Transactions on Industrial Electronics*, vol. 61, no. 8, pp. 4061–4072, 2014. 12, 68

[87] W. H. Press, S. A. Teukolsky, W. T. Vetterling, and B. Flannery, *Numerical recipes in C*, 2nd ed. Cambridge, United Kingdom: University Press, 1992. 23, 35

[88] K. V. Price, R. M. Storn, and J. A. Lampinen, *Differential Evolution: a practical approach to global optimization.* Berlin, Germany: Springer, 2005. 49, 61, 64

[89] A. Qing, X. Xu, and Y. Gan, "Anisotropy of composite materials with inclusion with orientation preference," *IEEE Transactions on Antennas and Propagation*, vol. 53, no. 2, pp. 737–744, 2005. 24

[90] H. L. Rakotoarison, J.-P. Yonnet, and B. Delinchant, "Using coulombian approach for modeling scalar potential and magnetic field of a permanent magnet with radial polarization," *IEEE Transactions on Magnetics*, vol. 43, no. 4, pp. 1261–1264, 2007. 25

[91] R. Ravaud, G. Lemarquand, S. Babic, V. Lemarquand, and C. Akyel, "Cylindrical magnets and coils: fields, forces, and inductances," *IEEE Transactions on Magnetics*, vol. 46, no. 9, pp. 3585–3590, 2010. 33

[92] R. Ravaud, G. Lemarquand, V. Lemarquand, and C. Depollier, "Analytical calculation of the magnetic field created by permanent magnet rings," *IEEE Transactions on Magnetics*, vol. 44, no. 8, pp. 1982–1989, 2008. 25

[93] J. R. Reitz, "Forces on moving magnets due to eddy currents," *Journal of Applied Physics*, vol. 41, no. 5, p. 2067, 1970. 5

[94] P. L. Richards and M. Tinkham, "Magnetic suspension and propulsion systems for high-speed transportation," *Journal of Applied Physics*, vol. 43, no. 6, p. 2680, 1972. 5

[95] P. Rocca, G. Oliveri, and A. Massa, "Differential Evolution as applied to electromagnetics," *IEEE Antennas and Propagation Magazine*, vol. 53, no. 1, pp. 38–49, 2011. 24

[96] T. J. Rocha, H. G. Ramos, A. Lopes Ribeiro, D. J. Pasadas, and C. S. Angani, "Studies to optimize the probe response for velocity induced eddy current testing in aluminium," *Measurement*, vol. 67, pp. 108–115, 2015. 6

[97] U. L. Rohde and M. Rudolph, *RF/Microwave circuit design for wireless applications.* Hoboken, USA: Wiley, 2013. 85

[98] L.-L. Rouve, L. Schmerber, O. Chadebec, and A. Foggia, "Optimal magnetic sensor location for spherical harmonic identification applied to radiated electrical devices," *IEEE Transactions on Magnetics*, vol. 42, no. 4, pp. 1167–1170, 2006. 71

[99] W. M. Saslow, "Maxwell's theory of eddy currents in thin conducting sheets and applications to electromagnetic shielding and MAGLEV," *American Journal of Physics*, vol. 60, no. 8, pp. 693–711, 1992. 5

[100] M. H. Schulze, H. Heuer, M. Küttner, and N. Meyendorf, "High-resolution eddy current sensor system for quality assessment of carbon fiber materials," *Microsystem Technologies*, vol. 16, pp. 791–797, 2010. 5

[101] H. R. Schwarz and N. Köckler, *Numerische Mathematik*, 8th ed. Wiesbaden, Germany: Vieweg & Teubner, 2011. 86

[102] H.-P. Schwefel, *Evolution and optimum seeking.* New York, USA: John Wiley, 1995. 24

[103] J. A. Sethian, *Level set methods and fast marching methods: evolving interfaces in computational geometry, fluid mechanics, computer vision, and materials science*, 2nd ed. Cambridge, United Kingdom: Cambridge University Press, 2008, reprinted. 97

[104] S. Singer and S. Singer, "Complexity analysis of the Nelder-Mead search iterations," in *Proceedings of the 1st Conference on Applied Mathematics and Computation*, 1999, pp. 185–196. 44

[105] J. Sinke, "Some inspection methods for quality control and in-service inspection of GLARE," *Applied Composite Materials*, vol. 10, pp. 277–291, 2003. 5, 8

[106] R. Srebro, "Iterative refinement of the minimum norm solution of the bioelectric inverse problem," *IEEE Transactions on Biomedical Engineering*, vol. 43, pp. 547–552, 1996. 67

[107] R. Storn and K. Price, "Differential Evolution: a simple and efficient heuristic for global optimization over continuous spaces," *Journal of Global Optimization*, vol. 11, pp. 341–359, 1997. 49, 64

[108] A. H. Stroud, *Approximate calculation of multiple integrals.* New Jersey, USA: Prentice Hall, 1971. 47

[109] Y. S. Sun, W. Lord, and G. Katragadda, "Motion induced remote field eddy current effect in a magnetostatic nondestructive testing tool: a finite element prediction," *IEEE Transactions on Magnetics*, vol. 50, no. 5, pp. 3304–3307, 1994. 6

[110] A. Thess, E. V. Votyakov, and Y. Kolesnikov, "Lorentz force velocimetry," *Physical Review Letters*, vol. 96, no. 16, pp. 164 501(1–4), 2006. 6

[111] A. Thess, E. Votyakov, B. Knaepen, and O. Zikanov, "Theory of the Lorentz force flowmeter," *New Journal of Physics*, vol. 9, no. 8, p. 299, 2007. 6

[112] A. N. Tikhonov, "Solution of incorrectly formulated problems and the regularization technique," *Soviet Mathematics Doklady*, vol. 4, pp. 1035–1038, 1963. 22

[113] R. P. Uhlig, M. Zec, H. Brauer, and A. Thess, "Lorentz force eddy current testing: a prototype model," *Journal of Nondestructive Evaluation*, vol. 31, no. 4, pp. 357–372, 2012. 6

[114] R. P. Uhlig, M. Zec, M. Ziolkowski, H. Brauer, and A. Thess, "Lorentz force sigmometry: a contactless method for electrical conductivity measurements," *Journal of Applied Physics*, vol. 111, no. 9, p. 094914, 2012. 7

[115] R. P. Uhlig, "Identification of material defects in metallic materials using Lorentz force eddy current testing: fundamentals, metrological implementation and verfication," Ph.D. dissertation, Technische Universität Ilmenau, Ilmenau, Germany, 2012. 11

[116] L. Vogelesang and A. Vlot, "Development of fibre metal laminates for advanced aerospace structures," *Journal of Materials Processing Technology*, vol. 103, no. 1, pp. 1 – 5, 2000. 81

[117] E. V. Votyakov and A. Thess, "Interaction of a magnetic dipole with a slowly moving electrically conducting plate," *Journal of Engineering Mathematics*, vol. 77, no. 1, pp. 147–161, 2012. 5, 68

[118] M. Wagner, H.-A. Wischmann, M. Fuchs, T. Köhler, and R. Drenckhahn, "Current density reconstructions using the L1 norm," in *Proceedings of the 10th International Conference on Biomagnetics*, 1996, vol. 1, pp. 393–396. 23, 67

[119] M. Wagner, "Rekonstruktion neuronaler Ströme aus bioelektrischen und biomagnetischen Messungen auf der aus MR-Bildern segmentierten Hirnrinde," Ph.D. dissertation, Technische Universität Hamburg-Harburg, Hamburg, Germany, 1998. 70

[120] K. Weise, "Advanced modeling in Lorentz force eddy current testing," Ph.D. dissertation, Technische Universität Ilmenau, Ilmenau, Germany, 2015. 10

[121] K. Weise, M. Carlstedt, M. Ziolkowski, and H. Brauer, "Uncertainty analysis in Lorentz force eddy current testing," *IEEE Transactions on Magnetics*, vol. 52, no. 3, pp. 6 200 104(1–4), 2016. 12

[122] K. Weise, M. Carlstedt, M. Ziolkowski, H. Brauer, and H. Töpfer, "Lorentz force on permanent magnet rings by moving electrical conductors," *IEEE Transactions on Magnetics*, vol. 51, no. 12, pp. 6 202 211(1–11), 2015. 6

[123] K. Weise, R. Schmidt, M. Carlstedt, M. Ziolkowski, H. Brauer, and H. Töpfer, "Optimal magnet design for Lorentz force eddy current testing," *IEEE Transactions on Magnetics*, vol. 51, no. 9, pp. 6 201 415(1–15), 2015. 10, 81, 82, 85, 92

[124] G. Wu and J.-M. Yang, "The mechanical behavior of GLARE laminates for aircraft structures," *Journal of the Minerals, Metals & Materials Society*, vol. 57, no. 1, pp. 72–79, 2005. 7, 81

[125] Z. J. Yang, T. H. Johansen, H. Bratsberg, G. Helgesen, and A. T. Skjeltorp, "Potential and force between a magnet and a bulk superconductor studied by a mechanical pendulum." *Superconductor Science and Technology*, vol. 3, pp. 591–597, 1990. 26, 30, 31

[126] M. Zec, "Theory and numerical modelling of Lorentz force eddy current testing," Ph.D. dissertation, Technische Universität Ilmenau, Ilmenau, Germany, 2013. 19

[127] M. Zec, R. P. Uhlig, M. Ziolkowski, and H. Brauer, "Fast technique for Lorentz force calculations in non-destructive testing applications," *IEEE Transactions on Magnetics*, vol. 50, no. 2, pp. 133–136, 2014. 10, 14, 19, 74

[128] M. Ziolkowski, *Modern methods for electromagnetic field problems.* Szczecin, Poland: West Pomeranian University of Technology College Publisher, 2015. 12, 16

[129] M. Ziolkowski and H. Brauer, "Fast computation technique of forces acting on moving permanent magnet," *IEEE Transactions on Magnetics*, vol. 46, no. 8, pp. 2927–2930, 2010. 19, 101

[130] M. Ziolkowski, J. Haueisen, H. Nowak, and H. Brauer, "Equivalent ellipsoid as an interpretation tool of extended current distributions in biomagnetic inverse problems," *IEEE Transactions on Magnetics*, vol. 36, no. 4, pp. 1692–1695, 2000. 67, 72

[131] E. Zitzler, K. Deb, and L. Thiele, "Comparison of multiobjective evolutionary algorithms: empirical results," *Evolutionary Computation*, vol. 8, no. 2, pp. 173–195, 2000. 24

[132] H. Zou and T. Hastie, "Regularization and variable selection via the elastic net," *Journal of the Royal Statistical Society*, vol. 67, Part 2, pp. 301–320, 2005. 79

Erklärung

Ich versichere, dass ich die vorliegende Arbeit ohne unzulässige Hilfe Dritter und ohne Benutzung anderer als der angegebenen Hilfsmittel angefertigt habe. Die aus anderen Quellen direkt oder indirekt übernommenen Daten und Konzepte sind unter Angabe der Quelle gekennzeichnet.

Bei der Auswahl und Auswertung folgenden Materials haben mir die nachstehend aufgeführten Personen in der jeweils beschriebenen Weise unentgeltlich geholfen:

1) *Unterstützung bei der Interpretation der Ergebnisse in der gesamten Arbeit.*
   Prof. Dr.-Ing. habil. Jens Haueisen, Technische Universität Ilmenau, Fakultät für Informatik und Automatisierung, Deutschland

2) *Unterstützung bei der Implementierung der Modelle zur Berechnung der magnetischen Flussdichte von Permanentmagneten im Abschnitt 3.2.*
   Dr.-Ing. Marek Ziolkowski, Technische Universität Ilmenau, Fakultät für Elektrotechnik und Informationstechnik, Deutschland

3) *Durchführung der Lorentzkraft-Wirbelstrom-Prüfung zur Untersuchung der Verbundwerkstoffe Alucobond und GLARE, sowie Bereitstellung der gemessenen Lorentzkraft-Signale in den Abschnitten 4.2.3 and 6.2.1.*
   M. Sc. Matthias Carlstedt, Technische Universität Ilmenau, Fakultät für Elektrotechnik und Informationstechnik, Deutschland

4) *Durchführung der numerischen Simulationen des Lorentzkraft-Wirbelstrom-Prüfverfahrens mittels eines Finite-Elemente-Modelles, sowie Bereitstellung der simulierten Lorentzkraft-Signale in den Abschnitten 2.4.1 und 4.2.3, sowie dem Anhang B.*
   M. Sc. Konstantin Weise, Technische Universität Ilmenau, Fakultät für Elektrotechnik und Informationstechnik, Deutschland

Weitere Personen waren an der inhaltlich-materiellen Erstellung der vorliegenden Arbeit nicht beteiligt. Insbesondere habe ich hierfür nicht die entgeltliche Hilfe von Vermittlungs bzw. Beratungsdiensten (Promotionsberater oder anderer Personen) in Anspruch genommen. Niemand hat von mir unmittelbar oder mittelbar geldwerte Leistungen für Arbeiten erhalten, die im Zusammenhang mit dem Inhalt der vorgelegten Dissertation stehen.

Die Arbeit wurde bisher weder im In- noch im Ausland in gleicher oder ähnlicher Form einer Prüfungsbehörde vorgelegt.

Ich bin darauf hingewiesen worden, dass die Unrichtigkeit der vorstehenden Erklärung als Täuschungsversuch angesehen wird und gemäß § 7 Abs. 10 der Promotionsordnung den Abbruch des Promotionsverfahrens zur Folge hat.

Ilmenau, den 11. April 2016   Judith Mengelkamp